Karlsruhe Institute of Technology

Background generation due to stored electrons at the KATRIN main spectrometer

Diploma Thesis of

Nikolaus Trost

At the Department of Physics
Institute of Experimental Nuclear Physics
(IEKP)

Reviewer:	Prof. Dr. Guido Drexlin
Second reviewer:	Prof. Dr. Husemann
Advisor:	Dr. Nancy Wandkowsky
Second advisor:	Dipl. Phys. Stefan Groh

Duration: 17. September 2012 – 17. September 2013

Ich versichere wahrheitsgemäß, die Arbeit selbstständig angefertigt, alle benutzten Hilfsmittel vollständig und genau angegeben und alles kenntlich gemacht zu haben, was aus Arbeiten anderer unverändert oder mit Abänderungen entnommen wurde.

Karlsruhe, 17.09.2013

.....

(**Nikolaus Trost**)

Contents

1. Neutrino Physics and the Standard Model

The KATRIN experiment will measure the effective mass of the electron anti-neutrino with a previously unmatched sensitivity of $m_{\bar{\nu_e}} < 200$ meV (90% C.L.) by precision spectroscopy of the tritium β-decay near its endpoint of about 18.6 KeV/c^2. In this chapter a brief overview of the history of neutrino physics is given in section 1.1. The properties of neutrinos and their role in the Standard Model (SM) are discussed in 1.2. Section 1.3 elaborates on the phenomenon of neutrino oscillations and the implied non-zero neutrino masses. Then an overview of different experimental approaches to the determination of the neutrino mass is given in 1.4.

1.1. Discovery of the neutrino

For a long time neutrinos were not known to exist. The neutrino was first proposed in 1930 by Wolfgang Pauli. In a famous letter[1] he sought a solution to a problem that was discovered by James Chadwick in 1914[2]. He noted that the β-spectrum of radium was in fact continuous, as displayed in figure 1.1, and not discrete as previously known for α- and γ-spectra. This continuous β-spectrum could not be explained by a mere two-body decay or otherwise momentum- and energy conservation would have to be violated. Pauli instead chose to postulate a very light, electrically neutral spin 1/2 particle that would be emitted in addition to the β-particle. With this new particle, which Pauli initially called *neutron*, the β-decay is a three-body-decay where the kinematics allow for continuous spectra, since the reaction products share the decay energy. After the discovery of the neutron as part of the atomic nucleus in 1932 by Chadwick[4] Enrico Fermi continued Paulis approach and in 1934 formulated a theory of the nuclear beta decay[5], renaming Paulis particle *neutrino*. Fermi assumed a-point like interaction with the reaction noted as

$$n \rightarrow p + e^- + \bar{\nu_e} \tag{1.1}$$

The cross sections derived from Fermis theory are valid till today in the limit of low energies. As we today know the weak force is not a point-interaction, but mediated by W^+-, W^- and Z-bosons which leads to corrections for high energies. For the inverse β-decay

$$\bar{\nu} + n \rightarrow p + e^- \tag{1.2}$$

the cross section was first calculated by Bethe and Peierls in 1934 [6] to be of the order of $\sigma < 10^{-44}$ cm^2. Because of this extremely small cross section it took till 1956 when

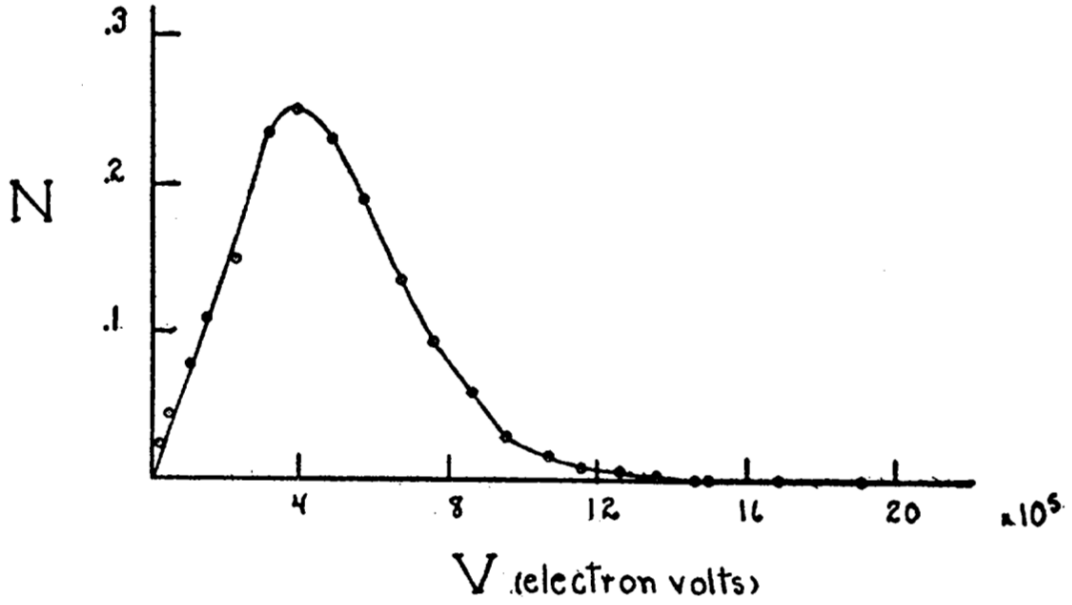

Figure 1.1.: the β-spectrum turned out to be continuous. Image taken from[3]

the "ghost particle" was directly discovered by Fred Reines and Clyde Cowan[7][8] in the famous series of *Poltergeist experiments* near the Savannah River. They used the inverse beta decay in water to detect incoming electron anti-neutrinos produced in large numbers ($\approx 10^{13}$ cm^{-2}s^{-1}) by the nearby Savannah River reactor. Their detector consisted of two tanks filled with 200 liters cadmium chloride solution each and three liquid scintillation counters of 1400 litres. In the inverse β-decay two particles are emitted: a positron and a neutron. The positron rapidly annihilates with an electron in the water producing two monoenergetic 511 keV photons headed in opposite directions. Despite this distinct signature previous experiments struggled with a large background from cosmic rays. The crucial ingredient was the Cadmium that captures the emitted neutron after it is moderated by the surrounding water. This leaves the nucleus in an excited state that decays via emission of an 3-11 MeV γ-photon that also can be detected. This way it is possible to do a delayed coincidence discrimination and reduce the background substantially. This technique enabled them to detect about 3 neutrino events per hour resulting in a measured cross section of $1.2^{+0.7}_{-0.4} \cdot 10^{-43}$ cm^{-2} for the inverse beta decay 1.2, a value compatible with the prediction within 5%. About four decades later in 1995 Reines received the nobel prize also in the name of Cowan, who passed away in 1974.

Next to be discovered was the muon neutrino ν_μ in 1962 by Ledermann, Steinberger and Schwartz with the AGS at Brookhaven National Laboratory [9]. They investigated the pion decay

$$\pi^+ \to \mu^+ + \nu_\mu \qquad \pi^- \to \mu^- + \bar{\nu}_\mu \tag{1.3}$$

using a spark chamber made of 10 t aluminium for detection. They discovered that the neutrinos from the pion beam never caused electronic showers in the detector material. Instead, they observed muon-induced events, thereby showing that the neutrinos from the muon beam were different from the electron (anti-)neutrinos. After the discovery of the τ lepton in 1975 the existence of a third neutrino, the ν_τ, was predicted [10]. In 2001 finally the tau neutrino ν_τ was discovered in the DONUT (Direct Observation of Nu Tau) experiment at Fermilab [11]. A 800 GeV proton beam was shot on a tungsten target to create particle showers containing a small fraction of D_S-mesons. These decay into

τ-leptons that in the end produce ν_τ. A massive shielding was used to remove almost all particles but ν_τ from the beam. While a combination of lead emulsion and stainless steel was used as detector material for the ν_τ. The DONUT experiment was designed to detect the charged-current interaction of ν_τ by observing only tau leptons being created at the interaction points. Since the typical decay length of the τ is only 2 mm at the ν_τ energies produced int the beam, it was rathre challenging to identify the signature of the tau lepton: A track with a sudden kink that results from a decay with a large transverse momentum and the neutrino remaining "invisible". An indirect observation indicating a third neutrino flavor however was made earlier in 1989 by the ALEPH experiment at LEP ,CERN [12][13]. Their very precise measurement of the Z_0 boson's decay width allowed to discriminate between the theoretical prediction for different numbers of neutrino flavors. The data fit best with $N_\nu = 3.01 \pm 0.15(\text{exp}) \pm 0.05(\text{theo})$ active neutrino flavors.

1.2. Neutrinos and the Standard Model

The Standard Model of particle physics is the most exact, yet incomplete description of nature we have at hand today. It describes all known fundamental particles and their interactions in the framework of quantum field theories and stems from the beautiful principle of gauge invariance. Once its symmetry group is fixed, most of the structure of the theory strictly follows from it. A complete treatment is found in the standard literature, e.g. [14], which this section is based on. The Standard Model's Lie group is

$$SU(3)_c \times SU(2)_L \times U(1)_{Y_w} \tag{1.4}$$

and results in a predominantly strongly interacting $SU(3)_c$ sector as described by QCD. And an only electro-weakly interacting $SU(2)_L \times U(1)_{Y_w}$ sector which is described by the Glashow-Weinberg-Salam-Model [15][16][17]. Thus particles are classified according to their participation in these interactions.

The only known interaction not described by the Standard Model is gravity, for its quantisation turns out to be a hard problem. Several approaches such as String theory, Loop Quantum Gravity and Asymptotic Safety exist [18][19][20]. Neither of which has been tested experimentally, mostly because they up to now are incomplete or lack predictive power.

Apart from gauge symmetries and those related to spacetime, e.g. the SO(3,1) group of special relativity, which are continuous there are discrete symmetries in the Standard Model that are more intricate: In our models, fundamental particles are described as indivisible objects without any substructure. The different kinds of particles can be distinguished by their quantum numbers only, while there are no means to distinguish one particle of a certain kind from another of the same kind. That is if we change the world by only exchanging two particles of the same kind it makes no difference in the outcome of measurements. This constraint allows two possibilities for the behavior of the system's wave function under this change: It can either stay the same, or pick up a minus sign. In both cases all observables remain unchaged. This fundamental symmetry in quantum mechanics allows us to classify particles into the two categories of fermions (antisymmetric, pick up a minus sign) and bosons (symmetric). This property is directly linked to the intrinsic angular momentum of the particle by the spin-statistics theorem [21][22]: particles with integer spin are bosons, particles with half-integer spin are fermions.

With these tools at hand we can describe the particle content of the Standard Model seen in figure 1.2: It embodies 3 generations of fermions grouped into the electro-weakly interacting leptons and the strongly (and electro-weakly) interacting quarks. Each generation consists of 2 quarks and two leptons, with each couple forming an isospin doublet that

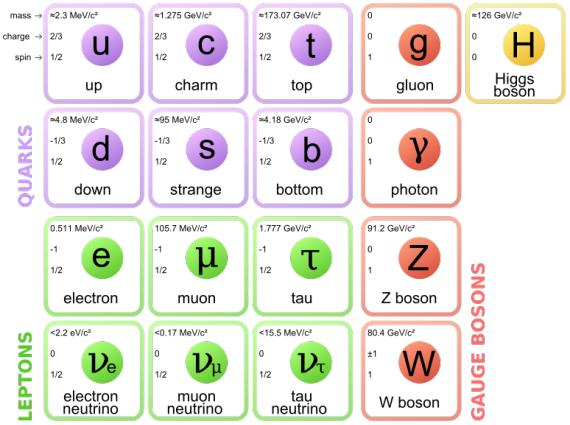

Figure 1.2.: Particles of the standard model

transforms under the $SU(2)$ group. The quarks are the only particles participating in all 4 interactions including gravity. They are also special because they carry fractional values of the elementary charge e: $+\frac{2}{3}$e for up-type quarks (up, charm, top) and $-\frac{1}{3}$e for down-type quarks (down, strange, bottom). However, due to the effect of color confinement, experimentally observable particles carry integer multiples of e. When attempting to separate quarks from each other, the strong interaction potential increases and new quarks are created out of the vacuum by the potential energy of the gluon field created by the color charge. To a macroscopic observer only color-neutral and integer electric charge states are visible.

The interactions are mediated by bosons: The electroweak interaction is carried by the $W^{\pm}$, Z bosons and photons, the strong interaction by gluons. A strict gauge symmetry however would forbid these particles to be massive with a simple mass term in their Lagrangian. This problem is solved within the Standard Model by the Higgs Mechanism [23][24] of dynamical symmetry breaking. This approach is based on the models and observations in solid state physics, where the ground state of a system (e.g. a crystal) is often found to be less symmetric than the corresponding Lagrangian. In this scenario the observed particle content is interpreted as low-energy excitations of the vacuum forming a ground state with lower symmetry within the high-energy symmetric theory. This part of the standard model was the last to be confirmed until in 2012 the Higgs boson was finally discovered at the LHC [25][26]. Although this neutral scalar particle, an excitation of the higgs background field that is understood to generate the particle masses in a gauge-invariant way, is the only accessible hint to the high-energy theory so far, its discovery is a great confirmation after decades of search.

Generation			Electric	Lepton	Interaction
1	2	3	charge	number	
e^-	μ^-	τ^-	-1	+1	electromagnetic, weak
ν_e	ν_μ	ν_τ	0	+1	weak
e^+	μ^+	τ^+	+1	-1	electromagnetic, weak
$\bar{\nu}_e$	$\bar{\nu}_\mu$	$\bar{\nu}_\tau$	0	-1	weak

Neutrinos in this picture are leptons and the isospin partners of the electron, muon and tau as displayed in table 1.2. They carry no electric charge and only interact weakly, implying parity and CP violation. Within the Standard Model neutrinos are assumed to be massless based on the observations of β-spectra and Goldhabers 1958 measurement of the neutrino helicity [27]. Helicity is defined as the normalized projection of the particle spin $\vec{\sigma}$ on to

the momentum $\vec{p}$:

$$h = \frac{\vec{\sigma} \cdot \vec{p}}{|\vec{p}|} \tag{1.5}$$

Goldhaber found the neutrinos to have a helicity of -1. If the neutrino's helicity is indeed always negative and the anti-neutrino's always positive, they have to travel at the speed of light. Otherwise reference frames can be found in which the momentum, but not the spin, is reversed and the helicity hence flips. Traveling at light speed consequently implies massless neutrinos. This asymmetry between ν_L and $\bar{\nu}_R$ is different from what is observed for the other fermions. There the charge conjugation operation C transforms a fermion into its anti-particle $Cf_{L/R} = \bar{f}_{L/R}$, not affecting handedness. This fails with neutrinos as, the ν_R and $\bar{\nu}_L$ states appear to be missing in nature. The two observed states however transform into each other under CP transformation $CP\nu_L = \bar{\nu}_R$. Two explanations to this puzzle are widely discussed.

Ettore Majorana showed that massive neutral particles can have a two-component spinor description [28]. In this case the neutrino and antineutrino would be their own antiparticles, i.e. $C\nu_L = \nu_L$ and $C\bar{\nu}_R = \bar{\nu}_R$. The neutrino would be a *Majorana particle*. The other possibility is that the "missing" states actually do exist, but because they only interact gravitationally or by neutrino mixing, they have not been observed so far. In this case the neutrino would be a Dirac particle like the other fermions.

In both cases the neutrino would be massive, as actually indicated by the observation of neutrino oscillations. In a strict interpretation this observation hence implies new physics beyond the standard model.

1.3. Neutrino mass and oscillations

For a long time, the discrepancy between the expected and the actually observed number of neutrinos coming from the sun puzzled physicists. Neutrino oscillations turned out as the solution to this longstanding problem, revealing the massive nature of neutrinos. This section will cover the historical and theoretical aspects of neutrino oscillations and discuss the implications for the neutrino mass.

1.3.1. The solar neutrino puzzle

As can be seen in figure 1.3 one of the main neutrino sources available on earth are the nuclear reactions fueling the sun. In terms of neutrino flux the sun is the second strongest source after the low energetic cosmic neutrino background.

The most dominant process contributing to the sun's neutrino spectrum is the pp-chain starting with the reaction

$$p + p \rightarrow d + e^+ + \nu_e \tag{1.6}$$

This reaction accounts for about 85% of the suns neutrino flux. In contrast to earth-bound neutrino sources like nuclear reactors the sun produces mainly ν_e and no $\bar{\nu}_e$. In heavier stars the otherwise sub-dominant CNO-cycle becomes important.

The solar neutrino puzzle came up when the Homestake [32][33] experiment measured the neutrino flux from the sun to be actually lower then expected from the Standard Solar Model (SSM). To detect solar neutrinos they developed a radiochemical detection technique based on chlorine in a tank filled with 600 t perchloroethylene using the reaction

$$\nu_e + {}^{37}\mathrm{Cl} \rightarrow {}^{37}\mathrm{Ar} + e^+ \tag{1.7}$$

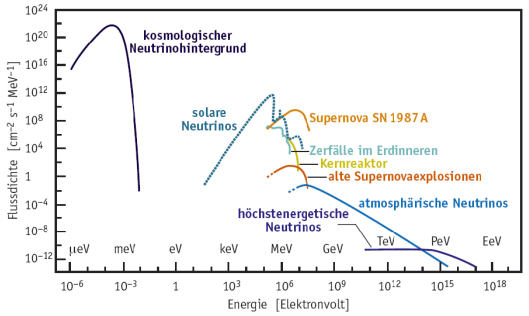

Figure 1.3.: Solar neutrinos provide a total (integrated) flux of about $6 \cdot 10^{10}$ $\mathrm{cm}^{-2}\mathrm{s}^{-1}$ at the earth. Shown are the flux densities of different neutrino sources in $\mathrm{cm}^{-2}\mathrm{s}^{-1}\mathrm{MeV}^{-1}$. The sun is even a stronger source than the spectacular SN 1987 A supernova from which the Kamiokande, IMB and Baksan experiments recorded a neutrino burst [29]. This was a rare event, for the supernova happened in the nearby magellanic cloud, at a distance of 51.47 kpc (167885 Ly). Image taken from [30]

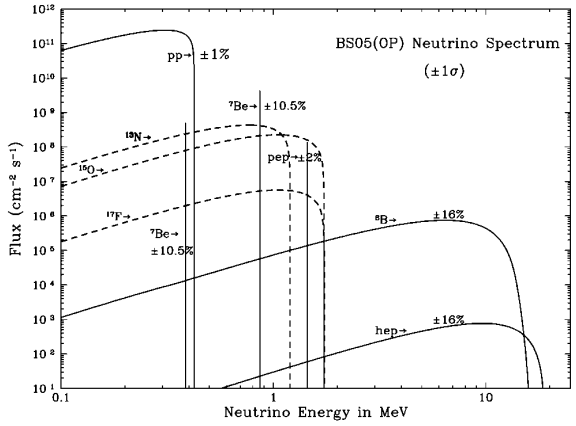

Figure 1.4.: Solar neutrino spectrum. Displayed are neutrino fluxes from pp-chain (solid) and the CNO-cycle (dashed). Figure taken from [31]

After a measurement interval of about 30 days they separated the produced Argon from the detector material. The Argon reacts via electron capture back to excited states of ^{37}Cl. Their de-excitation by emission of Auger electrons then was measured by proportional counters. The neutrino deficit established by Homestake was confirmed by other experiments like Gallex [34]/GNO [35], SAGE [36] and Kamiokande [37]. While the deficit was widely attributed to uncertainties in the SSM and its predictions, a different possibility was pointed out by B.Pontecorvo and V. Gribov [38]: The electron neutrinos generated in the sun could change their flavor during the travel to earth.

To finally resolve this problem the Sudbury Neutrino Observatory (SNO) was build. Its design was targeted at beeing able to detect all three neutrino flavors ν_e,ν_μ and ν_τ. The SNO experiment used an acrylic sphere filled with 1000 t of pure heavy water surrounded by photo multipliers situated in a depth of 2000 m in a former Canadian mine. In the heavy water (D_2O) the neutrinos undergo charged current (CC), neutral current (NC), and elastic scattering (ES) reactions:

$$\nu_x + e^- \rightarrow \nu_x + e^- \quad \text{ES} \tag{1.8}$$

$$\nu_e + d \rightarrow p + p + e^- \quad \text{CC, for } \nu_e \text{ only} \tag{1.9}$$

$$\nu_x + d \rightarrow p + n + \nu_x \quad \text{NC} \tag{1.10}$$

Due to the different signals produced by these reactions it was possible to discriminate between them and, by this, measure the total neutrino flux and the electron neutrino flux separately. After this phase I measurement multiple checks of the fluxes were performed loading the detector with salt water (phase 2) and ^{3}He (phase 3) looking for neutron capture. The SNO experiment showed that the total neutrino flux is in good agreement with the predictions of the SSM, whereas the electron neutrino flux is substantially lower. This established neutrino flavor oscillations as the solution to the solar neutrino puzzle [39].

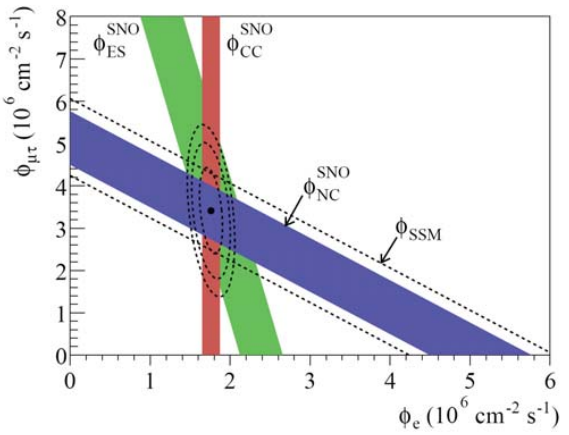

Figure 1.5.: The solar neutrino fluxes from ^{8}B as measured by SNO. Plotted is the neutrino flux from μ and τ flavors $\phi_{\mu\tau}$ over the electron neutrino flux ϕ_e. The solid bands represent the 1σ measurements of CC and NC fluxes. While the dashed line indicates the predictions of the SSM, the NC flux measures the total flux and is in good agreement with the predictions [40].

1.3.2. Theoretical description

Within the Standard Model neutrino flavor changing effects can not be explained. This led Pontecorvo and Gribov [38] to consider massive neutrinos. By introducing a unitary matrix translating between the flavor eigenstates $|\nu_f\rangle$ and the mass eigenstates $|\nu_{m_i}\rangle$:

$$|\nu_{m_i}\rangle = \sum_{f=e,\mu,\tau} U_{fm_i} |\nu_f\rangle \qquad |\nu_f\rangle = \sum_{i=1,2,3} U^*_{fm_i} |\nu_{m_i}\rangle \tag{1.11}$$

The matrix U_{fm_i} is called the **P**ontecorvo–**M**aki–**N**akagawa–**S**akata matrix and is similar to the CKM-matrix in the quark sector. There Cabibbo pioneered to explain (quark-) flavor mixing with ,at that time, one mixing angle [41]. A usual parameterization is

$$U = \begin{pmatrix} 1 & 0 & 0 \\ 0 & c_{23} & s_{23} \\ 0 & -s_{23} & c_{23} \end{pmatrix} \begin{pmatrix} c_{13} & 0 & s_{13}e^{-i\delta} \\ 0 & 1 & 0 \\ -s_{13}e^{i\delta} & 0 & c_{13} \end{pmatrix} \begin{pmatrix} c_{12} & s_{12} & 0 \\ -s_{12} & c_{12} & 0 \\ 0 & 0 & 1 \end{pmatrix} \begin{pmatrix} e^{i\alpha_1/2} & 0 & 0 \\ 0 & e^{i\alpha_2/2} & 0 \\ 0 & 0 & 1 \end{pmatrix}$$

with $c_{ij} = cos(\theta_{ij})$, $s_{ij} = sin(\theta_{ij})$ being the (co)sine of the three mixing angles θ_{ij}. The α_i are the two complex Majorana phases that appear when neutrinos are Majorana particles. These can cause CP violation and play a role in neutrinoless double beta decay. δ is a complex CP-violating Dirac phase. If a neutrino of flavor α is generated at $t = 0$, the value of interest is the *transition probability* P. Note that since neutrinos interact exclusively weak, they are always produced in a flavor eigenstate. A flavor eigenstate is a superposition of mass eigenstates:

$$|\nu(t=0)\rangle = |\nu_\alpha\rangle = U^*_{\alpha m_1} |\nu_{m_1}\rangle + U^*_{\alpha m_2} |m_2\rangle + U^*_{\alpha m_2} |m_2\rangle \tag{1.12}$$

The mass eigenstates are the eigenstates of the Hamiltonian and hence determine the propagation of the neutrino. The time evolution operator in this case is

$$T = \sum_{i=1,2,3} \exp(-i/\hbar t E_i) \left|\nu_{m_i}\right\rangle \left\langle\nu_{m_i}\right| \tag{1.13}$$

with $E_i = \sqrt{p^2 + m_i^2}$. The state $|\nu_\alpha\rangle$ at $t = 0$ evolves to

$$\left|\nu(t)\right\rangle = T \left|\nu_\alpha\right\rangle = \sum_{i=1,2,3} U^*_{\alpha m_i} \exp(-i/\hbar t E_i) \left|\nu_{m_i}\right\rangle \tag{1.14}$$

which is not necessarily a flavor eigenstate. The transition probability to a different flavor β is then

$$\begin{aligned} P_{\nu_\alpha \to \nu_\beta}(t) &= |\left\langle\nu_\beta \,|\, \nu_f(t)\right\rangle|^2 = |A(t)|^2 = |\sum_{i=1,2,3} U^*_{\alpha m_i} \exp(-i/\hbar t E_i) U_{\alpha m_i}|^2 \\ &= \sum_{i,j} U^*_{\alpha i} U_{\beta i} U_{\alpha j} U^*_{\beta j} \exp(-i/\hbar (E_i - E_j) t) \end{aligned} \tag{1.15}$$

With the ultra-relativistic approximation $v \approx c$, $L \approx ct$, which is possible due to the exceedingly low neutrino masses, we can rewrite the neutrino energy to

$$E_i = E + \frac{m_i^2 c^4}{2E} \tag{1.16}$$

with $E \approx cp$. The transition probability can then be formulated depending on the distance L traveled by the neutrino and its energy E, which are both parameters accessible in experiments:

$$P_{\nu_\alpha \to \nu_\beta}(L/E) = \sum_{i,j} U^*_{\alpha i} U_{\beta i} U_{\alpha j} U^*_{\beta j} \exp\left(-i/\hbar \frac{\Delta m^2_{ij} c^3 L}{2E}\right) \tag{1.17}$$

with $\Delta m_{ij} = m_i - m_j$. This immediately shows that oscillation experiments are sensitive to the differences in the neutrino mass spectrum only, but not to the overall mass scale of the neutrino sector. The transition probability is governed by the mass splittings and the mixing parameters of the PMNS matrix. A further approximation can be made due to the smallness of θ_{13} which has been determined only in 2012 [42][43][44]. This leads basically to a decoupling of ν_τ and the formula can be simplified to the 2ν case

$$P_{\nu_e \leftrightarrow \nu_\mu}(L/E) = \sin^2(2\Theta) \sin^2\left(\frac{\Delta m^2 c^3 L}{4\hbar E}\right). \tag{1.18}$$

In this form it gets clear that the mixing angle Θ determines the amplitude of the oscillation, while the mass splitting Δm^2 controls the frequency. The typical length associated with this oscillation is then

$$L_{osc} = \frac{4\pi\hbar E}{\Delta m^2 c^3} \tag{1.19}$$

1.3.3. Oscillation Parameters

With the introduction of the PMNS-matrix the Standard Model is extended by at least another 6 parameters that have to be determined experimentally, namely the three mixing angles θ_{12}, θ_{23}, θ_{13} and the three squared mass splittings Δm^2_{12}, Δm^2_{23}, Δm^2_{13}. Furthermore, up to 3 CP-violating complex phases have to be added depending on the nature of the neutrino. So far there exists no generally accepted, comprehensive theory of lepton

(or equivalently quark-) flavor changing that could reduce this number of parameters. Additionally, the prospects to discover new physics beyond the Standard Model has fueled neutrino physics in the last two decades. To investigate neutrino oscillations, experiments have to use a variety of sources, such as the sun, cosmic particle showers, nuclear reactors and accelerators. Oscillation experiments come in two categories: appearance and disappearance experiments. They either investigate if the neutrino flux of a certain flavor turns out to be smaller than predicted without oscillations (e.g. SNO) or they aim to detect a flavor not expected from the examined source.

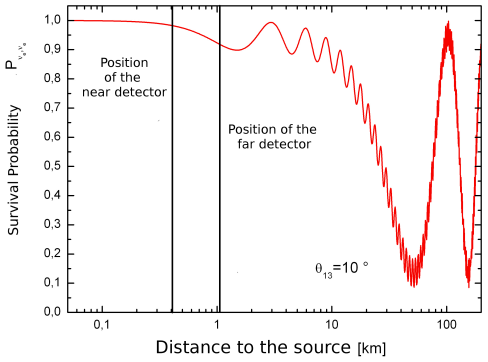

Figure 1.6.: Plot example of the theoretical expected oscillation probability for 3 MeV neutrinos over the distance with an assumed mixing angle of $\theta_{13} = 10°$ (which is close to the value measured by e.g. Double Chooz). The black lines correspond to the source distances of the near- and far-detectors of Double Chooz. Image adapted from [45]

As can be seen in figure 1.6 it is very important to tune the L/E ratio of an experiment carefully to achieve a good sensitivity for the parameter of interest. At a given energy the oscillation frequency gets large for $L \gg L_{osc}$ and only averaged transition (or survival) probabilities are measurable, while at $L \ll L_{osc}$ there barely is any oscillation. The energy of the observed neutrinos however is rarely controllable. Only accelerator experiments have a certain handle on this, so once the source is determined the experiment Lenght needs to be choosen accordingly.

A great success has been achieved in recent oscillation experiments was the detection of anti-neutrino disappearance in several reactor neutrino experiments and the measurement of the corresponding mixing angle θ_{13}. In early 2012 Double Chooz, Daya Bay and RENO announced their results

$$\text{DoubleChooz[42]} : \sin^2(2\theta_{13}) = 0.109 \pm 0.030(\text{stat.}) \pm 0.025(\text{syst.}) \quad (1.20)$$

$$\text{DayaBay[43]} : \sin^2(2\theta_{13}) = 0.089 \pm 0.010(\text{stat.}) \pm 0.005(\text{syst.}) \quad (1.21)$$

$$\text{RENO[44]} : \sin^2(2\theta_{13}) = 0.113 \pm 0.013(\text{stat.}) \pm 0.019(\text{syst.}) \quad (1.22)$$

These very similar experiments work with a two-detector concept, with one detector placed close to the reactor (300-500 m) and one further away (1-1.6 km). The near detector determines the total flux, produced by the reactor, and the far detector has to detect the loss of electron anti-neutrinos. The experiments are based on the detection principle established by the poltergeist experiments: delayed coincidence of positron signal and neutron capture. They profit from advanced scintillator development, larger detectors and carefully chosen places for the far detectors to reduce background. Their results are in good agreement with each other and with previous results from T2K [46], MINOS [47] and Double CHOOZ [48]

that had lower significance. The other mixing angles and mass splittings have already been measured, except for the sign of Δm_{23}. Pure oscillation experiments are only sensitive to Δm^2, however the sign of Δ_{12} is known from solar neutrinos. Because solar neutrinos travel through the dense sun they experience the MSW-effect [49][50], an effect resulting from propagation through matter, which is sensitive to the sign of the mass splitting. The best fit of the remaining oscillation parameters is [51]:

$$\sin^2(2\theta_{12}) = 0.857 \pm 0.024 \tag{1.23}$$
$$\Delta m^2_{12} = (7.50 \pm 0.20) \cdot 10^{-5}\ \mathrm{eV}^2 \tag{1.24}$$
$$\sin^2(2\theta_{23}) > 0.95\ (90\%\mathrm{C.L.}) \tag{1.25}$$
$$\Delta m^2_{23} = (2.32 + 0.12 - 0.08) \cdot 10^{-3}\ \mathrm{eV}^2 \tag{1.26}$$

1.3.4. Models of neutrino mass

In the Standard Model (SM) no neutrino masses and therefore no mechanism generating them are foreseen. The observation of neutrino oscillations and the so-far determined very small upper limits on the masses themselves (factor $> 10^5$ smaller than e^-) are hints to physics beyond the SM. Especially the smallness relative to the masses of other particles in the SM led to the assumption that the neutrino masses might be generated by a mechanism different from the standard Higgs mechanism. Otherwise a fine-tuning of the Higgs couplings ,which translate into the masses, is necessary. A popular alternative is the see-saw mechanism which will be briefly layed out in its simplest version. Full treatment can be found in the literature this section is based on e.g.[52].

To account for a neutrino mass in the SM Lagrangian analogously to the other leptons, terms in the form of

$$L^{\mathrm{D}}_{\mathrm{mass}} = -\frac{1}{2}\sum_{\alpha,\beta} \bar{\nu}_{\beta\mathrm{L}} M^{\mathrm{D}}_{\alpha\beta} \nu_{\alpha\mathrm{R}} + h.c. \tag{1.27}$$

can be introduced, thereby completing the neutrino's Dirac Lagrangian. It is summed over all flavors with L, R denoting the chirality of the fields, that is the part that is projected out by $(1 \pm \gamma^5)/2$. We see immediately that this requires also the introduction of right handed neutrino fields ν_R that are not part of the SM. These new ν_{R} states would not take part in the weak interaction and hence are called sterile. In this scenario the Higgs mechanism could be invoked to generate the mass terms in a gauge invariant way. This is unappealing due to the extremely fine-tuned Yukawa coupling of $\sim 10^{-13}$ needed in this scenario

Another possibility was brought up by E. Majorana. It is possible to construct a mass term without referring to the right handed field ν_R. Instead its role is played by $C\nu_L$

$$L^{\mathrm{M,L}}_{\mathrm{mass}} = -\frac{1}{2}\sum_{\alpha,\beta} \bar{\nu}_{\beta\mathrm{L}} M^{\mathrm{D}}_{\alpha\beta} \nu^C_{\alpha\mathrm{L}} + h.c. \tag{1.28}$$

This term causes lepton number violation e.g. in double beta decay and implies that a Majorana neutrino is its own anti-particle.

It is also possible to invoke both mass terms and add also a Majorana term for the right handed neutrino. When collecting all these terms in a Dirac-Majorana term

$$L^{D+M} = L^D + L^{M,L} + L^{M,R} \tag{1.29}$$

with the neutrino fields combined in the vector

$$N_{\mathrm{L}} = \begin{pmatrix} , \nu_{\mathrm{L}} \\ (\nu_{\mathrm{R}})^C \end{pmatrix} \tag{1.30}$$

the mass term can be written as

$$L^{D+M} = -\frac{1}{2} N_{\mathrm{L}} M N_{\mathrm{L}}. \tag{1.31}$$

Here M denotes the mass matrix (for a single neutrino now for simplicity)

$$M = \begin{pmatrix} m_{\mathrm{L}} & m_{\mathrm{D}} \\ m_{\mathrm{D}} & m_{\mathrm{R}} \end{pmatrix}. \tag{1.32}$$

The eigenvalues of this matrix determine the physical neutrino masses observed. In the simplest form of the See-Saw mechanism $m_{\mathrm{L}} = 0$ and $m_{\mathrm{D}} \ll m_{\mathrm{R}}$ is assumed. In this case the matrix' diagonalization gives

$$m_1 \approx \frac{m_{\mathrm{D}}^2}{m_{\mathrm{R}}} \qquad m_2 \approx m_{\mathrm{R}}. \tag{1.33}$$

One very small mass m_1 and a rather large mass m_2 is found, naturally giving rise to the small neutrino mass. The heavy state consists mostly of ν_{R} and hence is sterile.

1.4. Measurements of the neutrino mass

Since oscillation experiments can only measure squared mass splittings, further measurements are needed to determine the absolute neutrino masses. Indirect methods include observations of the large scale structure of the universe and searches for neutrinoless double beta decay. Both methods are heavily model dependent. Direct searches rely purely on kinematics and measure beta decay spectra using either bolometers or electron spectroscopy. Until today only upper limits on the absolute neutrino mass scale are known.

1.4.1. Indirect neutrino mass measurements

1.4.1.1. Cosmological measurements

Neutrinos play an important role in cosmology. Their exclusively weak interaction and small mass imply that they contribute to the hot dark matter component in the universe. Due to their predicted vast abundance of 336 neutrinos per cubic centimeter left from the big bang , the so-called cosmic neutrino background ($C\nu B$), they do give a measurable contribution to the matter-energy density of the universe in spite of their small mass, see fig. 1.7. While relic neutrinos have not been detected directly, indirect evidences exist.

Due to their low mass, neutrinos do not contribute to the dominant cold dark matter (CDM) component. The currently prevailing model of the universe is the ΛCDM model. It describes the universe today as dominated by the cosmological constant Λ and CDM. Both are not understood on a fundamental level. The cosmological constant is only described in the classical Einstein equation[54][55][56][57]

$$R_{\mu\nu} - \frac{1}{2} g_{\mu\nu} R + \Lambda g_{\mu\nu} = \frac{8\pi G}{c^4} T_{\mu\nu}. \tag{1.34}$$

However it is often regarded residual energy of vacuum fluctuations of the other quantum fields, similar to the zero-point energy $\hbar\omega/2$ of a harmonic oscillator. A particular problem with this interpretation is the smallness of the cosmological constant, which can not be explained within the SM. This is one motivation for super symmetry. A full understanding of the cosmological constant may in the end require quantum gravity.

While there are many indirect evidences for CDM in the universe, e.g. galactic rotational curves [58], weak lensing [59] and the bullet cluster [60][61], no direct evidence has been

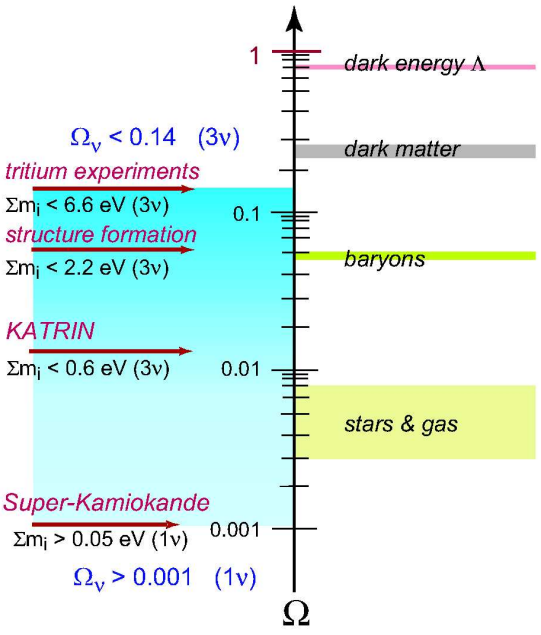

Figure 1.7.: Relative contributions to the matter-energy densitiy of the universe from different sources and experimental bounds on the neutrino mass density. KATRIN aims to improve the sensitivity of previous tritium experiments by one order of magnitude. Image from [53].

found yet. Many experiments search for dark matter candidates, the weakly interacting massive particles (WIMPs), predicted by different theories. Such WIMP candidates are e.g. the lightest supersymmetric particles..

The ΛCDM model is an inflationary big-bang cosmology, consistent with the cosmologic microwave background [62][63] (CMB), that has been measured with high precision by satelite experiments such as WMAP [64] and Planck [65].

Due to their low mass and weak interaction, neutrinos are able to travel through the universe unperturbed on cosmological scales, so-called free-streaming. They decoupled from the remaining matter about 1 s after the big bang, when they were still highly relativistic, with energies on the order of 1 MeV. Consequently, they suppressed the formation of structures in the universe on scales below their free-streaming length. In fig.1.8 the influence of neutrino mass on this process can be seen.

The matter distribution of the universe is accessible in experiments measuring the CMB, galaxy surveys and the Lyman-alpha-forest. In cosmology only the sum of the neutrino masses can be accessed. A combined analysis of cosmological data gives [66]:

$$\sum_i m_{\nu_i} \leq 0.51 \text{ eV } (90\% \text{ C.L.}). \tag{1.35}$$

This upper bound however is strongly model dependent [67]. More conservative bounds exist and large variations are common, depending on which model and data set are used.

1.4.1.2. Neutrinoless double beta decay

Double beta decay is a rare second order process. It can only be observed if a single beta decay of an even-even nucleus to the neighboring odd-odd-nucleus is forbidden by energy conservation. In the nucleus two β^- decays happen simultaneously:

$$2n \rightarrow 2p + 2e^- + 2\bar{\nu_e} \tag{1.36}$$

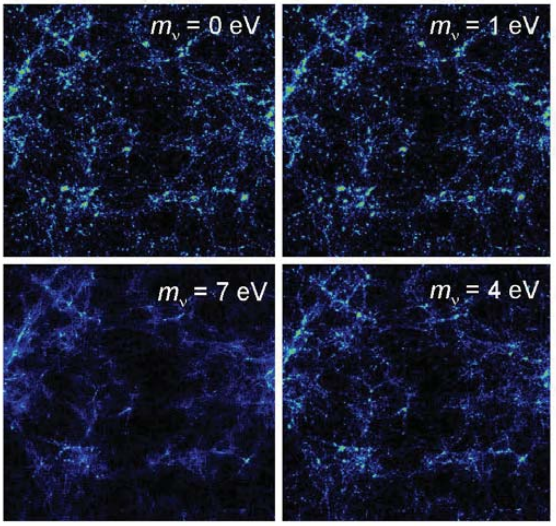

Figure 1.8.: Influence on the neutrino mass on the structure formation in the universe. Larger neutrino masses lead to stronger 'wash out' of the small scale structures. Figure from [53].

or

$$(A, Z) \rightarrow (A, Z+2)^{2+} + 2e^- + 2\bar{\nu}_e \tag{1.37}$$

Since it is a second order-process the decay rates are low and typical half-lives are very long. The first observation was in 1987 on the isotope ^{82}Se[68] after it was first proposed for ^{76}Ge in 1935[69]. Today $2\nu\beta\beta$ decays are known to occur for 12 isotopes out of the 60 for which it would in principle be possible. If neutrinos are Majorana particles and hence their own anti particles, another process is possible, the neutrinoless double beta decay ($0\nu\beta\beta$). The $0\nu\beta\beta$ decay was proposed by G. Racah[70] and W. Furry[71] after Majoranas work[28]. Instead of emitting two neutrinos in the final state, a 'virtual' neutrino is exchanged, flipping from an outgoing anti neutrino at one vertex to an incoming neutrino at the other vertex, as seen in fig. 1.9.

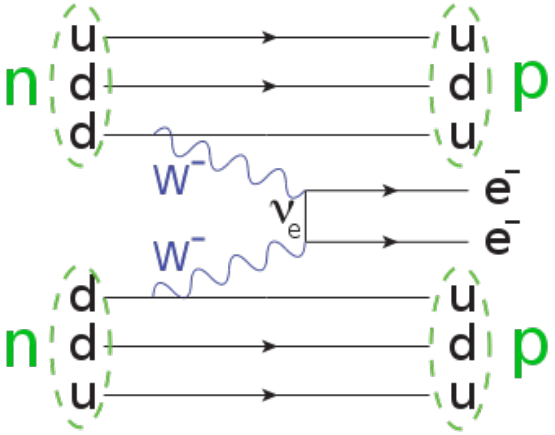

Figure 1.9.: Feynman diagram for neutrino less double beta decay.

This is only possible for massive Majorana neutrinos. In contrast to single beta decay and ordinary double beta decay, the summed energy spectrum of the emitted electrons in neutrinoless double beta decay is discrete and sharply peaked, since the virtual neutrino

can not carry away energy or momentum. This process violates lepton number conservation by two units and would indicate physics beyond the SM. In principle loops of new particles coupling to the neutrino could also contribute to the process, and consequently to the neutrino mass. From the observation of neutrinoless double beta decay a neutrino mass can be deduced:

$$m_{\beta\beta} = \left| \sum_i U_{ei}^2 m_{\nu_i} \right| = \frac{1}{G^{0\nu} |M^{0\nu}|^2 \tau_{1/2}^{0\nu}}. \tag{1.38}$$

Here $\tau_{1/2}^{0\nu}$ is the measured half-life of the decay, $M^{0\nu}$ the nuclear matrix element for the transition and $G^{0\nu}$ the phase space factor. One important aspect is that unlike single beta decay measurements, neutrinoless double beta decay is sensitive to the *coherent* sum of the neutrino mass eigenstates. Due to the Majorana nature of the neutrino in this case, the Majorana phases come into play and allow for cancellation in this sum. The deduced mass is therefore also model dependent. The Heidelberg-Moscow collaboration published a result claiming the observation and a corresponding neutrino mass $m_{\beta\beta} \approx 0.4$ eV[72], which is not accepted in general, due to a disputed analysis method. Many experiments e.g. CUORE, GERDA and EXO are currently searching for neutrino less double beta decay using different isotopes and different experimental setups to test the claim from Heidelberg-Moscow. Recently, the GERDA collaboration has published their phase I results, which do not support the earlier observations [73].

1.4.2. Direct neutrino mass measurements

Direct neutrino mass measurements purely rely on the kinematics involved in neutrino production. Although the highest sensitivity in neutrino mass search is achieved when investigating β^--decay, also experiments with muons und tau leptons were conducted.

1.4.2.1. Beta decay kinematics

The β^- decay is a weak nuclear decay. It converts a neutron into a proton, an electron and an anti electron-neutrino.

$$(A, Z) \rightarrow (A, Z+1) + e^- + \bar{\nu}_e. \tag{1.39}$$

On a fundamental level, a down quark converts to an up-quark via emission of a W^- boson. The W^- boson then decays into an electron and an anti electron-neutrino as depicted in the feynman diagram 1.10. Neutrino, electron and nucleus share the decay energy. The nuclear recoil can be largely neglected due to the much larger nuclear mass compared to the electron and the neutrino. Since a fraction of the decay energy is needed to create the neutrino with its mass, the electron's spectral shape is influenced by the neutrino mass. Fermis theory[5] gives for the energy spectrum

$$\frac{dN}{dE} = C \cdot F(E,Z) p_e (E_e + m_e c^2)(E_0 - E_e) \sqrt{(E_0 - E_e)^2 - m_{\nu_e,\text{eff}}^2} \tag{1.40}$$

$$C = \frac{G_F}{2\pi^3} \cos^2 \Theta_C |M|^2. \tag{1.41}$$

Here E_e, p_e ,m_e denote the electron energy, momentum and mass, E_0 the endpoint energy and $F(E,Z)$ the Fermi factor that accommodates the electron's interaction with the Coulomb potential of the nucleus. G_F is the Fermi constant, Θ_C the Cabibbo mixing angle[41] between up- and down-quark states and $|M|^2$ the nuclear matrix element. The main influence of the neutrino mass on the spectral shape originates from the phase space factor, since the Fermi function and the nuclear mass element are independent of $m_{\nu_e,\text{eff}}$.

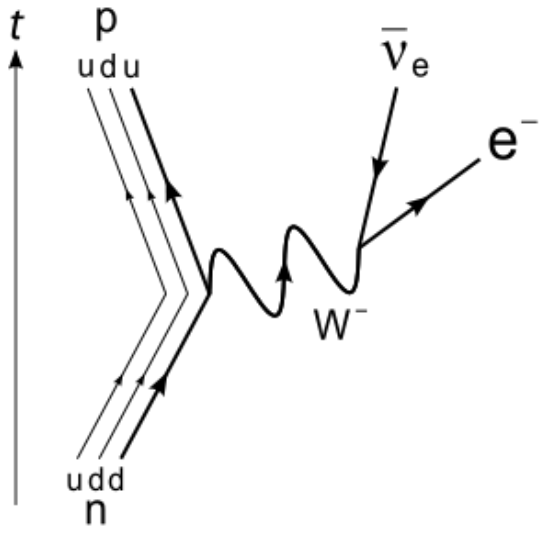

Figure 1.10.: Feynman diagram of the β^- decay

In super-allowed decay processes the nuclear matrix element is also energy independent, simplifying the relation. Theoretically, highly sensitive experiments could resolve even the individual mass eigenstates in

$$m^2_{\nu_e,\text{eff}} = \sum_i |U_{ei}|^2 m^2_{\nu_i}. \tag{1.42}$$

However by current means of technology this is not achievable due to the tiny mass splittings and the resolution achieved in spectroscopic experiments. While in principle the neutrino mass could be determined from the energy difference between the measured end of the spectrum and the theoretical endpoint E_0 for a vanishing neutrino mass, this is not feasible because the endpoint is not known precisely enough and the experimental sensitivity is limited by the background rate in the region of vanishing count rates. Instead, the mass is deduced from the relative shape of the spectrum near the endpoint. There, the neutrinos are not ultra-relativistic anymore and the neutrino mass influences the spectral shape.

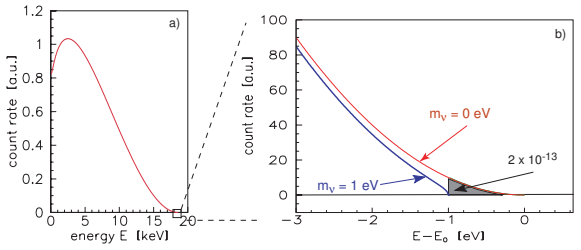

Figure 1.11.: Electron energy spectrum of tritium β-decay. The neutrino mass manifests itself only in a narrow region close to the endpoint, as seen in b). Hence, neutrino mass measurements are challenged by the requirement of a high resolution spectral scan in a region of very low count rates. [53]

1.4.2.2. Bolometric experiments

One approach to the neutrino mass pushed forward in experiments mainly in Italy is the measurement of the β-spectrum using cryogenic micro-calorimeters. In this type of

experiment the source simultaneously serves as detector. After a beta decay a rise of temperature in the detector is measured by thermistors adjacent to it. The main benefit of this approach is the fact that the decay electrons deposit their entire energy in the detector and can be measured. A drawback is that always the complete spectrum is measured simultaneously, resulting in large pile-up effects if the total decay rates are not kept sufficiently low, thereby reducing the statistical sensitivity Therefore it is important for these experiments to select a beta emitter with a low endpoint energy. Rhenium is the beta emitter with the lowest known beta endpoint of 2.67 keV. The disadvantage is its exceedingly long half life of $T_{1/2} = 10^{10}y$, so large amounts of Rhenium are needed to provide sufficient statistics for a neutrino mass measurement. Due to the pile up effects this can not be put in one single detector, but an array of many small detectors has to be build. This approach is taken by the MARE experiment that builds on the expertise of its predecessors MANU and MIBETA. In the MIBETA experiment an upper bound on the neutrino mass[74]

$$m_{\bar{\nu}_e} \leq 15 \text{ eV } (90\% \text{ C.L.}) \tag{1.43}$$

was found. The MARE experiment aims to improve this limit by more than an order of magnitude and is currently taking data with a set of 72 detectors[75].

1.4.2.3. Tritium experiments

The most stringent direct and model independent bounds on the neutrino mass have been set by the Mainz and Troitsk tritium experiments.

$$\text{Mainz[76]} \quad : \quad m_{\nu_e} \leq 2.3 \text{ eV } (95\% \text{ C.L.}) \tag{1.44}$$

$$\text{Troitsk[77]} \quad : \quad m_{\nu_e} \leq 2.05 \text{ eV } (95\% \text{ C.L.}) \tag{1.45}$$

They analyzed the Tritium beta decay:

$$^3_1\text{T} \rightarrow ^3_2\text{He} + \text{e}^- + \bar{\nu}_e \tag{1.46}$$

Tritium has a variety of benefits as beta emitter for neutrino mass measurements layed out in 2.2.1. Both, Mainz and Troitsk used an electrostatic spectrometer and setup of the kind that the KATRIN experiment will take to its limits. Hence, the KATRIN experiment stands at the frontier of a long history of tritium beta decay experiments [78].

2. The KATRIN Experiment

The **Ka**rlsruhe **Tri**tium **N**eutrino experiment [53] aims for a model-independent measurement of the effective mass of the electron anti-neutrino $m_{\bar{\nu_e}}$ with a sensitivity of 200 meV (90% C.L.). The nearly 70 m long experimental setup is being build at KIT Campus North near Karlsruhe (Germany) and will be a significant scale-up of previous tritium neutrino experiments in Mainz [79][76] and Troitsk [80][81]. Like its predecessors, KATRIN will analyze the shape of the tritium β-spectrum close to the endpoint of $E_0 \approx 18.6$ keV with a spectrometer of the MAC-E-filter type[1]. Continuing developments at Troitsk KATRIN will use a **W**indowless **G**aseous **T**ritium **S**ource (WGTS) that will be installed at the Tritium Laboratory Karlsruhe (TLK). Due to its 2 decades of experience with tritium technology and the necessary allowance to process the required 40 g/Day of molecular tritium in a closed loop TLK is the ideal facility for this task. The WGTS has to deliver a luminosity $> 10^{11}$ Bq for the KATRIN experiment. To improve the sensitivity by one order of magneitude as compared to predecessor experiments, KATRIN not only needs to push the technical limits in terms of scale but also in control of statistical and systematical uncertainties. This Chapter contains an introduction to the basic measurement principle in section 2.1, a detailed description of the experimental setup and its different components in section 2.2 and a discussion on the experimental sensitivity and discovery potential of KATRIN in section 2.3.

2.1. Measurement Principle

As discussed in the last chapter, the neutrino mass can be extracted from the shape of the ^{3}T β-spectrum close to its endpoint. Due to the very low count rates in this region - a fraction of 10^{-13} of all decays occurs in the energy region of interest, resulting in a count rate of 10^{-2} counts per second (cps)- a high luminosity source and spectrometer, meaning many decays and keeping a high portion of them analyzable, are needed to provide sufficient statistics. Furthermore, a sharp energy resolution is needed for a precise analysis of the spectral shape. These requirements are met by the MAC-E-Filter that acts as a high-pass-filter for electrons with an energy $eU$where e denotes the elementary charge and U the filter potential. An electron-counting detector will then provide an *integral* spectrum.

2.1.1. MAC-E filter

The MAC-E-Filter principle was first proposed by Picard et al. [82] and a simple scheme is displayed in figure 2.1. All of the different spectrometers (pre-, main- and monitor-

[1] **M**agnetic **A**diabatic **C**ollimation with **E**lectrostatic filter

spectrometer) in the KATRIN setup are built according to this principle. It works through a combination of an axial-symmetric magnetic field and a retarding potential U_0 within the spectrometer. The retarding potentials acts only along the beamline, the z-axis, and can only analyze the kinetic energy stemming from the Z-momentum $E_{\parallel} = \frac{p_z^2}{2m}$ at maximum potential. As the tritium decay is isotropic the electron momenta need to be parallelized along the beam line. Ideally the kinetic energy

$$E_{\text{kin}} = E_{\parallel} + E_{\perp} \tag{2.1}$$

at the maximum of the retarding potential consists of $E_{\parallel}$ only. The degree to which this condition is broken will define the energy resolution of the spectrometer. The magnetic field is generated by two solenoids on the beam axis at the entrance and exit of the spectrometer. Due to the Lorentz-force charged particles will be guided adiabatically on a cyclotron motion around the field lines. The particle's first adiabatic invariant

$$\gamma\mu = \frac{\gamma + 1}{2} \cdot \frac{E_{\perp}}{B} \tag{2.2}$$

is to a high degree conserved, with the relativistic Lorentz factor γ and the magnetic moment of the particle μ. Hence in the non-relativistic regime the orbital magnetic moment $\mu = E_{\perp}/B$ is conserved. Since the magnetic field strength drops from the solenoids to the mid of the spectrometer by a factor of ~20000, $E_{\perp}$ is reduced accordingly. Consequently the minimum of the magnetic field strength and the maximum of the retarding potential need to coincide in the center of the spectrometer. This requirement is called *transmission condition* and the cross section of the spectrometer where it is fulfilled is called *analyzing plane*. An electron with a vanishing longitudinal kinetic energy at the analyzing plane will

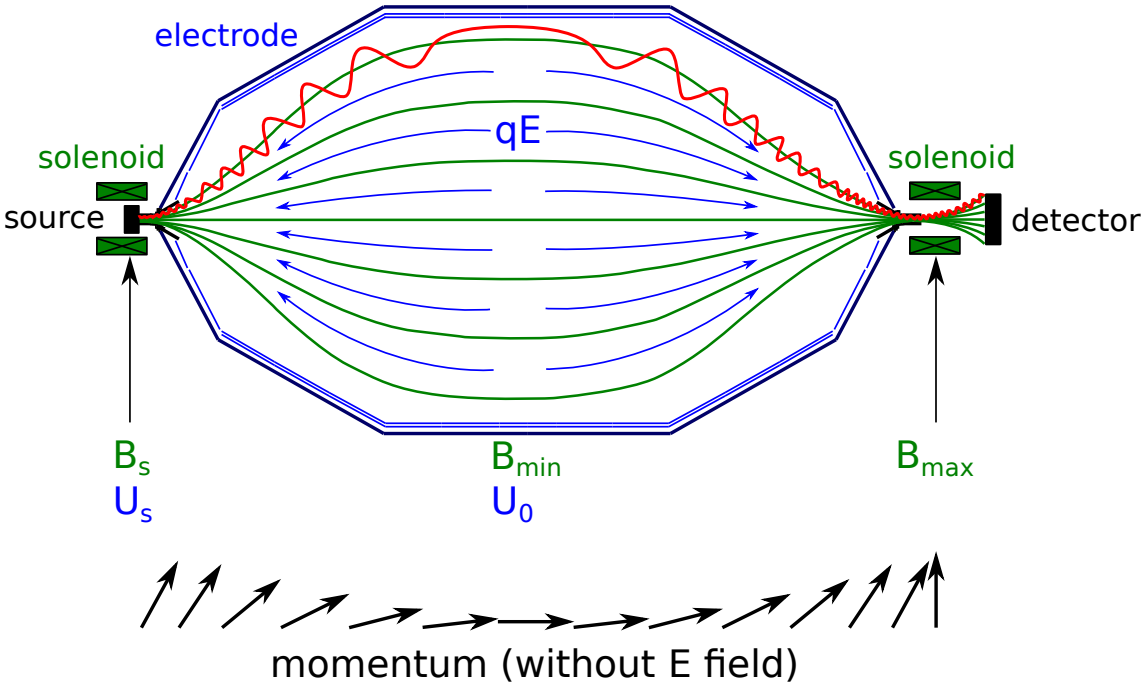

Figure 2.1.: Scheme of the MAC-E filter. Image from [83][83].

not get transmitted but reflected back to the source. The electron energy can be determined except for a small fraction which remains in the transversal energy component as the magnetic field in the analyzing plane cannot be reduced to zero. From the conservation of μ we get

$$\frac{\Delta E}{E} = \frac{B_{\text{min}}}{B_{\text{max}}} \tag{2.3}$$

For the tritium endpoint energy $E = 18.6$ keV, an analyzing magnetic field strength $B_{\text{min}} = 3 \cdot 10^{-4}$ T and a maximal field strength $B_{\text{max}} = 6$ T, the energy resolution $\Delta E = 0.93$ eV is obtained, which corresponds to the fraction of the electron energy inaccessible by the MAC-E filter. Because this very good energy resolution requires such a large decrease of the magnetic field, the flux tube is widened substantially - necessitating the enormous dimensions of the KATRIN main spectrometer. In addition to the potential barrier there is the effect of *magnetic reflection* [84]: When electrons move along the magnetic field lines to a higher magnetic field, the perpendicular components of the electron momenta are increased. If a polar angle of 90° is reached the electron is magnetically reflected. The maximal accepted starting angle can be computed by

$$\theta_{\text{max}} = \arcsin\left(\sqrt{\frac{B_{\text{S}}}{B_{\text{max}}}}\right) = 50.77^{\circ} \tag{2.4}$$

with $B_{\text{S}} = 3.6$ T denoting the starting magnetic field strength and $B_{\text{max}} = 6$ T. This particular value indeed is a design choice: the angular acceptance of a MAC-E-filter can range up to 2π. But electrons with a large polar angle are less favorable for the analysis because of their larger path length and hence, scattering probability in the source. Due to the consequent energy losses, they would contribute significantly to the systematic uncertainty of the measurement.

2.1.2. Transmission function

All effects influencing the transmission of electrons through the spectrometers manifest themselves in the *transmission function*. In its simplest form it gives the transmission probability depending on the electron starting energy and the retarding potential. Similary the *response function* describes the entire experiment taking also effects from the source into account. The transmission function is highly sensitive to the interplay of electric and magnetic fields and can be resolved in many different ways, introducing angular, radial and further dependencies. Full idealization would yield a Heavyside function: only electrons above the energy threshold are transmitted. Using the assumptions of adiabacity , i.e. a conservation of the orbital magnetic moment, and an isotropic angular distribution for the source, the transmission function can be analytically derived. With the magnetic field strength at the source B_{S}, the electron start energy E, the analyzing potential U_0, electron charge q, maximal (pinch) magnetic field strength B_{max} and magnetic field in the analyzing plane B_{A} the transmission function can be written as:

$$T(E, qU) = \begin{cases} 0 & \text{if } E - qU_0 < 0 \\ \dfrac{1-\sqrt{1-\frac{E-qU}{E}\cdot\frac{B_{\text{S}}}{B_{\text{A}}}}}{1-\sqrt{1-\frac{B_{\text{S}}}{B_{\text{max}}}}} & \text{if } 0 < E - qU < \Delta E \\ 1 & \text{if } \Delta E < E - qU \end{cases} \tag{2.5}$$

The transmission probability strongly depends on the electron's starting angular distribution. Electrons at higher starting polar angles require more energy to be transmitted, as their transformation of $p_{\perp}$ into $p_{||}$ is less efficient.

2.1.3. Response function

It was discussed above that the probability for electron transmission through the spectrometer is given by the transmission function T. This information, however, is not sufficient to determine the tritium β-spectrum from a measurement, since scattering in the source is

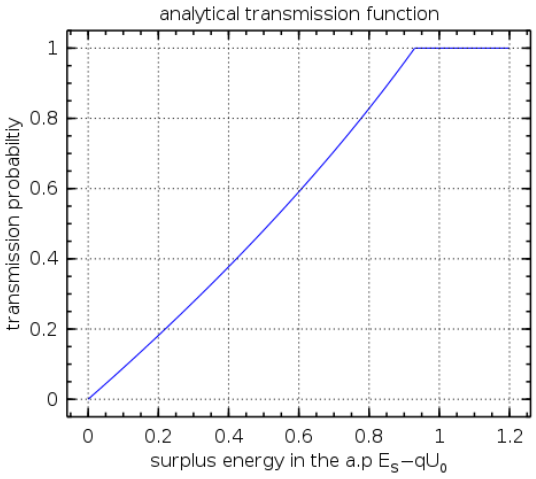

Figure 2.2.: Transmission function for electrons propagating along the beam line, emitted by an isotropic source. This transmission function is already normalized, taking into account magnetic reflection for starting angles above 50.1°

completely unaccounted for. for design values of the column density ρd only about 40% of all decay electrons reach the spectrometer without undergoing inelastic scattering off the tritium molecules in the WGTS. This is why the *response function* of the experiment needs to be considered. It is a convolution of the source- and spectrometer-properties reflecting the transmission properties of the spectrometer section and the scattering probabilities in the source. The scattering is characterized by the (normalized) energy loss function

$$f(\Delta E) = \frac{1}{\sigma_{\text{tot}}} \frac{d\sigma}{d(\Delta E)}. \tag{2.6}$$

with ΔE being the energy loss and σ_{tot} the total scattering cross section. The energy loss function also has an angular dependence, but this is negligible for small energy losses of electrons within the analysis range of 30 eV below the endpoint. The response function is obtained by convoluting the transmission function with the electron energy loss probability ϵ:

$$R(E, qU) = \int_0^E d\epsilon T(E - \epsilon, qU) \left(P_0 \delta(\epsilon) + P_1 f(\epsilon) + P_2 (f \otimes f)(\epsilon) + \dots\right) \tag{2.7}$$

The general shape of the response function is shown in figure 2.3. The energy loss function found in the literature is not known precisely enough for a theoretical determination of the response function. Therefore it will be determined in an extra measurement before the dedicated tritium measurements. This will be done using mono-energetic electrons provided by the rear section (see 2.2.2). Since there exist radial as well as azimuthal inhomogeneities in the experiment, the response function needs to be determined over the whole cross section of the source. Radial dependencies are introduced by the density profile of the WGTS, azimuthal ones by a necessary breaking of the rotational symmetry.

2.2. Experimental Setup

KATRIN combines an extremely stable high-luminosity molecular tritium source with a variable and precise MAC-E-filter. By counting the transmitted electrons for various retarding potentials an integrated spectrum can be recorded. Figure 2.4 displays a schematic

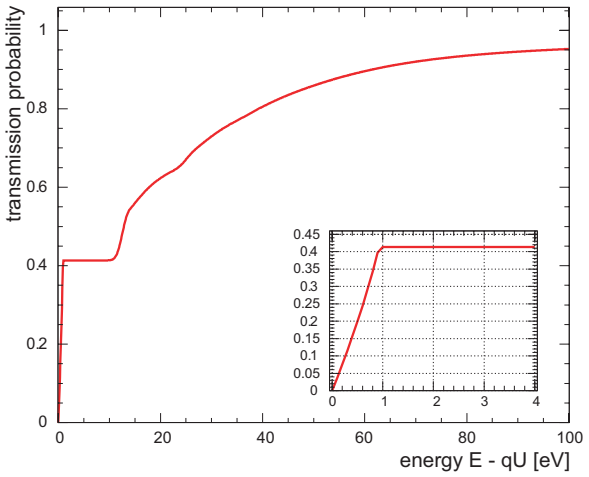

Figure 2.3.: KATRIN repsone function at reference values for the magnetic field B and column density ρd: $B_S = 3.6\ T$, $B_{\min} = 3 \cdot 10^{-4}\ T$, $\rho d = 3 \cdot 10^{17}\ \mathrm{cm}^{-2}$. The two bumps indicate the thresholds of one-fold and two-fold scattering. Below 10 eV the response function basically coincides with the transmission function since this is the minimum energy loss for inelastic scattering at tritium. Slight changes to the shape originate from the altered angular distribution. Image taken from [85]

drawing of the experimental setup with its different subsections: the source, transport section, spectrometers and detector.

2.2.1. Tritium source

KATRIN will use a **W**indowless **G**aseous **T**ritium **S**ource[87]. Tritium decays according to

$$^3_1\mathrm{H} \rightarrow {}^3_2\mathrm{He} + \mathrm{e}^- + \bar{\nu_e} \tag{2.8}$$

The hydrogen isotope tritium as β-source has a number of advantages for measuring the neutrino mass:

- Tritium has a comparably **low endpoint of 18.6 keV**. Since the total activity of the source scales as $\Gamma \propto Q_0^4$ and the relative fraction of electrons in the vicinity of the endpoint as $\Gamma \propto Q_0^{-3}$ a moderate dependence of the rate in the region of interest on Q_0 results.
- ^3_1T **has a short half life of only 12.3 a.** This ensures a high rate per mol allowing low source densities and even a gaseous source. This is a great benefit for systematic uncertainties due to scattering effects of the electrons in the source.
- The transition $^3_1\mathrm{H} \rightarrow {}^3_2 He$ **is a super-allowed β-decay** as it occurs between mirror nuclei. As a consequence the matrix element is easy to compute, energy independent and rather large.
- $^3_1\mathrm{H}$ **has the lowest possible Z value** and thus a simple electronic structure. This is advantageous for the computation of the final state spectrum and scattering processes, both very important for the understanding of source systematics. Also the resulting cross section for inelastic scattering is overall low.

Besides a high luminosity, a source suitable for KATRIN needs to have very low and well understood systematic uncertainties. The WGTS will reach an activity of $\sim 10^{11}$ Bq

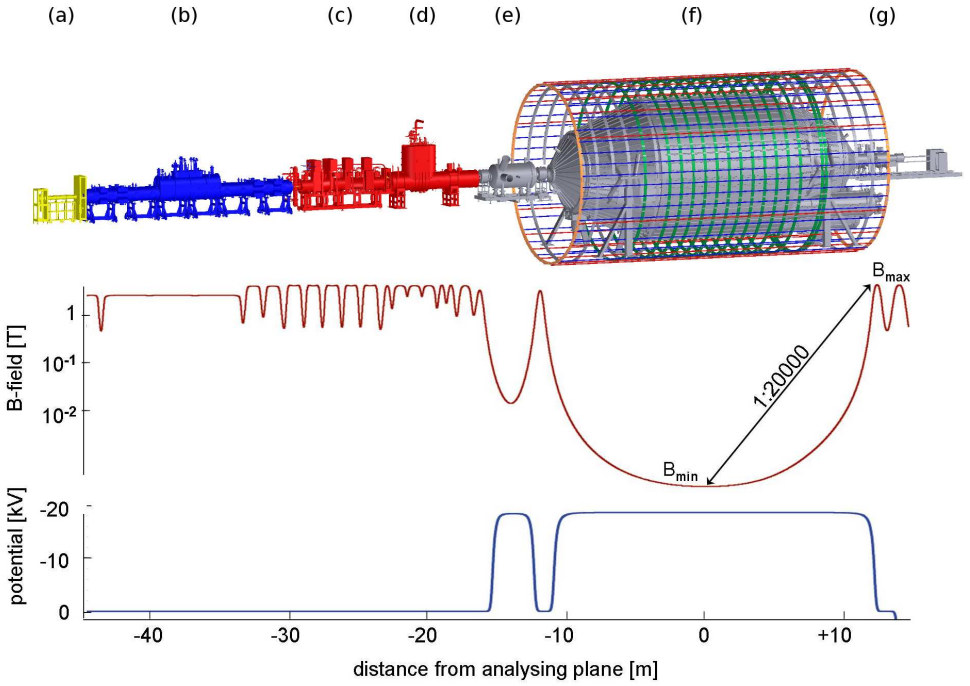

Figure 2.4.: The 70 m long KATRIN experimental setup, together with the magnetic field and electric potential along the Z-axis. In different colors: **a)** the rear section (yellow) for monitoring the source potential, **b)** the WGTS (blue) a high luminosity tritium source, **c)** the **D**ifferntial **P**umping **Section** and **d)** the **C**ryogenic **P**umping **S**ection (both red) for preventing inflow of tritium into the spectrometers, the Spectrometer-Detector-Section (SDS grey) consisting of **e)** prespectrometer for filtering the low-energy part of the β-spectrum , **f)** mainspectrometer for high resolution analysis of the β-spectrum and **g)** detector for counting the transmitted electrons. Image from [83]

by injecting cold (27° K) high purity ($\geq$ 95%) tritium gas in the center of the 10 m long, 90 mm diameter stainless steel beam tube. Tritium will diffuse, from the point of injection in the center of the WGTS to both ends resulting in an overall column density of $\rho d = 5 \cdot 10^{17}$ cm^{-2}. At each end of the WGTS a 3 m long pumping section (DPS-1F, DPS-1R) will pump out the tritium gas with TMPs and re-inject it in the closed tritium (inner) loop [88] for purification to prevent a waste of tritium and contamination of the transport and spectrometer section. This measure already reduces the tritium flow from the source to the other sections by two orders of magnitude.

Because the column density defines the source luminosity it has to be known very precisely i.e. only deviations below 0.1% can be tolerated. This leads to stringent requirements for the source temperature. The allowed fluctuations have to stay below $\Delta T \leq 30$ mK. The required cooling will be provided by a two phase neon system that has already been tested in the WGTS demonstrator [89][90] and actually outperformed this bound [91].

The low temperature of 27° K is on the one hand required to suppress plasma effects of the tritium gas that would lead to a charge-up of the source and therefore to a higher systematic error of the source potential. And on the other hand it minimizes the Doppler shifts that broaden the β-spectrum and contribute to the systematic error of the spectrum. It is the lowest possible temperature without the tritium molecules starting to cluster, which again would raise the systematics.

Figure 2.5.: CAD drawing of the WGTS including the DPS-1F and DPS-1R on seperate stands. Figure taken from [86]

Further systematical errors that have to be dealt with include fluctuations of the tritium purity and the final state distribution of the $^3HeT^*$ daughter molecules. The final state distribution arises from rotational, vibrational and electronic excitations that modify the β-electrons energy. Precise calculations of the final state distribution are needed to account for this [92][93]. To correct for the tritium purity fluctuations the Laser Raman system LARA [94][95] is set up at TLK that will provide a fast determination of the isotopic composition of the tritium gas by raman spectroscopy of the total tritium flow.

In the WGTS the decay electrons are guided by a 3.6 T magnetic field created by several superconducting solenoids around the beam tube. It forms a magnetic flux tube of 229 Tcm^2 over the whole source cross section. However, only an inner flux tube of 191 Tcm^2 (corresponding to 3.3 T, the magnetic flux at the detector) will be analyzed since in the outer parts scattering off the walls can occur and disturb the measurement. The electrons travel to both ends of the WGTS leaving either towards the transport section or the rear section. So half the activity can actually be later on analyzed in the spectrometer section.

The WGTS is currently under construction by an industrial partner and will be delivered to KIT in spring 2015. It will be situated at TLK and connected to the downstream components in the KATRIN hall only through a feed through in the wall as a measure for tritium safety.

2.2.2. Rear section

The rear section, situated at the back end of the DPS1-R, will serve several purposes:

- monitoring the source activity by **B**eta **I**nduced **X**-ray **S**pectroscopy BIXS [96]
- defining the source potential
- measuring the column density with an high intensity electron gun
- mapping the KATRIN response function across the whole flux tube using the electron gun

The potential will be set by the rear wall that also functions as target for the BIXS. Through a small central hole in the rear wall electrons from the electron gun will be allowed to enter the beam tube. They can be used to measure the response function and to keep the tritium plasma quasi-neutral. A full scan of the flux tube will be possible with the use of additional

magnetic dipoles for deflection. These measurements will be done repeatedly and allow a close monitoring of the source parameters, which is very important to control its systematic effects [87].

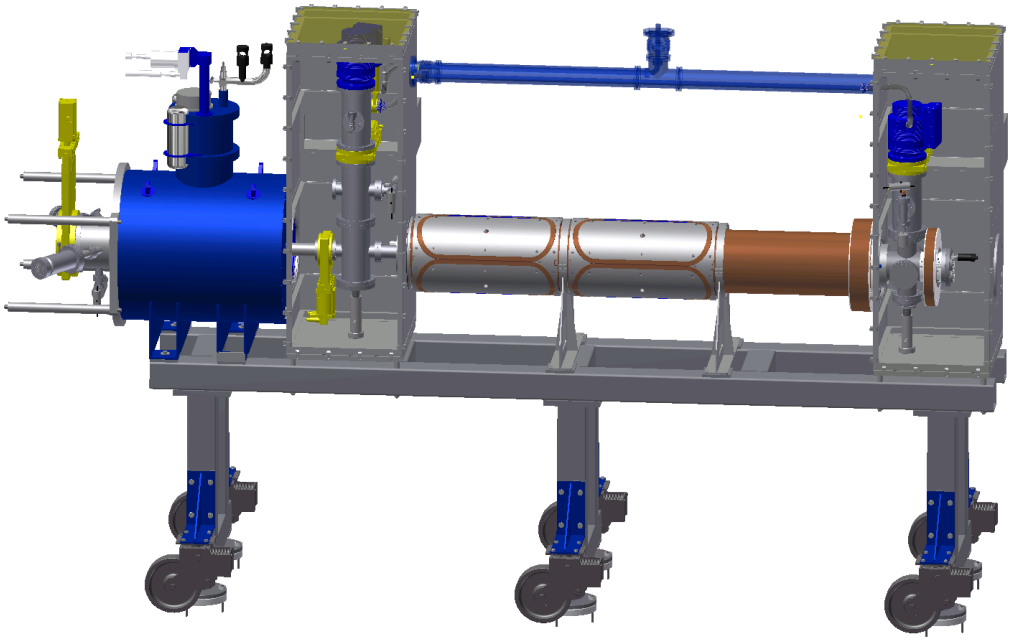

Figure 2.6.: Technical design of the Rear section. Figure taken from [97].

2.2.3. Transport section

The transport section consists of two subsystems: the **D**ifferential **P**umping **S**ection and the **C**ryogenic **P**umping **S**ection. Both have the same general purpose , a reduction of the tritium flow from the source to the spectrometers by 14 orders of magnitude and an adiabatic guidance of the electrons to the spectrometer section.

A tritium inflow to the main spectrometer would be fatal, in large amounts for the radiation safety concept on the one hand, but also extremely small amounts of tritium in the main spectrometer lead to a significant background, severely harming the KATRIN sensitivity. A partial pressure of less than 10^{-20} mbar [98] in the main spectrometer is required to keep this background lower than 10^{-3} cps[99].

2.2.3.1. Differential Pumping Section

The DPS will reduce the tritium flow by 5 orders of magnitude. For this purpose it uses 4 strong turbo molecular pumps housed in pump ports between the 5 superconducting solenoids that create the guiding magnetic field in the beam tubes. The beam tubes run through the warm bores of the solenoids and are, as the solenoids, tilted by 20° with respect to each other. This prevents a direct line of sight between source and spectrometer section, avoiding the molecular beaming effect [100]. The DPS will be instrumented with extra tools to measure and remove ions from the flux tube as these are neither pumped by the TMPs nor blocked by the tilting because they follow the field lines. The ion content will be determined with the FT-ICR [101][102] (Fourier Transform Ion Cyclotron Resonance) method: the ions are caught in a Penning trap and their cyclotron frequency is measured. As they circle around in the trap the periodically induced charge on a close electrode is measured. A Fourier transform of the signal gives the e/m spectrum.

Ion removal is done - similar to methods used in the spectrometers - by the short application of an electric dipole field. The resulting $\vec{E}\times\vec{B}$-drift moves the ions over the course of several

cyclotron motions to the wall. For this special electrodes are integrated into the system [103][104][105].

This large effort is necessary because the β-decay in the source creates a variety of ions in quantities as large as the signal electron's rate. The decay products ${}^{3}_{2}\mathrm{HeT}^{+}$ can dissociate and recombine with T_2 as well as other hydrogen isotopologues in the source.

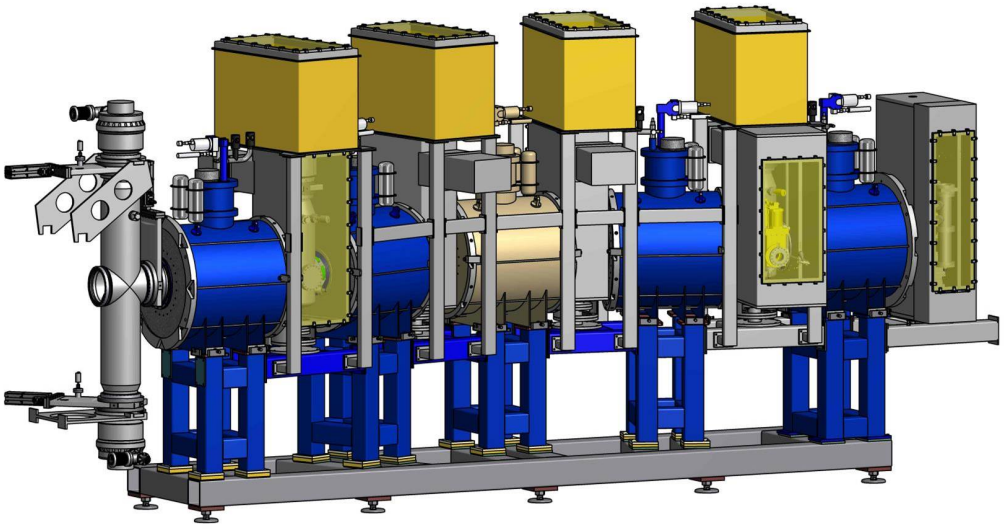

Figure 2.7.: DPS with its 5 solenoids for adiabatic guidance of the electrons in a magnetic field of up to 5.5 T. 4 TMPs are used for tritium retention. Image taken from [83]

2.2.3.2. Cryogenic Pumping Section

As the DPS the tritium flow can not be efficiently reduced further with TMPs, an additional section is needed based on the principle of cryo-sorption. It will reduce the tritium flow towards the spectrometers by 7 orders of magnitude [100][106], so that the overall tritium retention from the WGTS to the spectrometer section will be a factor of 10^{14}. The inner surfaces of the beam tubes of the CPS are held at 3° K and will be covered by argon frost. This strongly enlarges the cold inner surfaces and thus enhances the effective pumping speed. Any tritium or hydrogen molecule that hits the wall will freeze and stick to it. Like the DPS it uses tilted beam tubes to prevent molecular beaming. Another 7 superconducting solenoids will create the magnetic guiding field for the signal electrons.

2.2.4. Spectrometer section

The KATRIN experiment uses all together three spectrometers, all built according to the MAC-E-filter principle layed out in section 2.1.1. Whilst the pre- and main spectrometer are set up in line with the source and the detector to filter the β-decay signal electrons, the monitor spectrometer resides in a separate building. Its purpose is to monitor the high voltage of the main spectrometer. All three spectrometers are described in the following.

2.2.4.1. Pre-spectrometer

The pre-spectrometer is set up to to pre-filter the low-energy part of the β-spectrum that contains most of the signal electrons coming from the source. These electrons are irrelevant for the neutrino mass measurement, as the effect of the neutrino mass only is visible in the last few electron volt below the endpoint. It is situated between the CPS and the

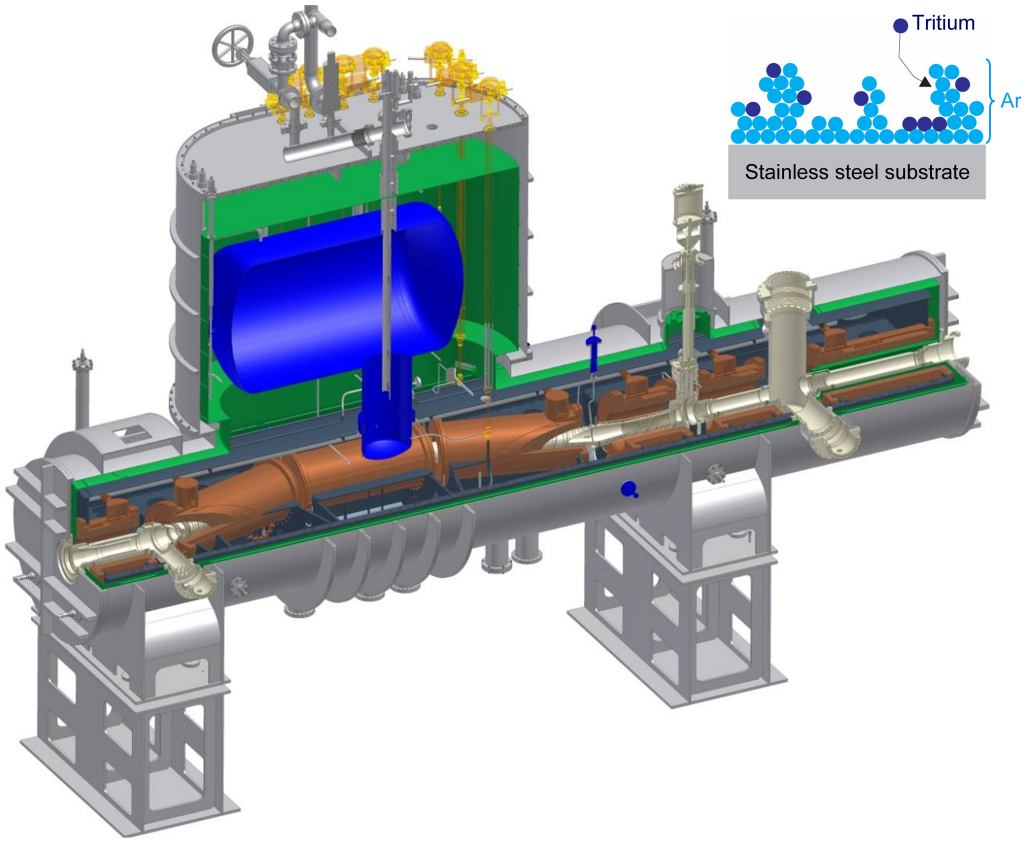

Figure 2.8.: Cryogenic Pumping Section. Image taken from [98]

main spectrometer. It can achieve a maximum magnetic field in the solenoids of 4.5 T and a retarding potential of −18.3 kV. In this setting it would reduce the electron flow into the main spectrometer by a factor of 10^7 [107]. The pre-spectrometer was used to test techniques later incorporated in the main spectrometer and for research into background generation mechanisms of MAC-E-filters. This includes methods of active (magnetic pulse, electric dipole, ECR) and passive (cryo-baffles) background reduction. Most importantly the radon isotopes ^{219}Rn and ^{220}Rn) emanating from the steel of the vessel as well as from the getter pumps could be identified as a significant source of background and suitable design decisions for the main spectrometer could be made.

2.2.4.2. Main spectrometer

The main spectrometer poses a particular challenge due to its enormous dimensions. With a length of 23.6 m and a diameter of 10 m, its total volume amounts to 1250 m^3, not including the LFCS and EMCS air coil systems. Figure 2.10 gives an impression of it.

The scale of the spectrometer is directly connected to the required energy resolution. Since the resolution depends on the ratio of $\frac{B_{\text{min}}}{B_{\text{max}}}$, the magnetic field has to drop by a factor of 20000 from the pinch magnet to the analyzing plane. This leads to a drastic widening of the flux tube.

The magnetic field is mostly created by the 4 solenoids near the main spectrometer: the 2 pre-spectrometer solenoids PS1 and PS2, the pinch solenoid PCH, capable of B-fields up to 6 T and the detector magnet DET, responsible for the precise imaging of the flux tube onto the detector. Additional a large air coil system [108], consisting of 14 coils surrounding the vessel, is needed to fine tune the magnetic field in the analyzing plane where the design magnetic field is as low as $\sim 300\ \mu$T. Therefore, the influence of the earth magnetic field

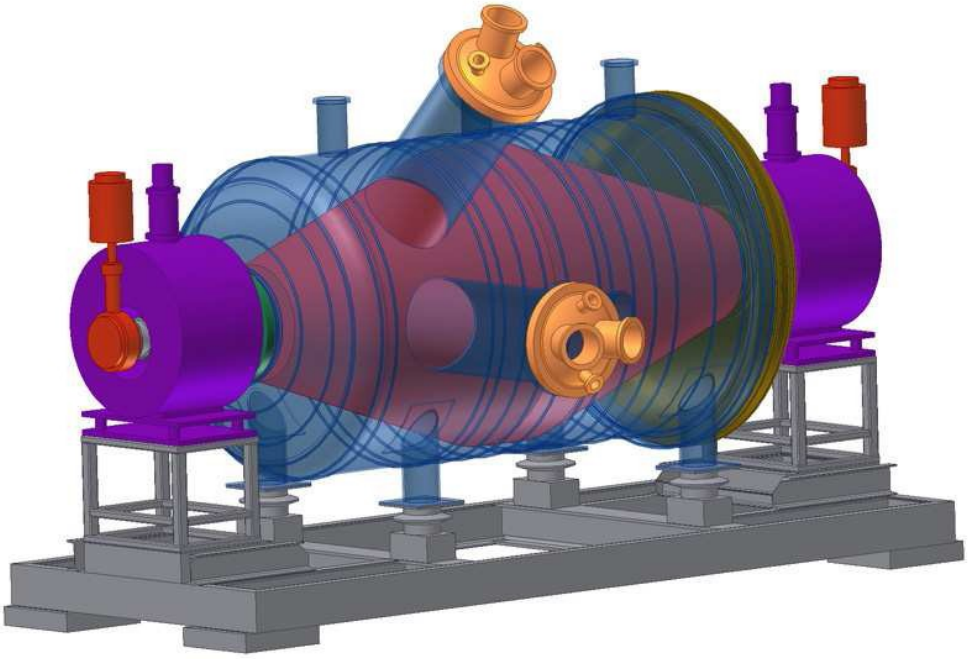

Figure 2.9.: The pre-spectrometer vessel (blue), with the 2 solenoids (purple), and the inner electrode system (red). Figure taken from [86]

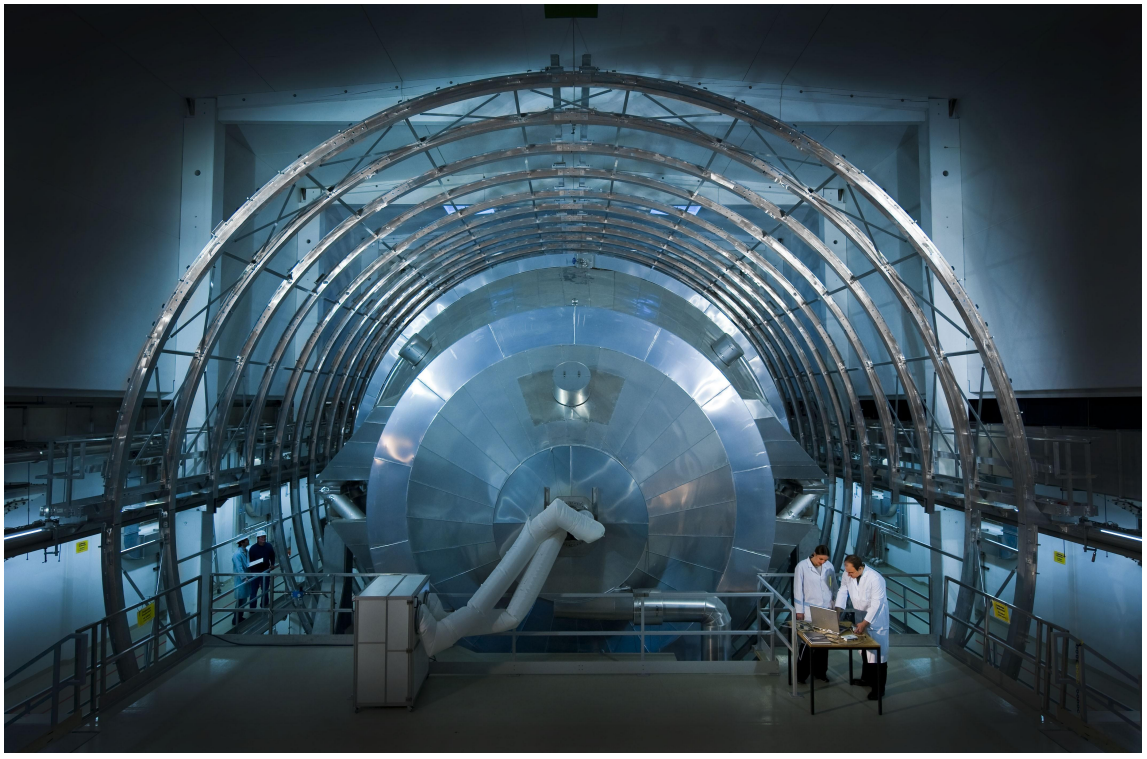

Figure 2.10.: The KATRIN main spectrometer surrounded by the air coil system. (photo: KIT)

(EMF), with a total field strength of 48 μT can not be neglected. Consequently, an Earth Magnetic Field Compensation System (EMCS) is needed.

In contrast to the Mainz and Troitsk experiments, the vessel of the main- as well as the pre-spectrometer is put on voltages and an inner electrode system is used to fine shape the potential. In case of the main spectrometer, this electrode system is nearly massless: it consists of 24000 thin (200-300 μm) wires organized in 248 modules in a double layer configuration [109][110]. It is designed to create a high precision and very homogeneous potential in the spectrometer volume as well as to shield the volume from background electrons originating at the wall that are induced by cosmic rays [111][112]. The screening is achieved by running the two layers of wires on different potentials where only the inner wire layer is set to the full analyzing potential.

Besides the electromagnetic field the most challenging demand on the main spectrometer is to achieve an ultra high vacuum of $< 10^{-11}$ mbar in a volume of 1250 cubic meters. This is necessary to ensure that the signal electrons are not perturbed by scattering off the residual gas on the one hand. On the other hand it suppresses an important mechanism of background generation: cascades of secondary electrons are induced as stored electrons scatter off residual gas molecules and ionize them. The vacuum system consists of 6 cascaded TMPs (Leybold MAG-W-2800) and 3 km of non-evaporable getter strips (NEG, SAES St707, 60 kg in total) will work. The TMPs can pump all gases and have even for hydrogen a pumping speed of 10^4 ℓ/s. For hydrogen, the dominant gas in the main spectrometer, however, the passive NEG pump is much more powerful with a pumping speed of 10^6 ℓ/s [113][114][115].

In the course of this thesis the commissioning of the main spectrometer from outbaking, alignment, background studies to first transmission measurements with an angular resolved e-gun as source took place. This was an important step towards the completion of the KATRIN experiment involving many people for the different systems and fields of expertise. The background studies and measurements of the main spectrometer form an important part of this thesis and will be reported on in section 4.

2.2.4.3. Monitor spectrometer

The monitor spectrometer is the fromer spectrometer of the Mainz experiment, that has been shipped to KIT and is housed in a separate building. The distance to the main beam line is kept to minimize the influence of stray fields on the transmission properties of the main spectrometer. Its purpose is to monitor the high voltage of the main spectrometer. Since the retarding potential defines the energy threshold of the transmission, this parameter has to be known very precisely and stabilized at the ppm level to reach the design sensitivity. The monitor spectrometer's retarding potential is fed by the same voltage as the main spectrometer. It will use a quench condensed krypton source as nuclear standard. By a repeated measurement of the 17.8 keV ^{83m}Kr K-32 conversion line, small shifts of this line will indicate fluctuations of the high voltage [116][117][118]. The monitor spectrometer is equipped with a silicon PIN-diode detector, an EMCS as well as 4 air coils. It is operational and taking data since 2012 [119][120].

Additional to the monitor spectrometer the voltage will be measured with the help of precision high voltage dividers developed in cooperation with the Physikalische Technische Bundesanstalt in Braunschweig[121]. These are also stable on the ppm level and give an output voltage of less than 10 V suitable for state of the art high precision volt meters.

2.2.5. Focal plane detector

The **F**ocal **P**lane **D**etector is situated at the downstream end of the beam line. It consists of a 90 mm diameter 148 pixel silicon PIN-diode wafer to count the few electrons ($\sim 10^{-2}$ cps)

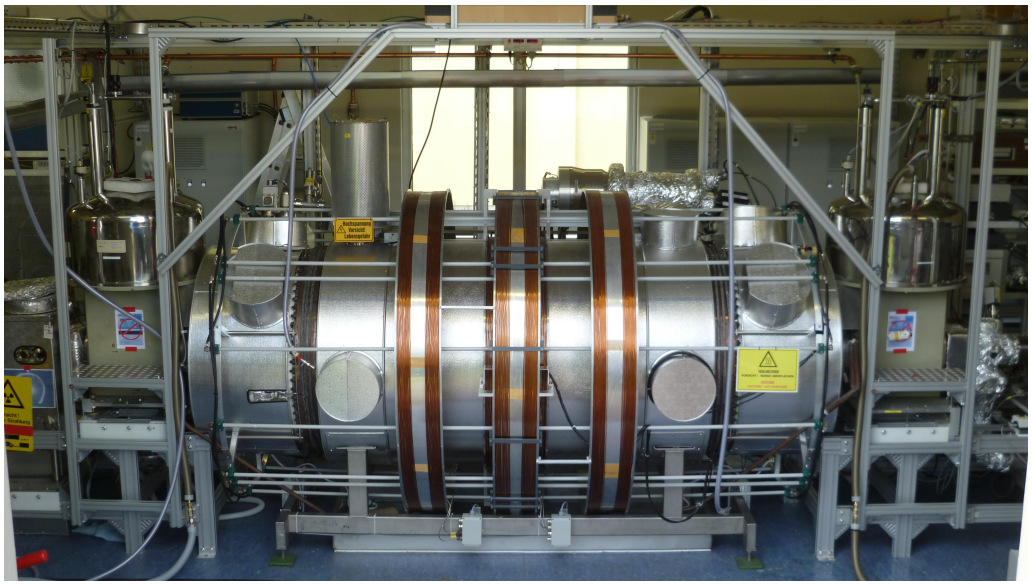

Figure 2.11.: Picture of the operational monitor spectrometer. (photo: M. Erhard [118])

that will be transmitted through the spectrometers. These low rates put high demands on the detector efficiency and intrinsic background. To achieve a low background of less than 10^{-3} cps, passive measures such as lead shielding and careful material selection aiming at a low intrinsic radioactivity have been taken and are supported by an active muon veto system. A post acceleration electrode is installed and will allow to shift the signal by up to 30 keV into a region of lower background. The detector has a moderate energy resolution of 1 keV (FWHM) at 18.6 keV to discriminate between background and signal electrons. It is equipped with two sources for energy calibration, an ^{241}Am γ-source and an UV-lighted titanium disk for electrons of energies up to 25 keV.

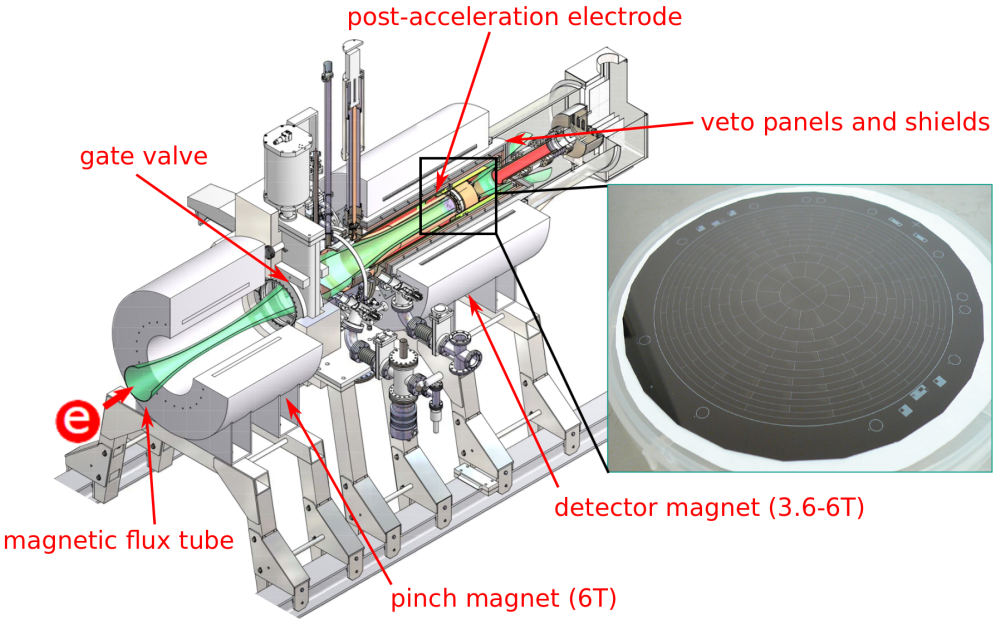

Figure 2.12.: Scheme of the FPD system and a picture of the detector wafer before integration. Image taken from [122]

2.3. Sensitivity

The KATRIN experiment aims to measure the effective anti-neutrino mass $m_{\bar{\nu}_e}$ with a sensitivity of $m_\nu \leq 200$ meV (90%C.L.). To improve the the neutrino mass sensitivity by one order of magnitude as compared to the Mainz and Troitsk experiments statistical and systematical uncertainties need to be reduced by two orders of magnitude. The KATRIN error budget thus may not exceed

$$\sigma_{abs} = \sqrt{\sigma_{sys}^2 + \sigma_{stat}^2} \leq 0.025 \text{ eV}^2. \tag{2.9}$$

To extract the neutrino mass from the measured rates a comparison with the theoretically expected rates needs to be done. Since KATRIN measures a convolution of the differential energy spectrum with its response function, the expected signal rate is calculated according to

$$N_s(qU, E_0, m_\nu) = N_{tot} t_U \int_0^{E_0} dE R(E, qU) \frac{dN}{dE}(E_0, m_\nu) \tag{2.10}$$

where N_{tot} is the number of tritium nuclei in the source and t_U the measuring time at the potential U. Taking into account a constant background N_b with a signal-to-noise ratio R_s/R_b we get

$$N_{th}(qU, E_0, m_\nu, R_s, R_b) = R_s N_s(qU, E_0, m_\nu) + R_b N_b \tag{2.11}$$

To get the neutrino mass, the free parameters $E_0,\ m_\nu,\ R_s$ and R_b have to be fitted.

2.3.1. Statistical uncertainty

The design value of KATRINs statistical uncertainty is $\sigma_{stat} = 0.018 \text{ eV}^2$. This corresponds to a pure measurement time of 3 years which results in 5 calendar years runtime including maintenance and calibration. A low background rate is key to achieve a good statistical uncertainty. Not only the rate, but also possible time- and energy- dependencies have a big influence on the statistical uncertainty. Also, depending on the background the measurement time distribution for the different retarding potentials needs to be optimized, to push the statistical uncertainty as low as possible. While close to the endpoint the sensitivity to the neutrino mass is largest, the very low count rates there also require low background rates. Further away from the endpoint, the signal rates are larger, but the influence of the neutrino mass gets significantly lower, enforcing longer measurement times for the same sensitivity. Also, systematic uncertainties due to scattering of the signal electrons gets bigger further away from the endpoint.

Multiple possible sources of backgrounds have to be under control in the KATRIN experiment:

- **Detector background**: due to the energy resolution $\Delta E \approx 1$ keV of the detector, any event in this region around the endpoint contributes to the background of the measurement. However a post-acceleration electrode is installed to shift the region-of-interest (ROI) to regions of lower background if necessary.

  Cosmic particles hit the detector and deposit energy, thereby creating background events. A muon veto system is in place to filter most of them from the data set.

  Nuclear decays can occur due to residual radio-active nuclei in the detector. To prevent this the detector materials were selected carefully.

  High energy photons can originate from natural radioactivity in the surrounding.

- **Spectrometer background**: Since all electrons that reach the detector from the inside of the spectrometer are accelerated by the analyzing potential, any low energetic electron is pushed to the investigated energy and presents potentially dangerous background.

  Secondary electrons from cosmic particles or gamma radiation can hit the spectrometer vessel, and especially the inner electrodes. Electrons from the vessel are largely shielded by the axial symmetric magnetic field and the 200 V potential difference between vessel and inner electrode (IE). Low-energy electrons from the IE, however, also are accelerated into the ROI.

  Field emission due to imperfect surfaces at the IE also would produce low-energy electrons similar to cosmic rays. Much care was taken to prevent this in the design and construction of the inner electrode system.

  Radioactive decays in the volume of the main spectrometer create electrons that are stored in the magnetic bottle inherent to the field configuration of the spectrometer, and escape randomly onto the detector. One source is tritium that makes its way from the source to the spectrometer. This is to be prevented by the transport section that suppresses the tritium flow by 14 orders of magnitude. An other source are radon (219,220) atoms emanating from the material of the getter pump (219) or the walls (220).[123][124][125][99]

  stored particles can ionize the residual gas in the spectrometer and create secondaries, which can themselves be stored.

  Penning traps store particles locally and can generate huge background rates through Penning discharges. They have to be avoided by careful electromagnetic design.

2.3.2. Systematical uncertainty

The systematic uncertainty of the KATRIN experiment on the (squared) neutrino mass is aimed to stay below $\sigma_{sys} \leq 0.017$ eV. To achieve this, the key parameters like the retarding voltage and source activity have to be controlled thoroughly. Systematic effects that have to be taken care of are

- Radiative corrections to the theoretical beta spectrum
- Corrections to the spectrum from the final state distribution of the helium daughter molecules
- Corrections to the spectrum from nuclear recoil
- Corrections to the spectrum from Doppler-broadening due to the brownian motion of the tritium molecules
- Scattering of signal electrons in the WGTS (or transport section)
- Synchrotron losses of the electrons during the transport
- Variations in the source activity. They will be monitored by the rear wall and the LARA-system and kept low by the temperature stability of the WGTS
- Variations of the retarding potential. These will be monitored by the monitor spectrometer.
- Variations of the background rate.
- Any non-adiabatic effects on the electrons.

3. Simulation Software: The KASPER Package

Computer simulations are a necessary tool for detailed investigations of the spectroscopic properties and mechanisms of background generation of the MAC-E-filters in the KATRIN experiment. Ranging from the computations of e.g. the expected tritium β-spectra, over electron scattering in the source, electron or ion transport, to background generation from radon decays or cosmic muons, all aspects of KATRIN are covered by simulations to ensure a precise understanding of all effects that have an influence on the neutrino mass measurement. In this chapter, the KASPER software package, developed in collaboration between UNC, MIT, University of Münster and KIT, is introduced. It is designed to integrate the different algorithms needed for field computations, particle tracking, scattering, source- and detector simulations into a unified suite that is easily extendable and configurable via XML. The KASPER software package integrates the particle tracking program KASSIOPEIA[126][127], the electric and magnetic field computation framework KEMField, the near time analysis software BEANS, the database access module KALI[128] and the geometry tool KGeoBag[127]. A brief introduction into electric and magnetic field computations with KEMField is given in3.1. The KASSIOPEIA program is discussed in 3.2 since it is heavily used later on to investigate background generation in the main spectrometer and possible countermeasures. Finally, the approach taken in the course of this thesis to tackle simulations of stored particles is presented in section 3.3.

3.1. KEMField

KEMfield [129][130] is the field computation module integrated into the KASPER package. It can operate with fully three dimensional geometries, exploit axial symmetry, provides support for MPI and GPUs (via OpenCL). Geometry input is possible through KGeoBag in XML input files or legacy plain text files for compatibility. Other field codes are also shipped with KASPER, especially for magnetic fields within KASSIOPEIA. However, KEMField provides by far the most advanced and comfortable framework for field computations within KASPER, integrating most of the functions of the other field codes. What so far is not implemented in KEMField are the Biot-Savart and magnetic dipole methods needed for precise calculations of the EMCS-Field and the inhomogeneities induced by magnetic materials.

3.1.1. Electric field computation

KEMField performs electric field computation using the **B**oundary **E**lement **M**ethod (BEM[131][132]). The following linear equation is to be solved

$$U_i = \sum_j C_{ij}\sigma_j, \tag{3.1}$$

where U_i is the voltage applied to an electrode, σ_i the charge density that results from this voltage and C_{ij} is the Coulomb matrix element representing the influence of the electrode j on the electrode i. The Coulomb matrix contains purely geometrical information and its elements are computed according to

$$C_{ij} = C_i(\vec{r}_j) = \frac{1}{4\pi\epsilon_0}\int_{S_j}\frac{1}{\vec{r}_i - \vec{r}_S}d^2r_S, \tag{3.2}$$

where the integral runs over the surface of the jth electrode element. To solve the Coulomb matrix KEMField provides several methods:

- Gauss elimination
- LU-method
- Robin Hood method[133]

They are build to make use of parallel computing. The Robin Hood algorithm has a better scaling behavior than the first two for which the computing time grows as N^2, with N denoting the number of elements. This especially gets important for the full three dimensional model of the main spectrometer which has about 4 million elements. After the charge densities are computed usually the electric field and/or potential has to be evaluated for further computations e.g. within particle tracking. For this purpose KEMField provides a method based on zonal harmonic expansion and direct summing of the subelement contributions. Furthermore, a spherical multipole expansion for fast field evaluation in fully three dimensional geometries is being tested.

The direct method sums up the contributions of each element to the potential at a certain point. Generally, the subelements can be treated as point charges. Only close to the electrodes expressions depending on the geometry of the subelements have to be used. However, for triangles and rectangles corresponding analytical formulas do exist and are being used. This is also true for the computation of the electric field. Only if the analytical evaluation fails the electric field is computed by numerical derivation.

The zonal harmonic expansion (ZHE) is based on Legendre polynomials. The expansion coefficients are computed at certain sourcepoints on the symmetry axis. After this time consuming process is done once, the field can be evaluated very fast. This method, however, relies on the axial symmetry of the setup. Since this is a good approximation for many uses in the KATRIN setup, it is widely used. The ZHE is based on the following representation of the potential

$$\Phi_{cen}(r,z) = \sum_{n=0}^{\infty}\Phi_n^{cen}|_{z_0}(\frac{\rho}{\rho_{cen}})^n P_n(\cos(\theta)) \tag{3.3}$$

$$\Phi_{rem}(r,z) = \sum_{n=0}^{\infty}\Phi_n^{rem}|_{z_0}(\frac{\rho}{\rho_{rem}})^{-(n+1)} P_n(\cos(\theta)) \tag{3.4}$$

$$\tag{3.5}$$

where ρ is the distance to the source point and $\rho_{cen/rem} = \sqrt{(z-z_0)^2 + r^2}$. The Φ_n are the source coefficients that have to be computed. These two expansions differ in their convergence behavior. While the central expansion only converges inside a convergence radius r_c, the remote expansion does so outside of such an radius.

3.1.2. Magnetic field computation

The KATRIN experiment has numerous coils and solenoids to precisely shape the magnetic field that guides the signal electrons along. Their degree of adiabaticity and the precision of the energy analysis in the main spectrometer depend crucially on a very precise calculation of the magnetic fields, which is provided by KEMField. Some of the methods described here, however, are so far not available within KEMField and shipped with KASSIOPEIA separately.

In general, the magnetic field generated by a current is described by the Biot-Savart law:

$$\mathbf{B} = \frac{\mu_0}{4\pi} \int_C \frac{I d\vec{\mathbf{l}} \times \vec{\mathbf{r}}}{|\mathbf{r}|^3} \tag{3.6}$$

The contour integral runs over the path C of the current I and $\vec{r}$ points from the line segment $d\vec{\mathbf{l}}$ to the position the field is calculated at. In case of coils with thousands of windings, this integral would be very slow to compute numerically,so analytic methods are used in KEMField instead. These are based on elliptic integrals which can be used to compute the field at any point. Since the computation of the elliptic integrals is still rather slow (field computation accounts for a majority of the computing time needed), and since the coils are, at least locally, axially symmetric, again a zonal harmonic expansion is used. In a last step, the fields of the separate coils are superimposed to yield the total magnetic field of the configuration.

3.2. Particle tracking with KASSIOPEIA

The KASSIOPEIA package is built to simulate particle trajectories in the whole KATRIN setup. It is configured via XML files and provides a wide range of possibilities to generate, track and stop particles. Particle interactions are included, e.g. electron scattering on residual hydrogen atoms or energy deposition in the detector (handled by the KESS[134] module). KASSIOPEIA makes use KEMField and further methods to calculate the electric and magnetic fields needed to determine the trajectories.

3.2.1. Tracking methods

KASSIOPEIA offers multiple methods to track particles in magnetic and electric fields. Particle trajectories are calculated with the help of different Runge-Kutta algorithms that can be selected to solve the ODE. The default choice is an embedded Runge Kutta algorithm of 8th/6th order with internal error estimation. To define the particle's trajectory, different trajectory types can be selected for propagation. The most simple trajectory is a straight line, which can be directly generated from the particle's initial velocity without the need for the Runge-Kutta algorithm. To follow a certain magnetic field line, a so-called "magnetic trajectory" is computed using the Runge-Kutta algorithm to adjust the particle momentum to point in the direction of the magnetic field. With this tool magnetic field settings can be visualized by field lines. Furthermore there one can choose to track charged particles in the fields using the exact Lorentz equation, or an adiabatic approximation. In both cases a term to include the effect of synchrotron radiation can be switched on. In addition to these different possibilities of trajectory calculation, there exist several algorithms for step size control to choose from. Besides setting a simple *fix* step size either in length or in time, also one of the following precision criterion can be chosen. With an *energy* step size control, a step is accepted if the energy violation of the step is below a user-defined level, of typically on the order of 10^{-13} relative error. Furthermore since the curvature of the trajectory is largely controlled by the strength of the magnetic field, an adaptive *cyclotron* step size control is possible. In this case, the cyclotron period $T = 2\pi\frac{m_0\gamma}{qB}$ is

subdivided into a fix number of steps. If this number is chosen to be smaller than one, a single step spans more than one cyclotron period. If several step size controls are active at the same time, the step gets re-evaluated till the strongest criterion is met.

3.2.1.1. Exact tracking

Exact tracking uses the Runge-Kutta ODE solver to solve the exact Lorentz equation

$$\vec{F}_L = q(\vec{E} + \vec{v} \times \vec{B}). \tag{3.7}$$

Since the ODE-solver only solves systems of first order ODEs, this needs to be reformulated to

$$\frac{d\vec{r}}{dt} = \frac{\vec{p}}{\gamma m} \tag{3.8}$$

$$\frac{d\vec{p}}{dt} = q(\vec{E}(\vec{r},t) + \frac{\vec{p} \times \vec{B}(\vec{r},t)}{\gamma m}) \tag{3.9}$$

This is the propagation term.

Since the electrons from the source perform cyclotron motions around the guiding magnetic field lines, thereby describing strongly curved trajectories, they emit synchrotron radiation. Synchrotron radiation was first discovered in a synchrotron accelerator at General Electric [135] and is a dreadful effect in high energy particle physicis (HEP). It is emitted coherently over the whole electro-magnetic frequency band whenever a charged particle describes a curved trajectory. Due to this effect, modern HEP particle accelerators and storage rings are forced to take the enormous sizes of an LHC to achieve low synchrotron losses and high energies by minimizing the curvature of the particle's path. Within the KATRIN experiment synchrotron losses of the signal electrons are a systematic effect that has to be taken into account.

In KASSIOPEIA synchrotron radiation is dealt with on a classical level as a term added to the ODE. This so called Abraham-Lorentz-Dirac[136] force has raised a lot of debate in the past since, in a theoretical understanding, it is highly problematic, seemingly violating causality and energy conservation in special situations. On the one hand, for a particle at rest exponential runaway-solutions exist. On the other hand, for a time-dependent external force causality is violated: The particle starts acceleration before the force acts. There exists, however, a quantum description[137] that avoids these fallacies. Nevertheless, this topic still is worked on today [138][139][140]. Fortunately, these controversial situations do not occur in the case of KASSIOPEIA simulations, allowing an application of this method. The relativistic version of the (classical) force term, first proposed by Dirac[136] is

$$F_\mu^{\mathrm{rad}} = \frac{\mu_o q^2}{6\pi mc}\left[\frac{d^2 p_\mu}{d\tau^2} - \frac{p_\mu}{m^2 c^2}\left(\frac{dp_\nu}{d\tau}\frac{dp^\nu}{d\tau}\right)\right]. \tag{3.10}$$

The corresponding radiation power is

$$P = \frac{\mu_0 q^2 a^2 \gamma^6}{6\pi c}. \tag{3.11}$$

For our purpose, this has to be reformulated into a system of first order ODEs. This was done for KASSIOPEIA [127]

$$\frac{d\vec{r}}{dt} = 0 \tag{3.12}$$

$$\frac{d\vec{p}}{dt} = -\frac{\mu_0}{6\pi c}\frac{q^4 \vec{p}}{mp^2}(\gamma\xi_1 + \gamma^2\xi_2 + \gamma^3\xi_3) \tag{3.13}$$

with

$$\xi_1 = E_T^2 + B_V^2 \frac{p^2}{m^2} \tag{3.14}$$

$$\xi_2 = 2E_U B_V \frac{p}{m} \tag{3.15}$$

$$\xi_3 = E_U^2 + E_V^2 \tag{3.16}$$

where **T**, **U** and **V** span an othronormalized frame in which $\vec{T} \parallel \vec{p}$, $\vec{U} \parallel \vec{p}\times\vec{B}$ and $\vec{V} = \vec{T}\times\vec{U}$. Due to the generally low electric but strong magnetic fields the first two terms dominate the synchrotron losses in KATRIN. This term is expensive to compute and can be switched on if necessary for the simulation.

3.2.1.2. Adiabatic tracking

The electron transport in the KATRIN experiment is designed to be adiabatic to a very high degree, so that electrons energies can be analyzed properly. This property is also used for tracking making use of the adiabatic approximation. It is valid if the particle's trajectory can be split up in two components, one following the magnetic field lines, and one describing cyclotron motions around this field lines (*gyration*. Within KASSIOPEIA, multiple choices about the degree of detail that is modeled in this motion exist.

Furthermore it is possible to take into account $E \times B$ and $\nabla\vec{B} \times \vec{B}$ drift terms that perturb the motion in radial or azimuthal direction. The advantage of the adiabatic method is that it allows for much larger step sizes, jumping over several cyclotron motions of the particle, making the simulation much faster.

The adiabatic method is based on the conservation of the first adiabatic invariant, the orbital magnetic moment of the particle

$$\frac{d}{dt}(\gamma\mu) = 0. \tag{3.17}$$

It is given by

$$\gamma\mu = \frac{p_\perp^2}{2mB_c} \tag{3.18}$$

and proportional to the magnetic flux enclosed by the particle's trajectory, with $p_\perp$ the momentum orthogonal to the direction of the magnetic field and B_c the magnetic field at the guiding center position. An adiabatic motion is only possible if the magnetic field does not change significantly within one cyclotron period. From this we get

$$0 = \frac{d}{dt}(\frac{p_\perp^2}{2mB_c}) \tag{3.19}$$

$$0 = \frac{p_\perp \dot{p}_\perp}{mB_c} - \frac{p_\perp^2}{2mB_c^2}\frac{dB_c}{dt}. \tag{3.20}$$

The time derivative of the magnetic field can be expressed by use of the chain rule

$$\frac{dB_c}{dt} = (\vec{\nabla}B_c\frac{\vec{B_c}}{B_c})\frac{p_\parallel}{\gamma m} = \nabla_\parallel B_c. \tag{3.21}$$

With this we can get $\dot{p}_\perp$

$$\dot{p}_\perp = \frac{p_\perp p_\parallel}{2\gamma m B_c}\nabla_\parallel B_c \tag{3.22}$$

The other first order derivatives of the system then are

$$\dot{\vec{r}}_c = \frac{p_\parallel}{m\gamma}\frac{\vec{B}_c}{B_c} \tag{3.23}$$

$$\dot{\phi} = \frac{qB_c}{m\gamma} \tag{3.24}$$

$$\dot{p}_\parallel = -\frac{p_\perp^2}{2m\gamma B_c}\nabla_\parallel B_c + qE_\parallel \tag{3.25}$$

It is also possible with the adiabatic method to account for synchrotron radiation. This is particularly important for simulations investigating electron transport through the whole KATRIN system because this would take too long and provide only poor statistics with the exact method. In this case, only contributions coming from $\dot{p}_\perp$ are considered. Other influences on the radiated power P can be neglected, taking only the first term in 3.13 into account, yielding

$$P = \frac{\mu_0}{6\pi c}\frac{q^4}{m^4}B_c^2 p_\perp^2. \tag{3.26}$$

As only $p_\perp$ gets affected, we can also write, using $P = dE/dt$:

$$P = \frac{p_\perp \dot{p}_\perp}{m\gamma} \tag{3.27}$$

With 3.27 and 3.26 we can conclude

$$\dot{p}_\perp = \frac{\mu_0}{6\pi c}\frac{q^4}{m^3}B_c^2 p_\perp \gamma. \tag{3.28}$$

This is the term that has to be added to the ODE system to accommodate for synchrotron radiation in the adiabatic approach.

3.2.2. Radon electron spectrum generation

KASSIOPEIA includes a toolkit to generate particles for tracking in a customizable way. Different methods of *time*, *position*, *direction*, and *energy* creation can be freely combined in a PAGE particle generator. Time generator options are: *fix*, *equidistant* and *decay*. With the *decay* option, a random time series with a constant mean rate is generated from an exponential distribution typical for radioactive decays. Particles can be created from a *volume*, *surface*, *disk* or *fix* position, using geometric input from KGeoBag. Starting directions also offer different possibilities, up to self-defined formulas that specify distributions of azimuthal and polar angle.

The options for energy creation include, besides some simple distributions, radioactive decays of radon (isotope 219,220), krypton and of course tritium. The radon electron spectra are quite complicated, and are calculated based on a model developed in [83][141], including a discrete as well as a continuous part.

From the pre-spectrometer measurements, radon was expected as a large source of background in the main spectrometer. We will see that this could be confirmed in the SDS commissioning measurements. Though radon is known as an α-emitter, it also generates frequently electrons in process chains of de-excitation after the genuine α-decay. It happens that either the shell or the nucleus are left in an excited state and de-excitation can happen in complex processes involving an interplay between vacancies and photon emission, leading to electrons emitted in inner-shell shake-off (SO), internal conversion (IC), relaxation (RX) and shell reorganization (SR) processes. The energy spectra, generated from KASSIOPEIA, can be seen in figure 3.1.

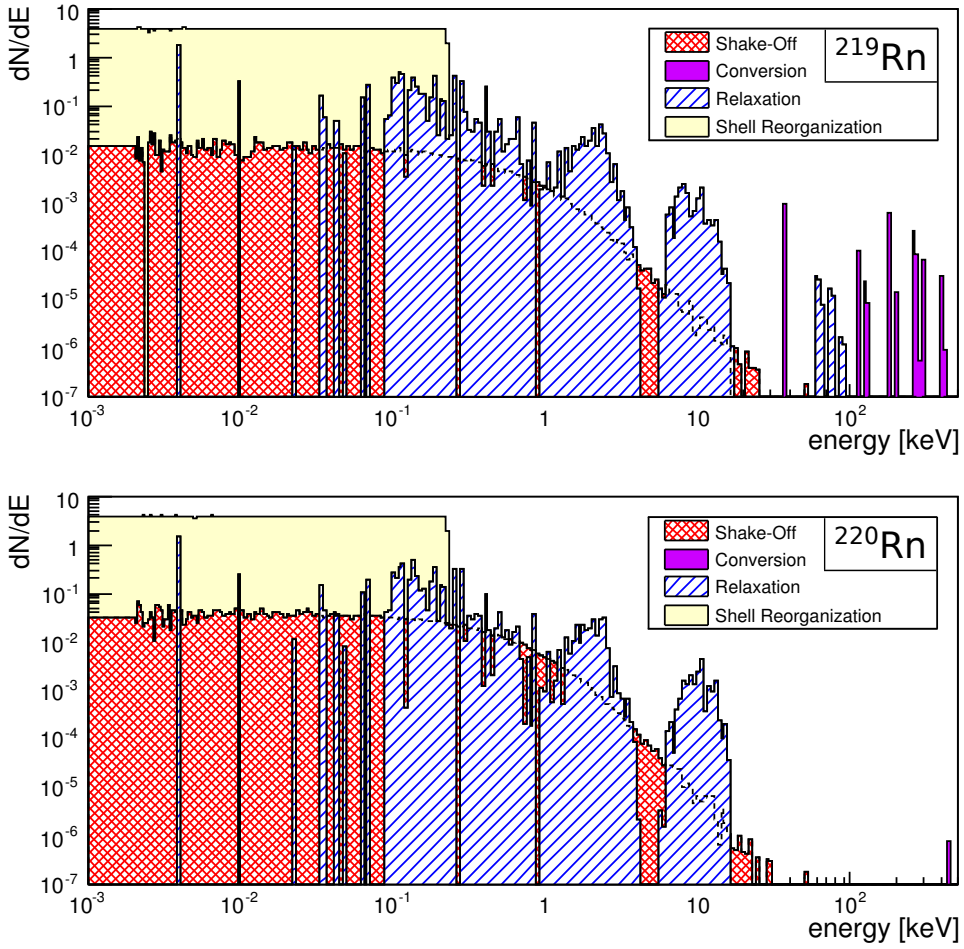

Figure 3.1.: Double logarithmic view of the relative intensity electron energy spectra of the two radon isotopes encountered in the main spectrometer. Contributions are colored according to the processes. ^{219}Rn has a high energy spectrum resulting from the inner conversion processes taking place in $\sim$ 3.5% of the decays and from the following relaxation. ^{220}Rn has only two quite rare conversion lines and thus a much softer relaxation spectrum. The simulations and plots were made after reintegration of the radon generator into the new version of KASPER with a script provided by N.Wandkowsky.

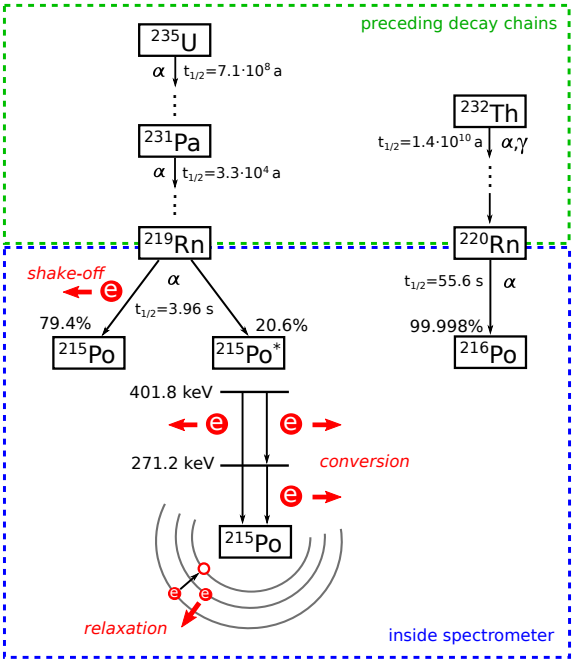

Figure 3.2.: Decay schemes of ^{219}Rn and ^{220}Rn. While ^{219}Rn emanates mostly from the getter material, while natural radioactivity of the vessel material is a source for ^{220}Rn [124]. Image taken from [83]

The decays follow the scheme in 3.2

Internal Conversion is a process in which an excited nucleus transfers its excitation energy to a shell electron that gets kicked out from the atom. This is possible for high-Z nuclei due to the nonzero probability of inner shell electrons to be found at the position of the nucleus. For high Z-nuclei the larger wavefunction overlap ensures the coupling that is needed for the electromagnetic energy transfer and to overcome the probability of radiative processes that would occur otherwise.

Shake-Off can happen due to the interaction of the ejected alpha particle with the inner shell of the atom. The high-energetic helium nucleus can transfer some of its energy to an inner shell electron that then leaves the atom.

Relaxation in general will follow IC and SO processes, as these leave vacancies in the atomic shell in which they happen. The atomic shell quickly relaxes to its ground state through the relaxation processes in which the released energy from electrons that fill the vacancies is transferred to electrons in higher shells, thereby creating new vacancies and so on. Emitted are Auger and Coster-Kronig electrons.

Shell Reorganization is the adaption of the outer shell to the more positive charge state of the daughter nucleus polonium. In contrast to the inner-shell shake-off electrons that closely coupled to the nucleus and hence react fast, the outer shell electrons are much slower and therefore basically decoupled on time scales of the decay process. If the decay does not directly perturb the shell and leaves the nucleus in the ground state, none of the above processes happen and SR is the only source of electrons. When the orbitals reorganize, an energy of $\Delta E \approx 250$ eV is released and shared between the two electrons that have to leave the atom to electrically neutralize it.

3.2.3. Particle Interactions

Within KASSIOPEIA a framework for particle interactions exists. Implemented are e.g. scattering on different gas species (H_2, N_2, H_2O, Ar) and the KESS module for simulation

of electron scattering in the silicon of the detector wafer. Similarly various *terminators* exist that allow to stop a track on user chosen conditions. Since mostly hydrogen is left over as residual gas in an otherwise clean vacuum chamber, scattering processes on this gas species dictate the storage times of electrons in the main spectrometer. The C++ code in charge of scattering in KASSIOPEIA integrates the programs written by F.Glück into the framework. Since electrons with energies as low as 1 eV are trapped in the main spectrometer at nominal settings also the low energetic excitations from rotational and vibrational modes are important which were implemented in [83].

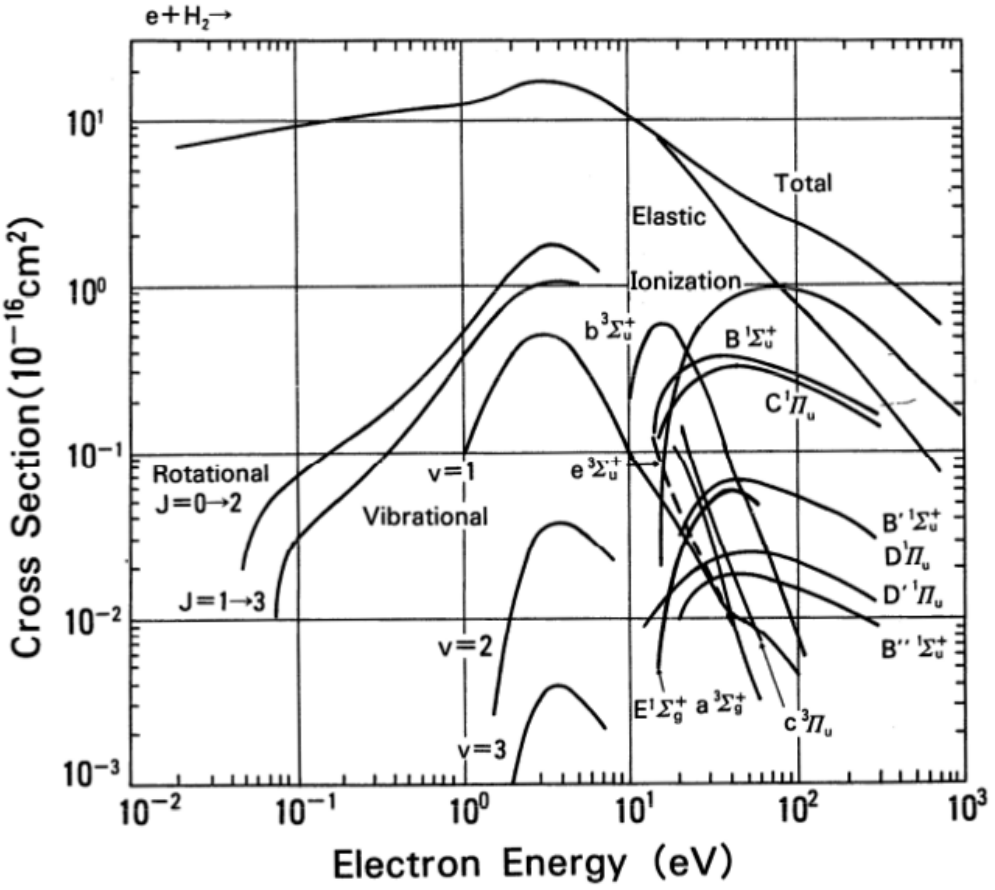

Figure 3.3.: Cross sections for the dominant processes in electron-hydrogen scattering. Figure taken from [142]

Electrons with energies above 1 keV mainly lose their energy via ionization, as indicated in figure 3.3.

3.3. Storage simulations

Because storage simulations with KASSIOPEIA in the main spectrometer, especially at low retarding voltages, turned out to be very computation time consuming, during the course of this thesis an additional program was developed to obtain a significant speed-up. It makes use of the algorithms and structures developed within KASSIOPEIA. The line of attack to this problem was to make drastic simplifications, that are much stronger than the adiabatic approximation, thereby reducing the simulation to the bare essentials, that cover the physics of electron storage , at the cost of predictive power, which is not required in this context. The concept is to neglect all effects, like gyration, magnetron drift and synchrotron radiation that can change the field line the particle is following. We are not interested in the full path the particle has chosen, but only in the time it takes until it

breaks the storage condition, and its production of secondary electrons. Both effects are governed by the scattering off residual gas molecules (mainly hydrogen).

For the purpose of this simulations a field line is chosen by the user. Only on this field line particles are generated and stored, undergoing scattering events until the storage condition breaks, which is tested after each new scattering (and on particle start). Furthermore it is not necessary to continuously compute the particle steps all over again. The idea is to reduce the particles motion to a one dimensional problem and instead of using computing time to compute steps, approximate the traveled distance and time the particle travels until its next scattering. This can be achieved when not dicing for a scattering to occur with a small probability every step the particle takes. Instead a real free path l_f is diced from an exponential distribution governed by the mean free path.

$$p(l_f) = \exp(-\frac{l_f}{\langle l_f \rangle}) \tag{3.29}$$

In this computation there is inevitably an error. The mean free path depends of course on the scattering cross section $l_f = (\sigma n)^{-1}$, which is energy dependent $\sigma = \sigma(E)$. A sensible thing to avoid larger errors then is to take an average over the kinetic energy of the particle along the path and calculate the mean free path with regard to this mean energy.

$$\langle E \rangle = \frac{\sum_{steps} E \Delta s}{\sum_{steps} \Delta s} \tag{3.30}$$

There are other possibilities. For example not to average the energy, but the cross section, this however would cost more computation time and hence was disregarded. Now the path left for the particle till scattering can be computed, which usually is quite long compared the path length of the particles trajectory between the two reflection points. Most of the propagation can be skipped by subtracting N times the round trip length l_2 from the free path where $N = floor(l_f/l_2)$. The rest of the path is stepped through on the pre-computed points of the field line until the remaining path is zero or less. At this point the scattering process can be invoked and the whole procedure repeated. In case of ionization, particles are produced the same way as in KASSIOPEIA and appended for processing.

At the start the main input from the particle are the polar angle θ, its position and its energy. With this we calculate using the adiabatic approximation from point to point the new angle, longitudinal and total kinetic energy, cyclotron path length and flight time. For the longitudinal energy we use the functions integrated in the C++ FieldLine class from KTrAP. The angle is from there recovered as

$$\tan^2(\theta) = \frac{E_\parallel}{E_\perp} \tag{3.31}$$

The path length of the particles trajectory is important for its scattering probability. Scattering naturally occurs more often where the particle makes a longer path. Obviously the path electrons follow is much longer than the field line they are following. To account for this the length of the real path is approximated step wise as a simple helix.

$$\Delta l_{cyc} = \Delta l_{fl} \cdot \sqrt{1 + \frac{1}{\tan^2(\theta)}} \tag{3.32}$$

To make sure that our model is not completely off from the exact tracking we can compare, for example, the spacial distribution of the ionisation probability. Further results that confirm these simulations are displayed in the next chapter.

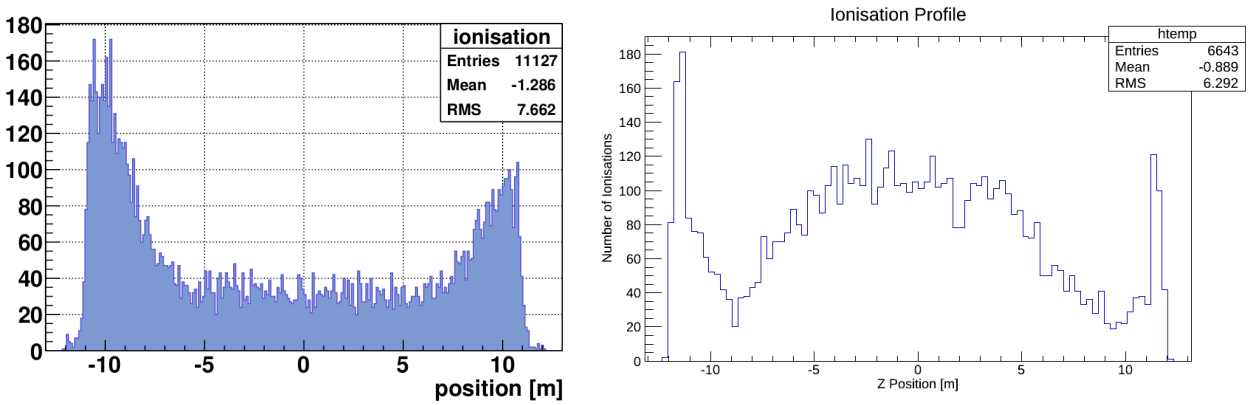

Figure 3.4.: ionization profile of the main spectrometer along the z-axis. Left: Old simulation from [143]. Right: New storage simulation with a comparable setting. However, the details of these simulations differ, so identical results are not expected. The bulge in the middle of the spectrometer in the new simulation reflects that more initial particles were created there as well.

4. Investigation of stored particles

The main goal of this thesis was to investigate the main spectrometer background from stored particles (mainly induced by Radon decays) in the SDS comissioning measurements. First previous results will be recalled briefly in 4.1. Then the outcomes of selected measurements will be presented in 4.2 but not commented. One thing to state in advance is that the background at the main spectrometer is not fully understood. To have a chance in sorting the situation out, all information available has to be taken into account. Thus measurements performed by others will also be cited here. Afterwards a discussion and an approach of interpretation with the help of simulations follows in 4.3.

4.1. Previous results

In previous efforts the expected activities for ^{220}Rn and ^{219}Rn and resulting background rates have been computed for different scenarios [99], with varying amounts of getter material and with or without cryogenic baffle, after measurements at the pre-spectrometer [125][144][141] revealed that nuclear decays of radon will significantly contribute to the main spectrometer background. A radon model has been developed, validated [145][124] and is being used in the following. The radon activities for the situation encountered in the current SDS comissioning measurements, warm baffles, no emanation from pre-spectrometer getters, have not explicitly been estimated but are very similar to scenario 2 described in [99]. Since in the main spectrometer 3000 m of getter material are used and 250 m in the pre-spectrometer (when it is installed, which is presently not the case), it is a conservative approach to work with the slightly higher estimate of 118.5 ± 29.5 mBq as ^{219}Rn activity sourced by the getter material. The radon activities sourced by emanation from the walls have been estimated as 27.2 ± 27.2 mBq for ^{219}Rn and 67.8 $\pm$ 45.0 mBq for ^{Rn220}Rn. From this total amount of radon decays a background rate of ~ 1 cps is then predicted.

4.2. SDS comissioning measurements of the KATRIN main spectrometer

Over the course of this thesis the author participated in several of the SDS commissioning measurements that took place from the end of May to mid of September 2013 after the KATRIN main spectrometer has been successfully baked out and spectrometer and detector were connected to share one vacuum. In the following the outcome of especially these, as

well as several measurements performed by others, will be reported on to describe carefully the status of the main spectrometer background.

After the connection of the main spectrometer to the detector the first light measurement took place [146]. It confirmed that with the spectrometer at ground potential there was no unexpected background that could be harmful to the detector. Multiple measures were taken to ensure hardware safety in any case. Before opening the valve to the spectrometer the Pulcinella disk was lowered to cover the detector, acting as a shield. The titanium disk can act as a calibration source for the detector when illuminated with UV light. Therefore it is connected to an integrating normalization electrometer with which ultra low currents in the pA range can be measured. As these measurements showed no raise in current after the opening of the valve the spectrometer at ground potential was considered safe.

4.2.1. Low IE voltage dependence of main spectrometer background

What followed were the first ramp ups of the inner electrode potential with the vessel still being at ground potential. As a safety measure the inner electrode potential was limited to 1 kV in order to avoid possible discharges that could harm either the detector or the inner electrode. Additionally two automatic safety programs are in charge. One watches the currents in the inner electrode and shuts the voltage down if a current of 5 μA is exceeded. The other one forbids further increasing of the voltage if a rate of 10 kHz is measured at the detector. Additionally at a measured rate of 100 kHz the gate valve between spectrometer and detector is automatically closed and the voltage ramped down. However none of these cases happened indicating that no major penning trap is present in the spectrometer at these settings. What was observed was a rate that increased exponentially with the voltage as seen in figures 4.1, 4.2 and 4.3.

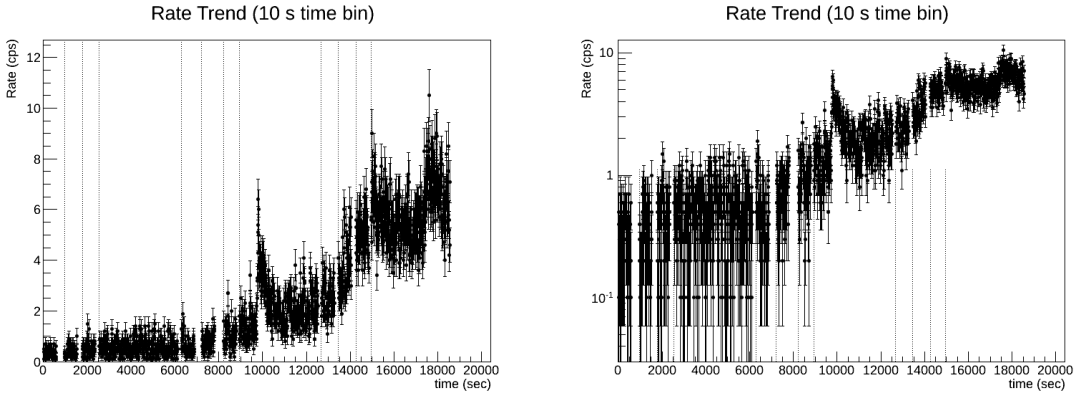

Figure 4.1.: Background measurement at low retarding potential ranging from 50 to 600 V in steps of 50 V. At 200,400 and 600 V the rate was measured for 3600 s. For the other voltages data was taken for 600 s . The same potential was applied to all IE modules and the aircoils and solenoids were in a symmetrical 380 μT setting [147]. With growing potential the Background increases and the fluctuations get stronger. Even a strong exponential decaying peak is visible from $t \approx 10000$ s. The data corresponds to the runs 4906-4929 as found in [148]. A ROI of 7-12 kV was selected, adjusted to the post acceleration potential of +10 kV that is necessary to accelerate electrons from the spectrometer to detectable energies.

The background rate empirically amounts to $R_{bg} = R_0 \exp(\frac{U}{U_0})$ with $R_0 = 0.16 \pm 0.05$ cps and $U_0 = 181 \pm 13.34$cps, the fit can be seen in 4.3. After these initial measurements it was unclear if this trend would continue for higher voltages with the spectrometer vessel

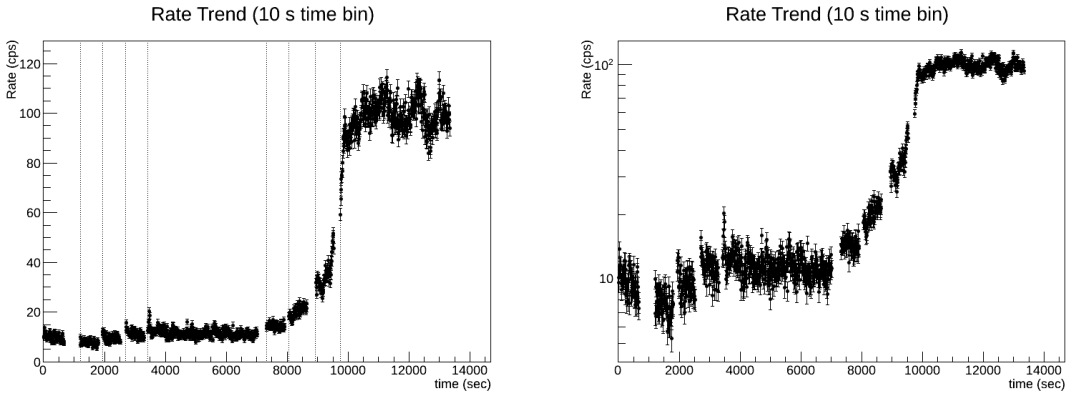

Figure 4.2.: Second measurement ranging from 600V to 1000V in steps of 50 V. 3600 s Measurements are taken at 800 and 1000 V, the other measurements lasted 600 s. The settings are the same as for the measurements with lower voltages. Data corresponds to runs 4955-4963 in [148].

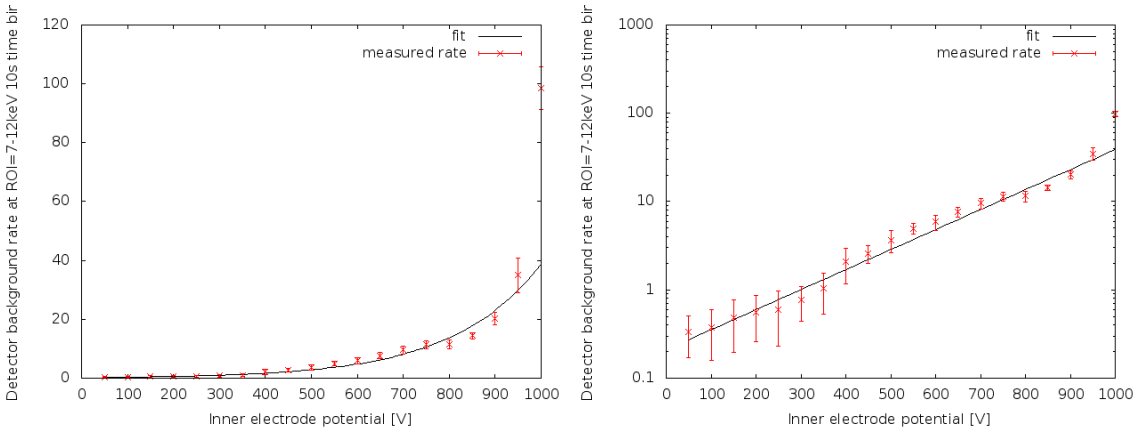

Figure 4.3.: Exponential fit of the extracted rates. The last data point at 1000 V, being far off, was excluded from the fit. An exponential trend is visible. The large errors are due to the relatively short measuring times. To decide if the deviations from the trend, especially the high rate at 1000 V, are by coincidence or not longer measurements would be necessary.

also at potential, posing a severe problem. However this turned out not to be the case, as seen later.

4.2.2. Rate fluctuations at low retarding potential

The background encountered in the presented measurements exhibits strong fluctuations. As in the case of the 200 V measurement these fluctuations can grow as large as $\sim 50\%$ of the rate. This can be seen well in long term measurements that were taken at weekends or overnight.

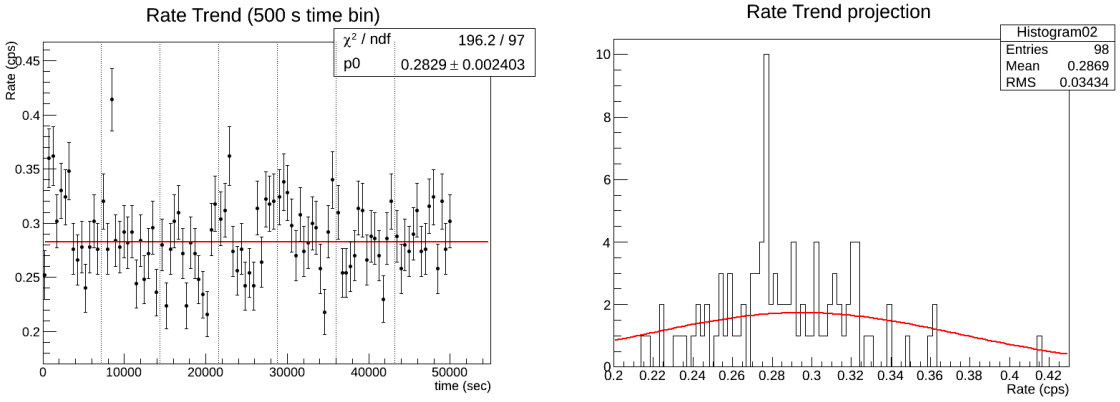

Figure 4.4.: Fluctuations at zero electric potential and 3.8 G magnetic field in the analyzing plane. Errors obtained from fitting a constant to the rate are much to low. On the right side we can see that the distribution is quite broad. Runs 4964-4969 as in [148]

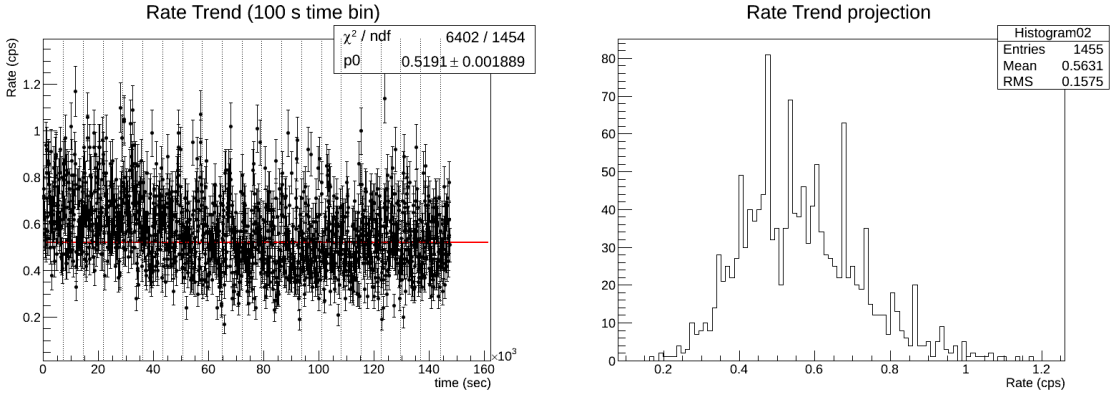

Figure 4.5.: Fluctuations at an inner electrode potential of 200V and 3.8 G magnetic field in the analyzing plane. The measurement spans a weekend, about $140 \cdot 10^3$ s and consists of the runs 4931-4951 [148]

4.2.3. Radial distribution of the background at low retarding potential

The rate distribution over the detector is almost centered. At the moment there is a shadow on the flapper valve, which does not open completely and the system is not yet perfectly aligned [149][150]. At low retarding potentials the rate decreases with increasing radius. Due to the misalignment, field lines starting at the outer ring of the detector are hitting the geometry and thus display an elevated rate. Hence, the outer ring is in general cut from the data.

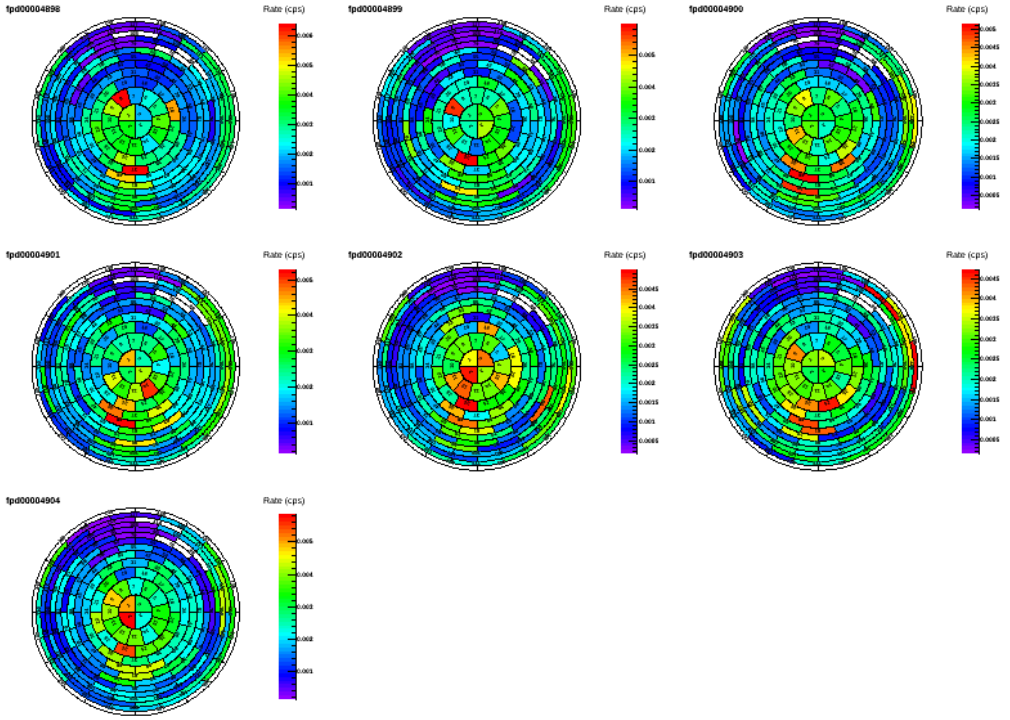

Figure 4.6.: FPD pixel distribution at an zero potential background measurement [148]

The volume that is magneto-optically "seen" by each pixel on the detector crucially depends on the precise magnetic field setting. During the SDS commissioning measurements three such transmission-optimized [151] standard settings are being used, with a magnetic flux density of 380,500 and 900 μT in the analysing plane. For these settings the volume that is imaged onto the the different pixel rings of the detector has been calculated [152]. The volume-normalized rate per ring is found to decrease exponentially with the ring number as can be seen in 4.7.

4.2.4. Passive background reduction by cryogenic baffles at low retarding potential

Radon emanating from the getter pumps was expected as a major source of stored electrons, and therefore background, since the measurements at the pre-spectrometer. As a countermeasure liquid nitrogen cooled baffles were first installed and successfully tested at the pre-spectrometer [123] to prevent emanated Radon from reaching the sensitive volume of the spectrometer. Apart from blocking the line of sight to the spectrometer from the getter stripes the Radon also freezes to surface of the cooled baffles. This cryo-pumping effect also reduces the Radon emanating from the walls of the spectrometer. After this proof-of-concept baffles were also installed at the main spectrometer and have been tested by S.Görhardt [154][155]. These are crucial measurements to estimate the background from stored electrons caused by radon decays. Hence we will recall this important results by S.Görhardt here briefly. A full analysis of these will be found in [156].

Measurements were taken at different magnetic and electric field settings, both with up to three cooled baffles at $\sim$ 160 °K and at room temperature. With the 380 μT magnetic field setting rates were measured at retarding potentials of -30, -300 and -600 V. At -600 V an additional measurement with 900 μT was done. Here the focus is on the first three, since they are best comparable to the other background measurements.

The most important observation to note here is that the background reduction efficiency

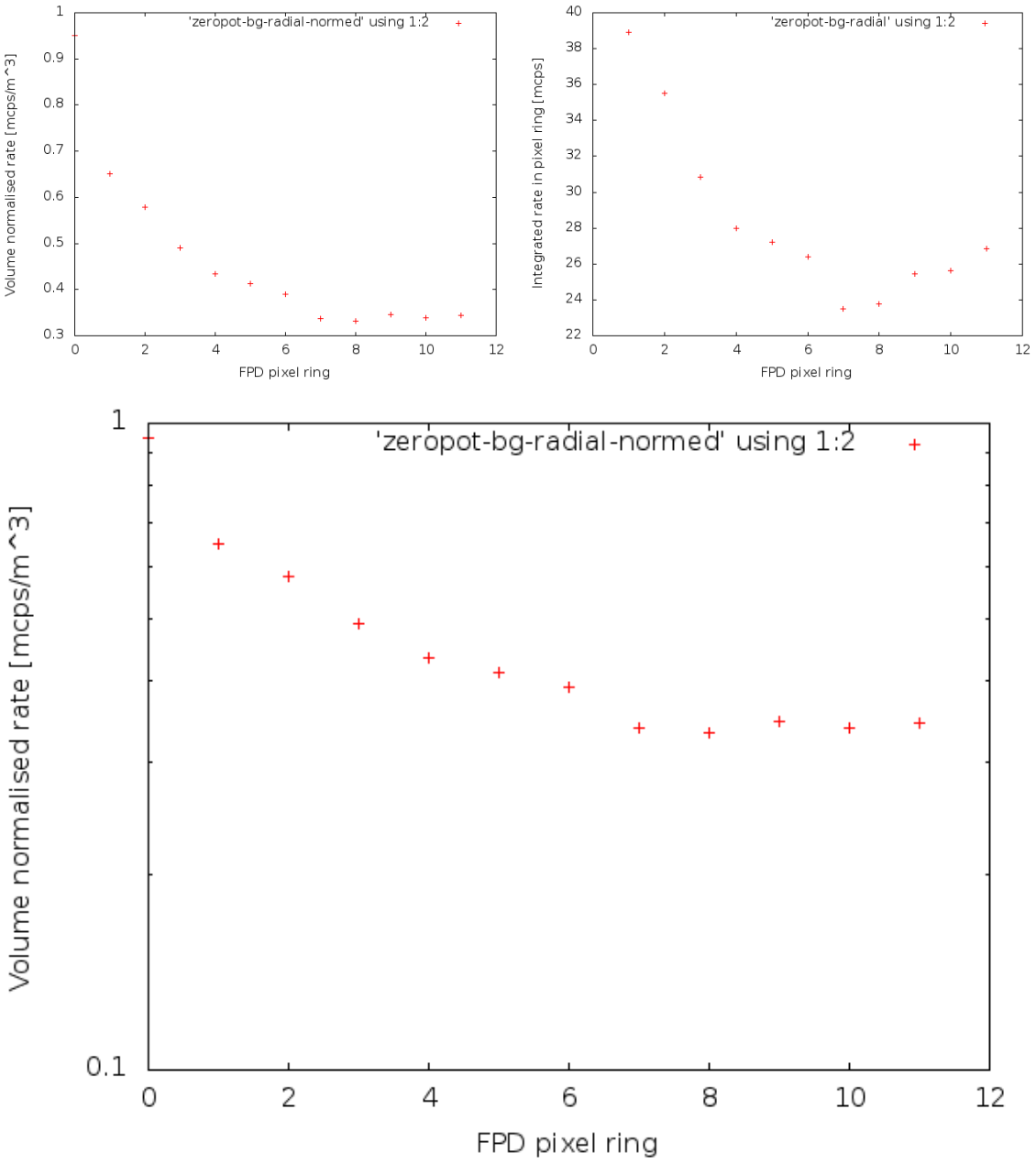

Figure 4.7.: Radial distribution of zero potential background by pixel ring. In the upper left and the lower plot the rate has been normalized to the volume imaged to each ring by the magnetic field. From the center outwards the rate drops exponentially - neglecting the slightly different pixel ring widths - as is visible from the logarithmic plot. Data from runs 4898-4904 as described in [153]. From ring 7 outwards the rate rises again.

	Inner electrode potential[V]		
# of cooled Baffles	-30	-300	-600
0	0.1621 ± 0.0024	20.16 ± 0.06	16.16 ± 0.03
1	0.1004 ± 0.0019		7.40 ± 0.02
2	0.0793 ± 0.0017		4.38 ± 0.02
3	0.0624 ± 0.0015	4.23 ± 0.02	2.99 ± 0.01

Table 4.1.: Background rates measured with warm and cooled baffles according to [154]. The measurement time was 2-10 h per point, depending on the rate.

increases with higher inner electrode potential as can be seen in tables 4.1 and 4.2. Another

Inner electrode potential [V]	Background reduction factor
-30	2.59 ± 0.10
-300	4.76 ± 0.04
-600	5.40 ± 0.03

Table 4.2.: Background reduction factors obtained from the baffle measurements with 3 cooled baffles

remarkable aspect is that the radial rate distribution changes drastically when the baffles are cold. The initially exponential decreasing rate with higher radii changes into a radially increasing.

4.2.5. Background at high voltage and reduction by cryo baffles

During the writing of this thesis the main spectrometer vessel was put on potential for the first time. At the first detector-monitored ramp to 18.6 kV, on the same potential as the inner electrode, the exponential rise of the background rate did not occur. Instead, looking at a wide ROI of 7-32 keV the rate stays around 1 cps. Though this figure is two orders of magnitude larger than the targeted design rate of $10 \cdot 10^{-3}$ cps this marks a big success. At the pre-spectrometer as well as at the Mainz experiment the rates observed in the first commissioning reportedly were much higher.

With the vessel on high voltage the background does not increase drastically when applying a moderate offset voltage on the inner electrode [158]. A 24h measurement in a 380 μT magnetic field setting, a hull potential of -18500 V and an inner electrode offset of -100 V yields a background rate of (777 ± 6)mcps [159].

Also at high voltage baffle tests were performed by S. Görhardt[155].

4.2.6. Ion Peak and field emission

The last piece of information to be displayed here is probably the most puzzling so far. In the detector energy spectra taken in high voltage measurements a sub dominant ion peak has been discovered [159]. The rate in this peak and the rate in the electron peak at an energy of $(U_{PAE} + U_{ret})e$ show a strong correlation. The strength of this peak rises with the offset voltage between IE and vessel. Due to the peak position it has been attributed to negative hydrogen ions. Further measurements investigating this revealed that the rate in the electron peak depends strongly on the applied potential difference between wire electrode and vessel - like in the low voltage settings measurements. Here however the increase is found to be compatible with the electrons being caused by field emission as J.Schwarz pointed out using the Fowler-Nordheim theorem [158]. The source of the ions themselves and their correlation with the electron rate remain so far unexplained.

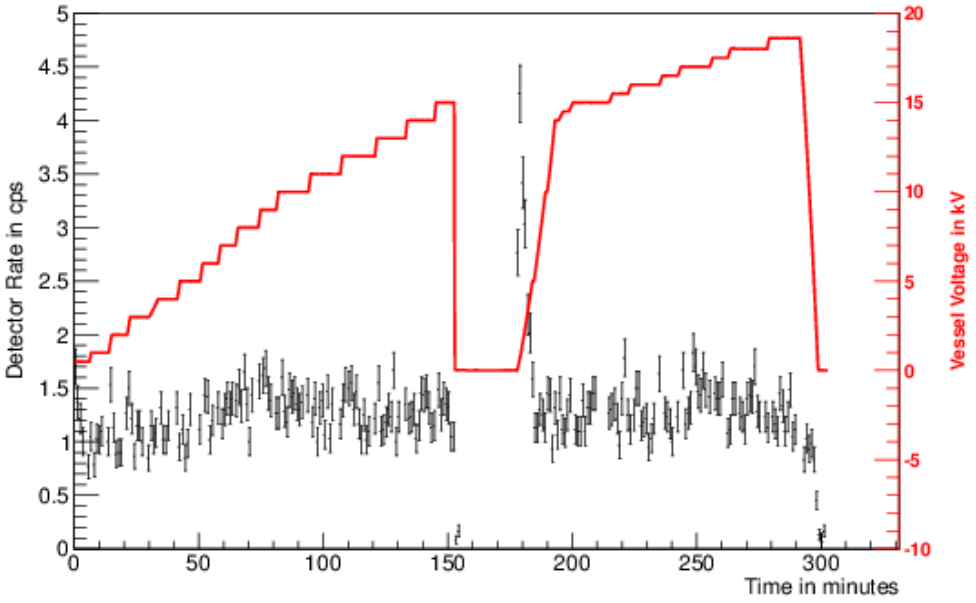

Figure 4.8.: The rate stays the same during ramp up. After a safety shut down of the high voltage due to too strict parameter monitoring a release of particles can be seen in the second ramp up. Figure from the Elog [157].

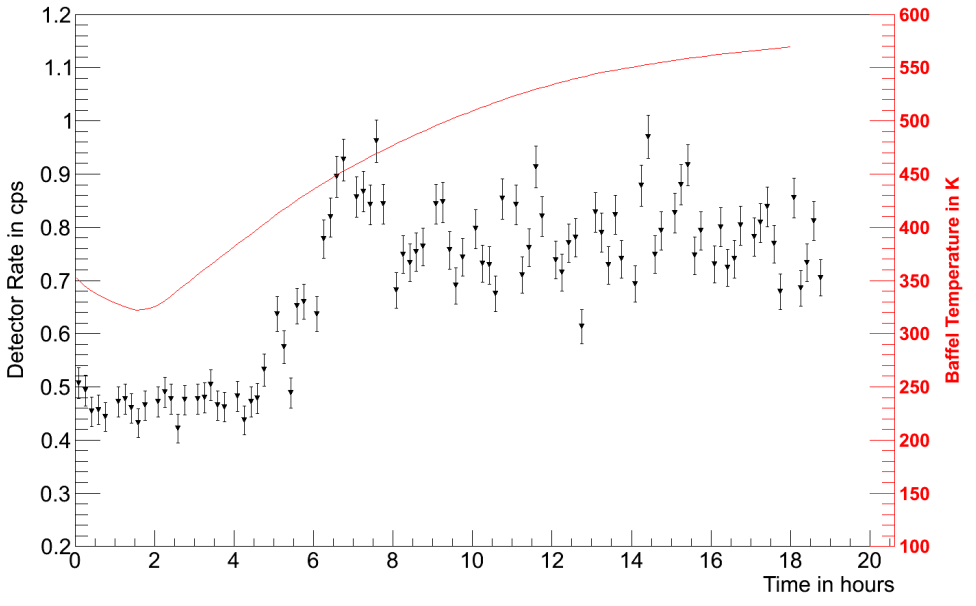

Figure 4.9.: Defrosting process of the baffles. The background rate rises from (484±6)mcps to (777 ± 6)mcps. With cooled baffles, the left over background is much more quiet, exhibiting smaller fluctuations. Measurement and image from [155]

4.3. An approach to understanding the main spectrometer background

It is evident that the current background situation is rather complex. Multiple known, and possibly unknown sources of electron background from the main spectrometer add up and the available time in the commissioning schedule is spare, since important transmission measurements have to be performed as well. In the following it will be tried to distinguish between the different backgrounds. From storage simulations of Radon-caused electrons a new insight into background generation will be gained. A full featured background model is not yet at hand and important questions have to be left open and further measurements will be necessary to answer them.

4.3.1. Storage simulations and an avalanche hypothesis

A known source of background are electrons emitted in nuclear decays of radon. These electrons are stored in the magnetic bottle a MAC-E-Filter type spectrometer represents. The property that defines the resolution of the spectrometer - the ratio of minimal and maximal magnetic field - also determines the 'tightness' of the magnetic bottle, the storage time distribution. The excellent energy resolution of the spectrometer implies long storage times. This essentially is the largest problem for storage time simulations with electron tracking, especially at low retarding potentials. Since $\Delta E = U_{ret} B_{\min}/B_{\max}$ storage times grow to huge values of 10^6 s when no voltage at all is applied. With the new trackless storage simulation presented in 3.3 quick and flexible simulations become possible. One, maybe surprising, result is that the secondary electron production from stored electrons rises exponentially. For this simulation random decays of ^{220}Rn were generated with equally distributed Z-position along a magnetic field line hitting the detector at a radius of 1 cm (within pixel ring 1). A pressure of 10^{-10} mbar was assumed. The inner electrode potential (the same for each module) was varied from 200 V to 1000 V in 50 V steps, keeping the vessel at ground potential. The magnetic field setting however was an older 150 μT standard setting not reflecting the situation in the SDS measurements.

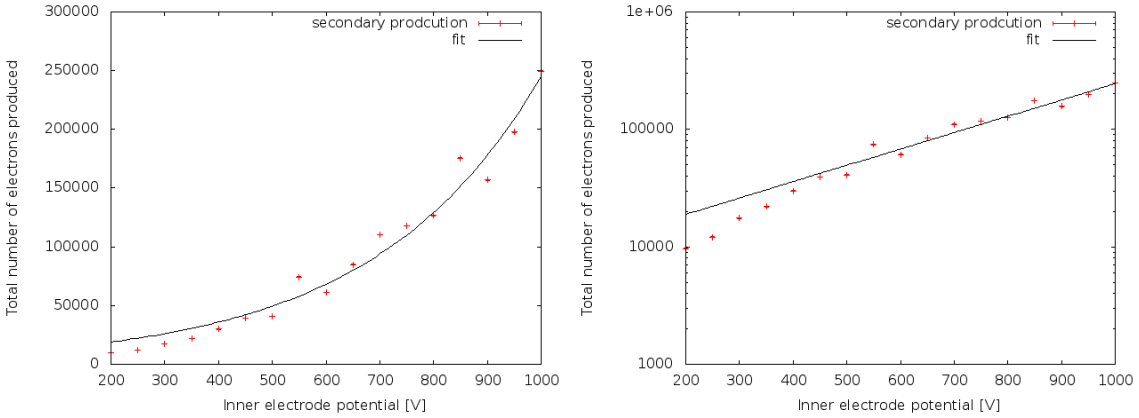

Figure 4.10.: Simulation shows exponential rise of the secondary electron production with the inner electrode potential. The vessel has been kept on ground potential. For each point 100 radon decays were simulated. The strong increasing electron production also poses a big problem for usual particle tracking simulations.

As can be seen in figure 4.10 the electron production rises exponentially with the inner electrode potential: $N_{\text{sec}} = N_0 \exp(\frac{U_{\text{ret}}}{U_0})$. A fit yields $U_0 = (312.478 \pm 17.87)$ V and $N_0 = 9986 \pm 1610$. Though this rise is much steeper than the rise of the observed *rate*

with $U_{0,R} = 181 \pm 13.34$ V it is arguable that the discrepancy in fact is not so severe. It should be reminded that the simulation completely neglects non-adiabatic effects, drift velocities, magnetic inhomogeneities etc. all of which effect the storage properties of the spectrometer.

In the following an avalanche mechanism is proposed to physically explain the observed potential dependency of the background rate. Furthermore it is argued that this effect is observed in the measured data and possible alternative explanations are discussed, especially the field emission hypothesis.

A possibly simple explanation for the exponential increase is that avalanches of secondary electrons form in the potential created by the inner electrodes. With the voltage on the inner electrodes increasing, the potential hill gets higher and higher. Now electrons that encounter hybrid storage conditions - meaning they magnetically reflected at the pinch magnet and have to low kinetic energy to cross the potential wall to the pre-spectrometer side - can use energy drawn from the electric potential to ionize residual gas atoms. In return their storage region is shrinked to regions of lower potential energy. Since the electrons caused by ionization can undergo the same process, a whole avalanche of electrons is started. The strength of this avalanche will be determined by the height of the potential wall created by the inner electrodes.

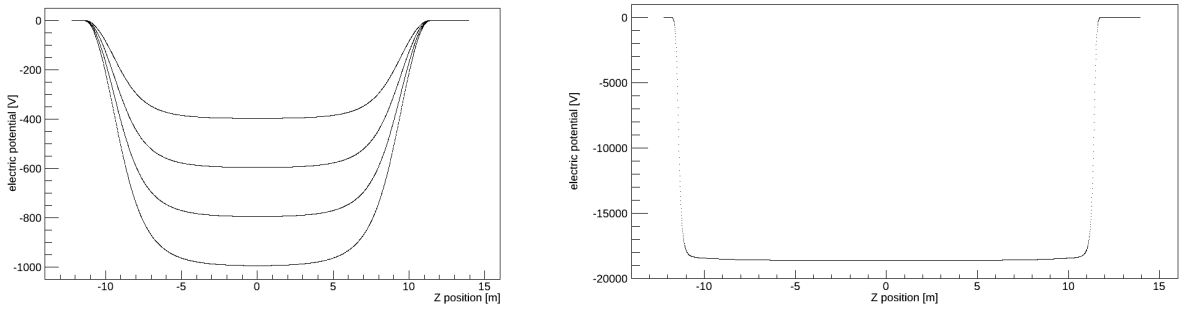

Figure 4.11.: At low retarding potentials, the vessel put to ground potential (left) the potential wall is not very steep. The resulting electric fields range in this example from 100 to 300 $\frac{\mathrm{V}}{\mathrm{m}}$. The potential values have been traced on the central field line from pinch magnet to the pre-spectrometer magnet. In comparison the potential at 18.6 kV retarding voltage (right). The potential is very steep, this is the desired effect of the anti-penning electrode.

In the simulations this hypothesis is supported by the observation that the majority of electrons are not ionized in scatterings involving the electrons emitted from the radon, but by other ionization electrons.

This leads to non-trivial storage time distributions. At low retarding voltages this distribution shows two peaks, a dominant and a sub dominant one at larger storage times.

At this place it should be remarked that this mechanism, if it is present in the spectrometer, would effect *all* stored electrons in the spectrometer, not only those related to radon.

4.3.2. Discussion and tests of the model

Two arguments could be brought up against the previously presented hypothesis.

- The background rate with the main spectrometer at high voltage is much lower than in the low retarding potential settings. Can an exponential increase at low voltages and a relatively low background at high voltage be simultaneously explained with the approximations made in the simulations?

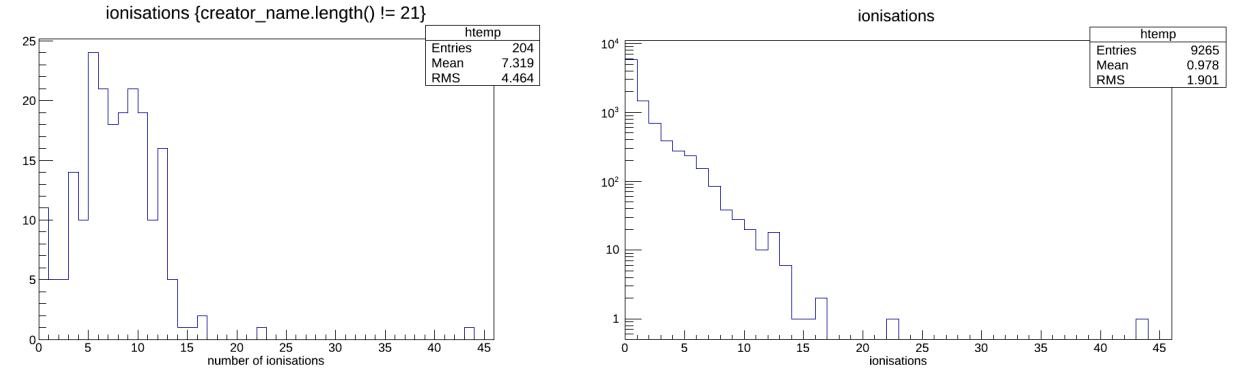

Figure 4.12.: Simulation example from the 200 V setting. Left: ionizations by only primary electrons. Right: Ionisations by all electrons. One primary electron statistically causes 7.3 secondary electrons, but this amounts to only about 16% of the total secondary production. The mean probability, taken over all electrons, to produce a secondary electron is close below one. In the simulation the spectrometer is close to criticality and thus highly sensitive to disturbances at low retarding potentials.

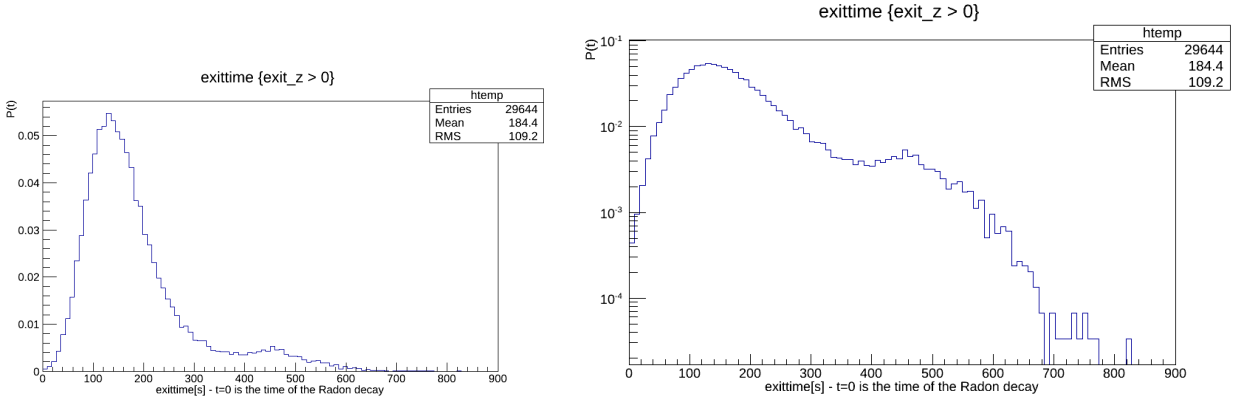

Figure 4.13.: Distribution of arrival times at the pinch magnet just before reaching the detector. Measured from the time point of the radon decay. Simulation run with 600 V potential on the inner electrode, vessel at ground potential. A growing avalanche forms and causes a second peak 'echoing' in the spectrometer. The mean exit time from the spectrometer after a nuclear decay amounts here to 184 s.

- As field emission seemingly is an observed effect and the electron rate has a strong correlation with the measured ion rate, the exponential increase with growing potential difference should be attributed to the field emission and the ion creating processes in both, HV and LV settings and is not caused by stored electrons.

Both points can be resolved, the first one is simple: Due to the locally high electric field in the high voltage setting avalanches can not form. The electrons undergo high accelerations to energies of 18.6 keV where the cross section for scattering is substantially lower, see figure 3.3 and figure 4.11 for the potentials. In addition the storage times in high voltage settings are significantly shorter also preventing such an effect. In fact the simulation predicts lower background rates in high voltage settings than in low voltage settings.

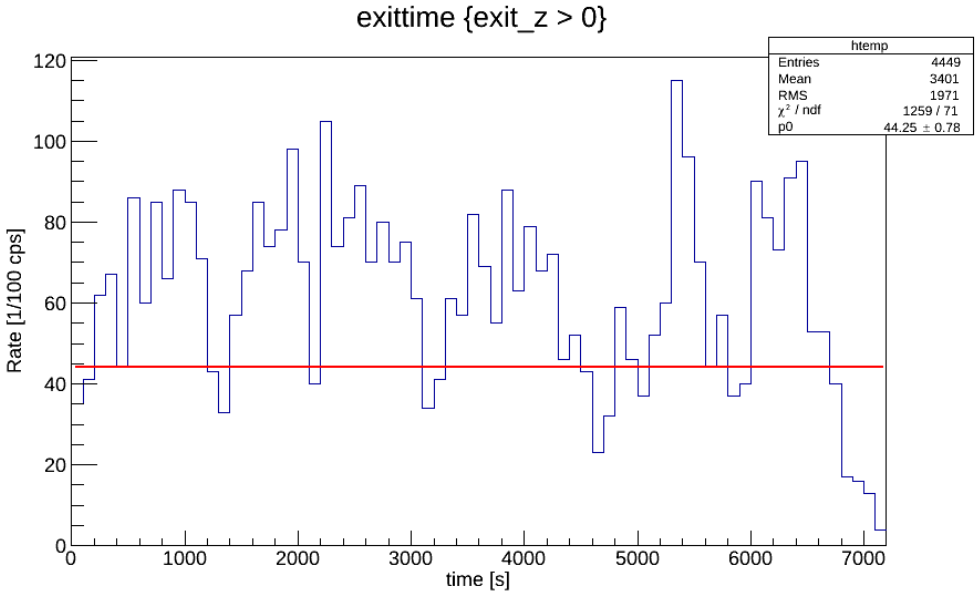

Figure 4.14.: The rate at high voltage settings is not as high as at low retarding potentials on the inner electrode. For this simulation a time series of ^{219}Rn decays was generated assuming an activity of 0.145 Bq - the ^{219}Rn activity calculated in [99]. As field settings a magnetic field of 380 μT in the analyzing plane, a potential of 18.6 kV on the inner electrode and a vessel potential of 18.4 kV were used. The simulated pressure was 10^{-10} mbar. An average rate of 0.442 ± 0.08 cps is created. This result is comparable to recent measurements in the main spectrometer [155], considering that also other background sources contribute

The second point is more difficult. In fact for field emission according to the Fowler Nordheim theory [160] the emitted current density is expected to behave like

$$j(E) \sim E^2 \exp(-\frac{E_0}{E}). \tag{4.1}$$

This was observed in the high voltage settings. But when using the same plot for the measurement at low retarding voltages this fails as visible in figure 4.15.

Furthermore the increase in rate due to an offset between inner electrode and vessel is much less prominent when the vessel is on high voltage, as seen in [158], compared to the strong increase at low retarding potentials.

The strongest argument for the presence of an avalanche mechanism at low retarding potentials are the baffle measurements in these settings. They show that with an increasing

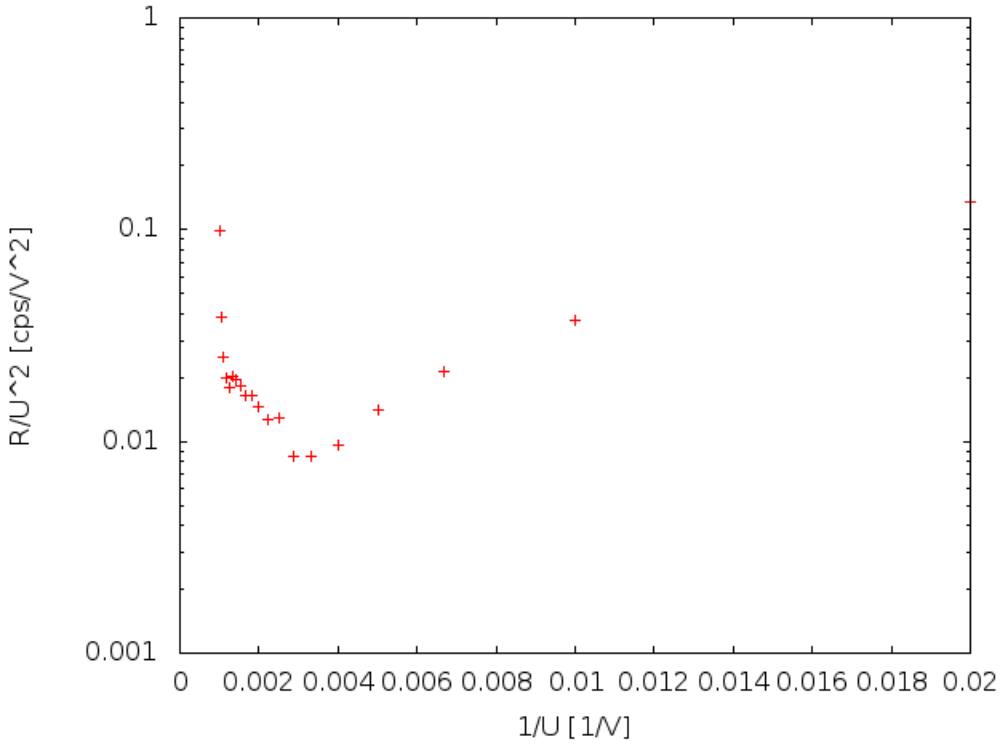

Figure 4.15.: Fowler-Nordheim plot of the low retarding potential measurements in [148]e. This does not match the results in [158] indicating that the spectrometer background at low retarding voltages is not dominated by field emission

rate due to larger retarding potentials also the background reduction by the baffles grows. There is no apparent reason why the cooled baffles should affect field emission at the inner electrodes (which stay at room temperature). The most probable explanation is that at least the removed background originates from radon decays. Another hint is given by the radial distribution of the background rate. Here the performed simulations actually fail to predict the correct profile.

Nevertheless what is observed is that the radial rate density distribution changes drastically when the baffles are cooled. The exponential radial rate density profile observed only with warm baffles should consequently be attributed to stored particles. It should be remarked that this clear profile is only obtained if the rates are scaled by the volume imaged onto the pixel rings of the detector. This is a strong indication that the dominant background stems from an effect proportional to the volume, e.g. stored particles - this explicitly applies also for the high voltage measurements. In addition it is also possible that electrons emitted by field emission could be stored. Admittedly this is unlikely due to the very low kinetic starting energy such electrons have. Field emission electrons undergo a tunneling process from within the electrode meaning they would not be able to escape classically - due to their low energy.

Summing things up, it can be stated that

- The developed simulation predicts an exponential dependence of the background rate on the IE potential as found in measurements with the vessel at ground potential.
- The slope of this exponential rise is overestimated
- In these settings the rate-potential dependency is not explained by Nordheim-Fowler theory.

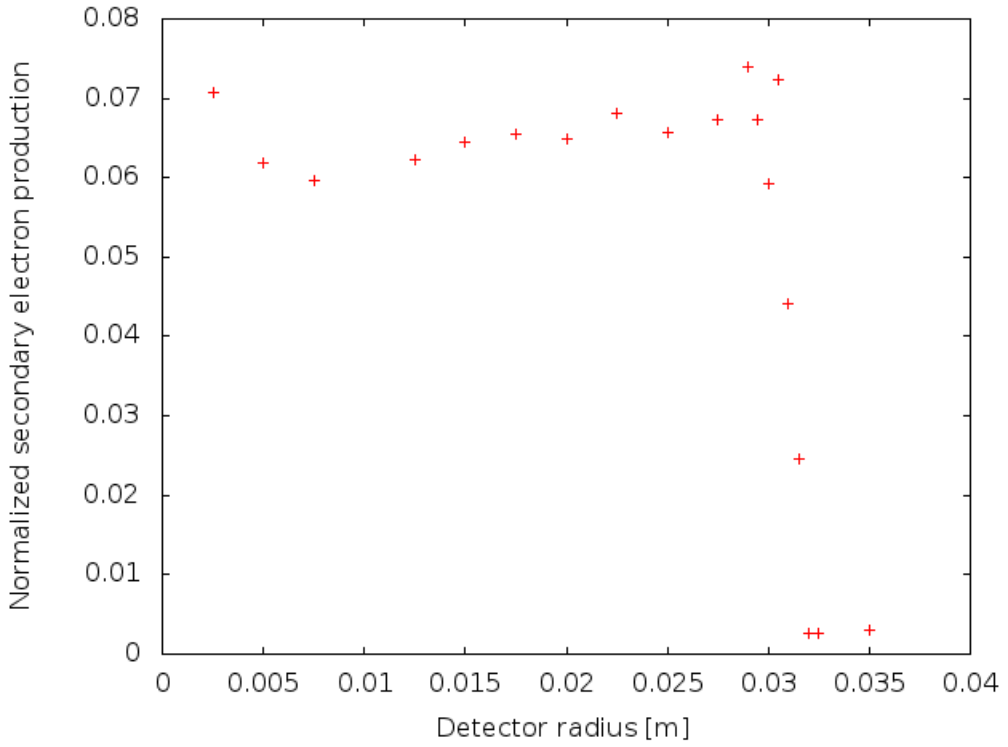

Figure 4.16.: In contrast to the measurements as shown in figure 4.7 the storage simulation predicts two regions of rather constant rate on the detector wafer: one inner region showing a high rate and an outer region with a significantly lower rate. Between those regions a sharp border manifests. In measurements a smooth decrease towards the outer rings is observed. This result stems from simulations performed with 600 V on the IE, the vessel put to ground potential. For each point the storage and secondary production of electrons from 1000 ^{219}Rn decays was simulated along a magnetic field line ending at the corresponding radius on the detector wafer

- The developed simulation tool yields for high voltage settings rates comparable to the actually measured rates under the assumption of a radon activity of the size expected from [99].
- While the overall electron production can be estimated, the radial profile is mismatched.
- The background stemming from field emission is stronger on the outer radii, something that can be expected.
- A so far unexplained process generates ions in the main spectrometer. The same process has an influence on the observed electron rate.

4.3.3. Estimation of the radon activity in the main spectrometer

In the current situation at the main spectrometer a precise determination of the background due to radon decays is hardly possible. With an unknown background component mixed in only a rough estimate can be obtained. This will be tried. Using the *decay* time generator implemented in KASSIOPEIA time series of nuclear decays can be simulated. If these are used as input for the presented storage simulations a realistic signal can be generated in which both, the efficiency of the secondary production and the storage time distribution of the spectrometer in the simulated setting are taken into account. However the high-energy electrons from ^{219}Rn can not be processed with the developed tool. A hybrid approach to this is a goal for the future. Here however we can see that if the activity estimates from [99] are used, the low energetic part of the energy spectrum (which is the same for ^{219}Rn and ^{220}Rn) already creates rates comparable to the measured (777 ± 6)mcps [159]. This indicates that the radon activity is lower than previously estimated. With respect to the baffle measurements this could either mean that it is less than half as much - according to the drop of ~ 300 cps observed there - or that the baffle efficiency is bad. However since there is also the field emission and ion background no stringent result can be obtained at the moment.

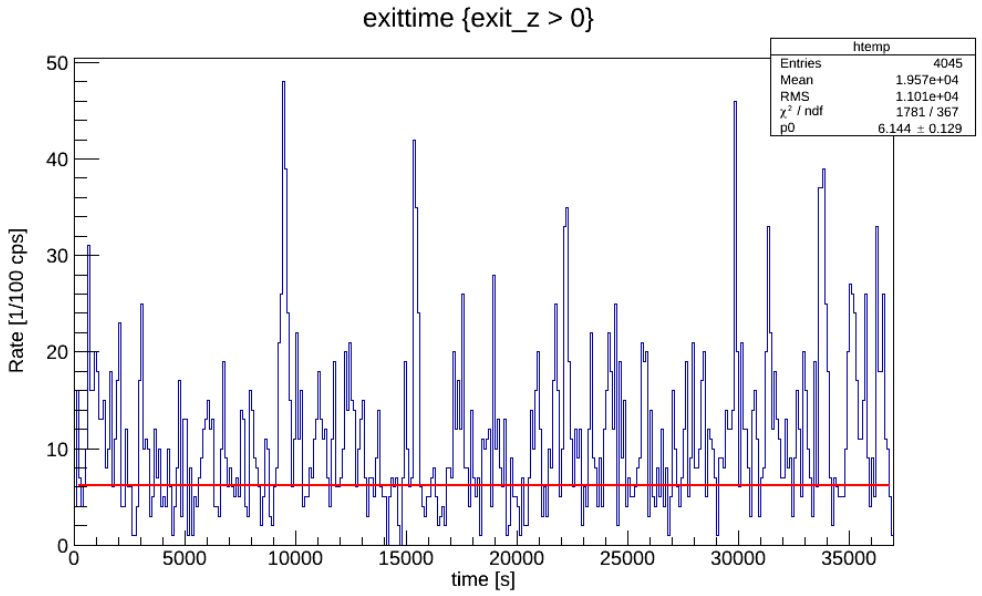

Figure 4.17.: Simulated background signal from a 27 mBq rate of ^{220}Rn at 18.6 kV inner electrode potential an 18.4 kV vessel potential at the standard 380 μT setting. The constant fit rate $R_{\text{fit}} = 0.061 \pm 0.001$ cps is significantly lower than the rate obtained by a long-term time integration $R_{\text{long}} 0.109 \pm 0.001$ cps - which gives the spikes a higher weight. This needs to be considered when comparing simulated and measured rates.

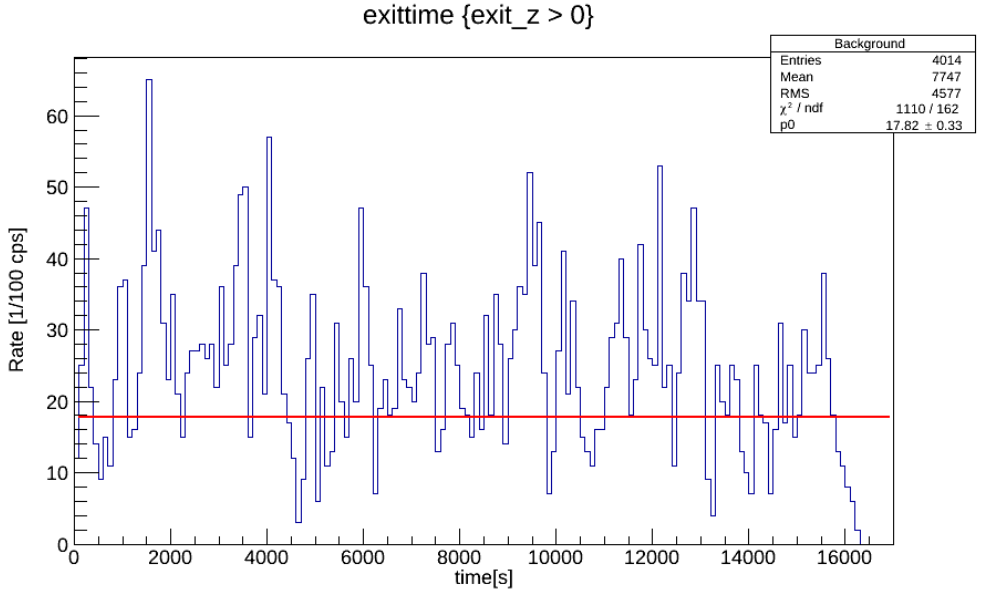

Figure 4.18.: Simulated background signal for 67 mBq activity with the same settings as in figure 4.17. $R_{\text{fit}} = 0.178 \pm 0.033$ cps, $R_{\text{long}} = 0.247 \pm 0.003$ cps.

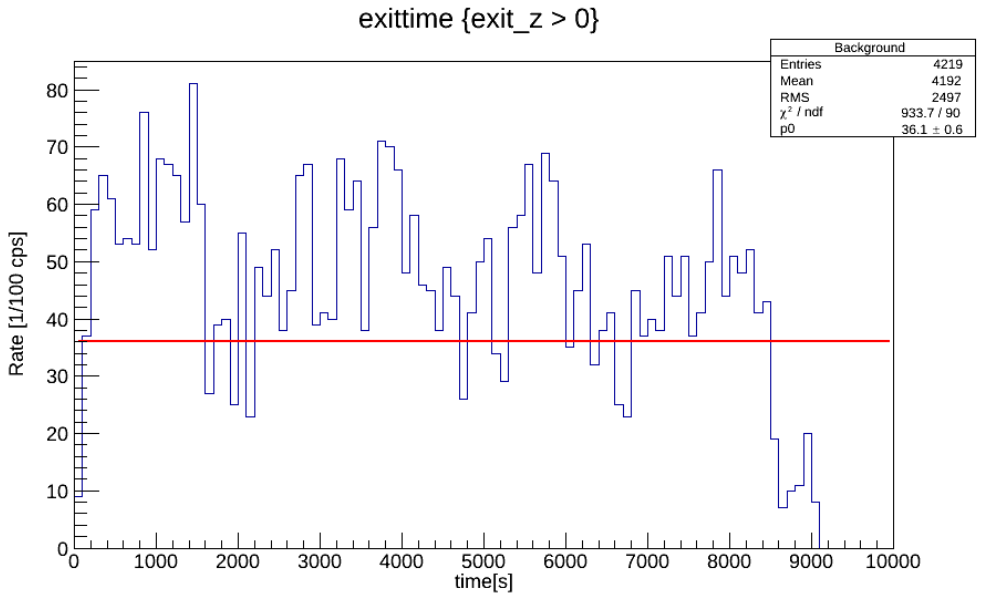

Figure 4.19.: Simulated background signal for 118 mBq activity. $R_{\text{fit}} = 0.361 \pm 0.006$ cps, $R_{\text{long}} = 0.463 \pm 0.007$ cps

5. Conclusion

In this thesis a new versatile tool for the simulation of electron storage in the KATRIN spectrometers has been developed. Due to its strong approximations it can provide quick insights in to the background generation through stored particles. The computation speed however comes at a cost. Since adiabaticity is always assumed, nonadiabatic effects can not be investigated. This drawback could in the future be compensated by hybrid simulations that compute the very high energetic electrons separately and give the produced low energy electrons as an input into the storage simulation. With the help of this new tool it was possible to explain an unexpected effect that was observed during the SDS commissioning measurements at the KATRIN main spectrometer. With the main spectrometers vessel on ground potential the observed background rate increases exponentially with the retarding voltage applied to the inner electrode. This can be explained as a result of electron avalanches which draw energy from the applied potential to ionize residual gas atoms inside the spectrometer. However the background situation at the main spectrometer currently is not well understood and further measurements are necessary to investigate especially in what processes the ions are produced and if the field emission at large offset voltages between vessel and inner electrode poses a problem. Considering the background caused by radon and stored electrons the planned measurement with low amounts of krypton artificially brought into the spectrometer might help to better understand the background properties of the main spectrometer. With the commissioning of the spectrometer-detector-section KATRIN has taken a huge step towards the tritium measurements, and possibly towards the observation of a finite neutrino mass. Ongoing effort will be necessary to achieve the design criteria of the KATRIN experiment, a background of less than 10 mcps remains a challenging goal.

Bibliography

[1] W. Pauli, "Letter to Gauvereinstagung in Tübingen: Sehr geehrte radioaktive Damen und Herren," in *Wolfgang Pauli, Collected scientific Papers* (R.Kronig and V. Weisskopf, eds.), vol. 2, pp. 173–204, New York (1964): Interscience, 1930.

[2] J. Chadwick, "Intensitätsverteilung im magnetischen Spectrum der β-Strahlen von Radium B + C," *Verhandl. Dtsc. Phys. Ges.*, vol. 16, p. 383, 1914.

[3] F. A. Scott, "Energy spectrum of the beta-rays of radium E," *Phys. Rev.*, vol. 48, pp. 391–395, Sep 1935.

[4] J. Chadwick, "Possible existence of a neutron," *Nature*, vol. 129, no. 3252, p. 312, 1932.

[5] E. Fermi, "Versuch einer Theorie der β-Strahlen. I," *Zeitschrift für Physik*, vol. 88, no. 3-4, pp. 161–177, 1934.

[6] H. Bethe and R. Peierls, "The "neutrino"," *Nature*, vol. 133, no. 532, pp. 689–690, 1934.

[7] C. L. Cowan, F. Reines, F. B. Harrison, H. W. Kruse, and A. D. McGuire, "Detection of the free neutrino: a confirmation," *Science*, vol. 124, no. 3212, pp. 103–104, 1956.

[8] F. Reines, C. Cowan Jr, F. Harrison, A. McGuire, and H. Kruse, "Detection of the free antineutrino," *Physical Review*, vol. 117, no. 1, p. 159, 1960.

[9] G. Danby, J. Gaillard, K. Goulianos, L. Lederman, N. Mistry, M. Schwartz, and J. Steinberger, "Observation of high-energy neutrino reactions and the existence of two kinds of neutrinos," *Physical Review Letters*, vol. 9, no. 1, pp. 36–44, 1962.

[10] M. L. Perl, G. S. Abrams, A. M. Boyarski, *et al.*, "Evidence for anomalous lepton production in $e^+ - e^-$ annihilation," *Phys. Rev. Lett.*, vol. 35, pp. 1489–1492, Dec 1975.

[11] K. Kodama, N. Ushida, C. Andreopoulos, N. Saoulidou, G. Tzanakos, P. Yager, B. Baller, D. Boehnlein, W. Freeman, B. Lundberg, *et al.*, "Observation of tau neutrino interactions," *Physics Letters B*, vol. 504, no. 3, pp. 218–224, 2001.

[12] D. Decamp, B. Deschizeaux, J.-P. Lees, M.-N. Minard, J. Crespo, M. Delfino, E. Fernandez, M. Martinez, R. Miquel, M. Mir, *et al.*, "Determination of the number of light neutrino species," *Physics Letters B*, vol. 231, no. 4, pp. 519–529, 1989.

[13] D. Decamp, B. Deschizeaux, J.-P. Lees, M.-N. Minard, J. Crespo, M. Delfino, E. Fernandez, M. Martinez, R. Miquel, L. M. Mir, *et al.*, "A precise determination of the number of families with light neutrinos and of the z boson partial widths," *Physics Letters B*, vol. 235, no. 3, pp. 399–411, 1990.

[14] M. E. Peskin and D. V. Schroeder, *An Introduction to quantum field theory*. Reading, USA: Addison-Wesley, 1995.

[15] S. L. Glashow, "Partial-symmetries of weak interactions," *Nuclear Physics*, vol. 22, no. 4, pp. 579–588, 1961.

[16] S. Weinberg, "A model of leptons," *Phys. Rev. Lett.*, vol. 19, pp. 1264–1266, Nov 1967.

[17] A. Salam and N. Svartholm, "Proc. 8th nobel symposium," *Stockholm, ed. N. Svartholm (Almqvist and Wiksells, Stockholm 1968)*, p. 367, 1968.

[18] J. G. Polchinski, *String theory*. Cambridge university press, 2003.

[19] C. Rovelli, "Loop quantum gravity," *Living Reviews in Relativity*, vol. 1, no. 1, 1998.

[20] S. Weinberg, "Ultraviolet divergences in quantum theories of gravitation.," in *General relativity: an Einstein centenary survey*, vol. 1, pp. 790–831, 1979.

[21] M. Fierz, "Über die relativistische Theorie kräftefreier Teilchen mit beliebigem Spin," *Helv. Phys. Acta*, vol. 12, no. 3, 1939.

[22] W. Pauli, "The connection between spin and statistics," *Physical Review*, vol. 58, no. 8, p. 716, 1940.

[23] P. W. Higgs, "Broken symmetries and the masses of gauge bosons," *Physical Review Letters*, vol. 13, no. 16, p. 508, 1964.

[24] F. Englert and R. Brout, "Broken symmetry and the mass of gauge vector mesons'," *Selected Papers on Gauge Theory of Weak and Electromagnetic Interactions*, p. 127, 1981.

[25] G. Aad, T. Abajyan, B. Abbott, J. Abdallah, S. A. Khalek, A. Abdelalim, O. Abdinov, R. Aben, B. Abi, M. Abolins, *et al.*, "Observation of a new particle in the search for the standard model higgs boson with the atlas detector at the lhc," *Physics letters. B*, vol. 716, no. 1, pp. 1–29, 2012.

[26] S. Chatrchyan, V. Khachatryan, A. Sirunyan, A. Tumasyan, W. Adam, T. Bergauer, M. Dragicevic, J. Eroe, C. Fabjan, M. Friedl, *et al.*, "Combined results of searches for the standard model higgs boson in pp collisions at $\sqrt{(s)} = 7$ TeV," *Physics Letters B*, vol. 710, no. 1, pp. 26–48, 2012.

[27] M. Goldhaber, L. Grodzins, and A. Sunyar, "Helicity of neutrinos," *Physical Review (US) Superseded in part by Phys. Rev. A, Phys. Rev. B: Solid State, Phys. Rev. C, and Phys. Rev. D*, vol. 109, 1958.

[28] E. Majorana, "Teoria simmetrica dell'elettrone e del positrone," *Il Nuovo Cimento*, vol. 14, no. 4, pp. 171–184, 1937.

[29] I. Krivosheina, "SN 1987 A-Historical View About Registration of the Neutrino Signal with BAKSAN, Kamiokande II, and IMB Detectors," *Sringer Proceedings in Physics*, vol. 92, pp. 685–710, 2003.

[30] J. Brunner, "Antares - astronomie in der tiefsee," *Sterne und Weltraum*, 2006.

[31] J. N. Bahcall, A. M. Serenelli, and S. Basu, "New solar opacities, abundances, helioseismology, and neutrino fluxes," *The Astrophysical Journal Letters*, vol. 621, no. 1, p. L85, 2005.

[32] R. Davis, "A review of the homestake solar neutrino experiment," *Progress in Particle and Nuclear Physics*, vol. 32, pp. 13–32, 1994.

[33] B. Cleveland, T. Daily, R. Davis Jr, J. Distel, K. Lande, C. Lee, P. Wildenhain, and J. Ullman, "Update on the measurement of the solar neutrino flux with the Homestake chlorine detector," *Nuclear Physics B-Proceedings Supplements*, vol. 38, no. 1, pp. 47–53, 1995.

[34] W. Hampel, J. Handt, G. Heusser, J. Kiko, T. Kirsten, M. Laubenstein, E. Pernicka, W. Rau, M. Wojcik, Y. Zakharov, *et al.*, "Gallex solar neutrino observations: Results for gallex iv," *Physics Letters B*, vol. 447, no. 1, pp. 127–133, 1999.

[35] M. Altmann, M. Balata, P. Belli, E. Bellotti, R. Bernabei, E. Burkert, C. Cattadori, R. Cerulli, M. Chiarini, M. Cribier, *et al.*, "Complete results for five years of gno solar neutrino observations," *Physics Letters B*, vol. 616, no. 3, pp. 174–190, 2005.

[36] J. Abdurashitov, E. Veretenkin, V. Vermul, V. Gavrin, S. Girin, V. Gorbachev, P. Gurkina, G. Zatsepin, T. Ibragimova, A. Kalikhov, *et al.*, "Solar neutrino flux measurements by the soviet-american gallium experiment (sage) for half the 22-year solar cycle," *Journal of Experimental and Theoretical Physics*, vol. 95, no. 2, pp. 181–193, 2002.

[37] Y. Fukuda, T. Hayakawa, K. Inoue, K. Ishihara, H. Ishino, S. Joukou, T. Kajita, S. Kasuga, Y. Koshio, T. Kumita, *et al.*, "Solar neutrino data covering solar cycle 22," *Physical Review Letters*, vol. 77, no. 9, p. 1683, 1996.

[38] V. Gribov and B. Pontecorvo, "Neutrino astronomy and lepton charge," *Physics Letters B*, vol. 28, no. 7, pp. 493–496, 1969.

[39] Q. Ahmad, R. Allen, T. Andersen, J. Anglin, J. Barton, E. Beier, M. Bercovitch, J. Bigu, S. Biller, R. Black, *et al.*, "Direct evidence for neutrino flavor transformation from neutral-current interactions in the sudbury neutrino observatory," *Physical Review Letters*, vol. 89, no. 1, p. 011301, 2002.

[40] B. Aharmim, Q. R. Ahmad, S. N. Ahmed, *et al.*, "Determination of the ν_e and total ^{8}B solar neutrino fluxes using the sudbury neutrino observatory phase i data set," *Phys. Rev. C*, vol. 75, p. 045502, Apr 2007.

[41] N. Cabibbo, "Unitary symmetry and leptonic decays," *Phys. Rev. Lett.*, vol. 10, pp. 531–533, Jun 1963.

[42] Y. Abe, C. Aberle, T. Akiri, *et al.*, "Indication of reactor $\bar{\nu}_e$ disappearance in the double chooz experiment," *Phys. Rev. Lett.*, vol. 108, p. 131801, Mar 2012.

[43] F. An, J. Bai, A. Balantekin, H. Band, D. Beavis, W. Beriguete, M. Bishai, S. Blyth, K. Boddy, R. Brown, *et al.*, "Observation of electron-antineutrino disappearance at daya bay," *Physical Review Letters*, vol. 108, no. 17, p. 171803, 2012.

[44] J. K. Ahn, S. Chebotaryov, J. H. Choi, *et al.*, "Observation of reactor electron antineutrinos disappearance in the RENO experiment," *Phys. Rev. Lett.*, vol. 108, p. 191802, May 2012.

[45] D. C. Collaboration, 2012. Double Chooz Experiment. Website, http://doublechooz.in2p3.fr/Public/German/welcome.php.

[46] K. Abe, N. Abgrall, Y. Ajima, H. Aihara, J. Albert, C. Andreopoulos, B. Andrieu, S. Aoki, O. Araoka, J. Argyriades, *et al.*, "Indication of electron neutrino appearance from an accelerator-produced off-axis muon neutrino beam," *Physical review letters*, vol. 107, no. 4, p. 041801, 2011.

[47] P. Adamson, D. Auty, D. Ayres, C. Backhouse, G. Barr, M. Betancourt, M. Bishai, A. Blake, G. Bock, D. Boehnlein, *et al.*, "Improved search for muon-neutrino to electron-neutrino oscillations in minos," *Physical review letters*, vol. 107, no. 18, p. 181802, 2011.

[48] M. Apollonio, A. Baldini, C. Bemporad, E. Caffau, F. Cei, Y. Declais, H. De Kerret, B. Dieterle, A. Etenko, J. George, *et al.*, "Limits on neutrino oscillations from the chooz experiment," *Physics Letters B*, vol. 466, no. 2, pp. 415–430, 1999.

[49] L. Wolfenstein, "Neutrino oscillations in matter," *Physical Review D*, vol. 17, no. 9, p. 2369, 1978.

[50] S. Mikheyev and A. Y. Smirnov, "Resonant amplification of ν oscillations in matter and solar-neutrino spectroscopy," *Il Nuovo Cimento C*, vol. 9, no. 1, pp. 17–26, 1986.

[51] J. Beringer, J. Arguin, R. Barnett, K. Copic, O. Dahl, D. Groom, C. Lin, J. Lys, H. Murayama, C. Wohl, *et al.*, "Review of particle physics (and 2013 partial update)," *Physical Review D*, vol. 86, no. 1, 2012.

[52] G. Altarelli and K. Winter, *Neutrino Mass: With 10 Tables*. No. 190, Springer, 2003.

[53] K. Collaboration, J. Angrik, *et al.*, "KATRIN design report 2004," *FZKA-7090*, 2005.

[54] A. Einstein, "Die formale Grundlage der allgemeinen Relativitätstheorie," *Sitzungsberichte der Königlich Preußischen Akademie der Wissenschaften (Berlin), Seite 1030-1085.*, vol. 1, pp. 1030–1085, 1914.

[55] A. Einstein, "Die Feldgleichungen der Gravitation," *Sitzungsberichte der Königlich Preußischen Akademie der Wissenschaften (Berlin), Seite 844-847.*, vol. 1, pp. 844–847, 1915.

[56] A. Einstein, "Die Grundlage der allgemeinen Relativitätstheorie," *Annalen der Physik*, vol. 354, no. 7, pp. 769–822, 1916.

[57] A. Einstein, "Kosmologische betrachtungen zur allgemeinen Relativitätstheorie," *Sitzungsberichte der Königlich Preußischen Akademie der Wissenschaften (Berlin), Seite 142-152.*, vol. 1, pp. 142–152, 1917.

[58] V. C. Rubin, W. K. J. Ford, and N. . Thonnard, "Rotational properties of 21 sc galaxies with a large range of luminosities and radii, from ngc 4605 $r = 4$ kpc to ugc 2885 $r = 122$ kpc," *APJ*, vol. 238, pp. 471–487, June 1980.

[59] P. Fischer, T. A. McKay, E. Sheldon, A. Connolly, A. Stebbins, J. A. Frieman, B. Jain, M. Joffre, D. Johnston, G. Bernstein, *et al.*, "Weak lensing with sloan digital sky survey commissioning data: the galaxy-mass correlation function to 1 h- 1 mpc," *The Astronomical Journal*, vol. 120, no. 3, p. 1198, 2000.

[60] M. Markevitch, S. Randall, D. Clowe, A. Gonzalez, and M. Bradac, "Dark matter and the bullet cluster," in *36th COSPAR Scientific Assembly*, vol. 36, p. 2655, 2006.

[61] M. Markevitch, A. H. Gonzalez, D. Clowe, A. Vikhlinin, W. Forman, C. Jones, S. Murray, and W. Tucker, "Direct constraints on the dark matter self-interaction cross section from the merging galaxy cluster 1e 0657–56," *The Astrophysical Journal*, vol. 606, no. 2, p. 819, 2004.

[62] A. A. Penzias and R. W. Wilson, "A measurement of excess antenna temperature at 4080 mc/s.," *The Astrophysical Journal*, vol. 142, pp. 419–421, 1965.

[63] E. Wright, J. Mather, C. Bennett, E. Cheng, R. Shafer, D. Fixsen, R. Eplee Jr, R. Isaacman, S. Read, N. Boggess, *et al.*, "Preliminary spectral observations of the galaxy with a 7 deg beam by the cosmic background explorer (cobe)," *The Astrophysical Journal*, vol. 381, pp. 200–209, 1991.

[64] C. Bennett, D. Larson, J. Weiland, N. Jarosik, G. Hinshaw, N. Odegard, K. Smith, R. Hill, B. Gold, M. Halpern, *et al.*, "Nine-year wilkinson microwave anisotropy probe (wmap) observations: Final maps and results," *arXiv preprint arXiv:1212.5225*, 2012.

[65] P. Ade, L. Wade, V. Stolyarov, F. Desert, J. Knoche, M. Giard, X. Dupac, M. Liguori, S. Matarrese, H. Kurki-Suonio, *et al.*, "Planck 2013 results. xvi. cosmological parameters," tech. rep., Planck Collaboration, 2013.

[66] S. Agarwal and H. A. Feldman, "The effect of massive neutrinos on the matter power spectrum," *Monthly Notices of the Royal Astronomical Society*, vol. 410, no. 3, pp. 1647–1654, 2011.

[67] S. Hannestad, "Neutrino masses and the dark energy equation of state:relaxing the cosmological neutrino mass bound," *Phys. Rev. Lett.*, vol. 95, p. 221301, Nov 2005.

[68] S. Elliott, A. Hahn, and M. Moe, "Direct evidence for two-neutrino double-beta decay in^{82} se," *Physical Review Letters*, vol. 59, no. 18, p. 2020, 1987.

[69] M. Goeppert-Mayer, "Double beta-disintegration," *Physical Review*, vol. 48, pp. 512–516, 1935.

[70] G. Racah, "Sulla simmetria tra particelle e antiparticelle," *Il Nuovo Cimento (1924-1942)*, vol. 14, no. 7, pp. 322–328, 1937.

[71] W. Furry, "On transition probabilities in double beta-disintegration," *Physical Review*, vol. 56, no. 12, p. 1184, 1939.

[72] H. Klapdor-Kleingrothaus, A. Dietz, H. Harney, and I. Krivosheina, "Evidence for neutrinoless double beta decay," *Modern Physics Letters A*, vol. 16, no. 37, pp. 2409–2420, 2001.

[73] M. Agostini *et al.*, "Results on neutrinoless double beta decay of 76Ge from GERDA Phase I," 2013.

[74] M. Sisti, C. Arnaboldi, C. Brofferio, G. Ceruti, O. Cremonesi, E. Fiorini, A. Giuliani, B. Margesin, L. Martensson, A. Nucciotti, *et al.*, "New limits from the milano neutrino mass experiment with thermal microcalorimeters," *Nuclear Instruments and Methods in Physics Research Section A: Accelerators, Spectrometers, Detectors and Associated Equipment*, vol. 520, no. 1, pp. 125–131, 2004.

[75] E. Ferri, C. Arnaboldi, G. Ceruti, M. Faverzani, F. Gatti, A. Giachero, C. Gotti, C. Kilbourne, S. Kraft-Bermuth, A. Nucciotti, *et al.*, "Mare-1 in milan: status and perspectives," *Journal of Low Temperature Physics*, vol. 167, no. 5-6, pp. 1035–1040, 2012.

[76] C. Kraus, B. Bornschein, L. Bornschein, J. Bonn, B. Flatt, A. Kovalik, B. Ostrick, E. Otten, J. Schall, T. Thümmler, *et al.*, "Final results from phase II of the Mainz neutrino mass search in tritium β decay," *The European Physical Journal C-Particles and Fields*, vol. 40, no. 4, pp. 447–468, 2005.

[77] V. Aseev, A. Belesev, A. Berlev, E. Geraskin, A. Golubev, N. Likhovid, V. Lobashev, A. Nozik, V. Pantuev, V. Parfenov, *et al.*, "Upper limit on the electron antineutrino mass from the troitsk experiment," *Physical Review D*, vol. 84, no. 11, p. 112003, 2011.

[78] E. Otten and C. Weinheimer, "Neutrino mass limit from tritium β decay," *Reports on Progress in Physics*, vol. 71, no. 8, p. 086201, 2008.

[79] J. Bonn, B. Bornschein, L. Bornschein, L. Fickinger, B. Flatt, O. Kazachenko, A. Kovalik, C. Kraus, E. Otten, J. Schall, *et al.*, "The mainz neutrino mass experiment," *Nuclear Physics B-Proceedings Supplements*, vol. 91, no. 1, pp. 273–279, 2001.

[80] V. Lobashev, V. Aseev, A. Belesev, A. Berlev, E. Geraskin, A. Golubev, O. Kazachenko, Y. E. Kuznetsov, R. Ostroumov, L. Rivkis, *et al.*, "Direct search for mass of neutrino and anomaly in the tritium beta-spectrum," *Physics Letters B*, vol. 460, no. 1, pp. 227–235, 1999.

[81] V. Lobashev, V. Aseev, A. Belesev, A. Berlev, E. Geraskin, A. Golubev, O. Kazachenko, Y. E. Kuznetsov, R. Ostroumov, L. Rivkis, *et al.*, "Direct search for neutrino mass and anomaly in the tritium beta-spectrum: Status of "troitsk neutrino mass" experiment," *Nuclear Physics B-Proceedings Supplements*, vol. 91, no. 1, pp. 280–286, 2001.

[82] A. Picard, H. Backe, H. Barth, J. Bonn, B. Degen, T. Edling, R. Haid, A. Hermanni, P. Leiderer, T. Loeken, A. Molz, R. Moore, A. Osipowicz, E. Otten, M. Przyrembel, M. Schrader, M. Steininger, and C. Weinheimer, "A solenoid retarding spectrometer with high resolution and transmission for kev electrons," *Nuclear Instruments and Methods in Physics Research Section B: Beam Interactions with Materials and Atoms*, vol. 63, no. 3, pp. 345 – 358, 1992.

[83] N. Wandkowsky, *Study of background and transmission properties of the KATRIN spectrometers*. PhD thesis, KIT, 2013.

[84] H. Higaki, K. Ito, K. Kira, and H. Okamoto, "Electrons confined with an axially symmetric magnetic mirror field," *AIP Conference Proceedings*, vol. 1037, no. 1, pp. 106–114, 2008.

[85] C. Kranz, "Optimierung der methoden und messprozeduren zur entfaltung der energieverlustfunktion beim katrin-experiment," Master's thesis, University of Münster, 2011.

[86] J. Reich, *Magnetic Field Inhomogeneities and Their Influence on Transmission and Background at the KATRIN Main Spectrometer*. PhD thesis, KIT, 2013.

[87] M. Babutzka, M. Bahr, J. Bonn, B. Bornschein, A. Dieter, G. Drexlin, K. Eitel, S. Fischer, F. Glück, S. Grohmann, *et al.*, "Monitoring of the operating parameters of the KATRIN windowless gaseous tritium source," *New Journal of Physics*, vol. 14, no. 10, pp. 103046–103074, 2012.

[88] M. Sturm, *Aufbau und Test des Inner-Loop-Systems der Tritiumquelle von KATRIN*. PhD thesis, KIT, 2010.

[89] S. Grohmann, T. Bode, H. Schön, and M. Süßer, "Precise temperature measurement at 30 k in the KATRIN source cryostat," *Cryogenics*, vol. 51, no. 8, pp. 438 – 445, 2011.

[90] T. Bode, "Optimierung des 2-Phasen-Kühlkonzepts für den WGTS-Demonstrator von KATRIN," Master's thesis, KIT, 2011.

[91] S. Grohmann, "Stability analyses of the beam tube cooling system in the KATRIN source cryostat," *Cryogenics*, vol. 49, no. 8, pp. 413 – 420, 2009.

[92] M. Hötzel, "Berechnung von KATRIN Messspektren unter Einbeziehung der Eigenschaften der fensterlosen gasförmigen Tritiumquelle," Master's thesis, KIT, 2009.

[93] M. Hötzel, *Simulation and analysis of source-related effects for KATRIN*. PhD thesis, KIT, 2012.

[94] M. Schlösser, H. Seitz, S. Rupp, P. Herwig, C. G. Alecu, M. Sturm, and B. Bornschein, "In-line calibration of raman systems for analysis of gas mixtures of hydrogen isotopologues with sub-percent accuracy," *Analytical Chemistry*, vol. 85, no. 5, pp. 2739–2745, 2013.

[95] M. Schlösser, *Accurate calibration of the Raman system for the Karlsruhe Tritium Neutrino Experiment*. PhD thesis, KIT, 2013.

[96] M. Röllig, "Studien zu einem Röntgendetektorsystem zur Bestimmung der Aktivität in der KATRIN Tritiumquelle," Master's thesis, KIT, 2011.

[97] M. Babutzka, "Status of the rear section.," *KATRIN Collaboration meeting*, 2013.

[98] A. Kosmider, *Tritium Retention Techniques in the KATRIN Transport Section and Commissioning of its DPS2-F Cryostat.* PhD thesis, KIT, 2012.

[99] S. Mertens, G. Drexlin, F. Fränkle, D. Furse, F. Glück, S. Görhardt, M. Hötzel, W. Käfer, B. Leiber, T. Thümmler, and N. Wandkowsky, "Background due to stored electrons following nuclear decays in the KATRIN spectrometers and its impact on the neutrino mass sensitivity," *Astroparticle Physics*, 2012.

[100] X. Luo, C. Day, V. Hauer, O. Malyshev, R. Reid, and F. Sharipov, "Monte carlo simulation of gas flow through the KATRIN dps2-f differential pumping system," *Vacuum*, vol. 80, no. 8, pp. 864–869, 2006.

[101] M. Ubieto-Dıaz, *Off-line commissioning of a non-destructive FT-ICR system for monitoring the ion concentration in the KATRIN beamline.* PhD thesis, Ruprecht-Karls-Universität Heidelberg, MPIK, 2011.

[102] M. Ubieto-Diaz, D. Rodriguez, S. Lukic, S. Nagy, S. Stahl, and K. Blaum, "A broad-band ft-icr penning trap system for KATRIN," *International Journal of Mass Spectrometry*, vol. 288, no. 1, pp. 1–5, 2009.

[103] A. Windberger, "Berechnungen und Simulationen zum Verhalten von Ionen in der differenziellen Pumpstrecke des KATRIN-Experiments," Master's thesis, KIT, 2010.

[104] F. Glück, "Electrons and ions in KATRIN STS," *KATRIN Collaboration meeting*, October 2010.

[105] S. Reimer, "Ein elektrostatisches Dipolsystem zur Eliminierung von Ionen in der DPS2-F des KATRIN Experiments," Master's thesis, KIT, 2009.

[106] X. Luo and C. Day, "Test particle monte carlo study of the cryogenic pumping system of the karlsruhe tritium neutrino experiment," *Journal of Vacuum Science & Technology A: Vacuum, Surfaces, and Films*, vol. 26, no. 5, pp. 1319–1325, 2008.

[107] M. Prall, P. Renschler, F. Glück, A. Beglarian, H. Bichsel, L. Bornschein, Z. Chaoui, G. Drexlin, F. Fränkle, S. Görhardt, *et al.*, "The katrin pre-spectrometer at reduced filter energy," *New Journal of Physics*, vol. 14, no. 7, p. 073054, 2012.

[108] F. Glück, G. Drexlin, B. Leiber, S. Mertens, A. Osipowicz, J. Reich, and N. Wandkowsky, "Electromagnetic design of the large-volume air coil system of the katrin experiment," *New Journal of Physics*, vol. 15, no. 8, p. 083025, 2013.

[109] K. Valerius, "The wire electrode system for the KATRIN main spectrometer," *Progress in Particle and Nuclear Physics*, vol. 64, no. 2, pp. 291 – 293, 2010.

[110] K. Valerius, "Electromagnetic design and inner electrode for the KATRIN main spectrometer," *Progress in Particle and Nuclear Physics*, vol. 57, no. 1, pp. 58–60, 2006.

[111] M. Zacher, "Electromagnetic design and field emission studies for the inner electrode system of the KATRIN main spectrometer," Master's thesis, University of Münster, 2009.

[112] K. Valerius, *Spectrometer-related background processes and their suppression in the KATRIN experiment.* PhD thesis, University of Münster, 2009.

[113] J. Wolf, "Size matters: The vacuum system of the katrin neutrino experiment," *Journal of the Vacuum Society of Japan*, vol. 52, pp. 278–284, 2009.

[114] X. Luo, L. Bornschein, C. Day, and J. Wolf, "Katrin neg pumping concept investigation," *Vacuum*, vol. 81, no. 6, pp. 777–781, 2007.

[115] C. Day, X. Luo, A. Conte, A. Bonucci, and P. Manini, "Determination of the sticking probability of a zr–v–fe nonevaporable getter strip," *Journal of Vacuum Science & Technology A: Vacuum, Surfaces, and Films*, vol. 25, no. 4, pp. 824–830, 2007.

[116] M. Zboril, *Solid electron sources for the energy scale monitoring in the KATRIN experiment*. PhD thesis, University of Münster, 2011.

[117] M. Slezak, *The source of monoenergetic electrons for the monitoring of spectrometer in the KATRIN neutrino experiment*. PhD thesis, Charles University Prague, 2011.

[118] M. Erhard, "Untersuchung der Langzeitstabilität des nuklearen Standards für die Energieskala des KATRIN-Expriments," Master's thesis, KIT, 2012.

[119] J. Goullon, "Installation and commissioning of the monitor spectrometer," Master's thesis, KIT, 2010.

[120] M. Schupp, "Inbetriebnahme des Monitorspektrometers und erste Messungen," Master's thesis, KIT, 2011.

[121] S. Bauer, "Aufbau und Inbetriebnahme des zweiten Präzisions-Hochspannungsteilers bis 65 keV für das KATRIN-Experiment," Diploma thesis, Univ. Münster, 2009.

[122] F. Harms, "Assembly and first results of the katrin focal-plane detec-tor system at kit," Master's thesis, KIT, 2012.

[123] S. Görhardt, "Reduktion der durch Radon induzierten Untergrundprozesse in den KATRIN Spektrometern," Master's thesis, KIT, 2010.

[124] N. Wandkowsky, G. Drexlin, F. M. Fränkle, F. Glück, S. Groh, and S. Mertens, "Validation of a model for radon-induced background processes in electrostatic spectrometers," *Journal of Physics G: Nuclear and Particle Physics*, vol. 40, no. 8, p. 085102, 2013.

[125] F. Fränkle, L. Bornschein, G. Drexlin, F. Glück, S. Görhardt, W. Käfer, S. Mertens, N. Wandkowsky, and J. Wolf, "Radon induced background processes in the KATRIN pre-spectrometer," *Astroparticle Physics*, vol. 35, no. 3, pp. 128 – 134, 2011.

[126] D. Furse *et al.*, "Kassiopeia - the simulation package for the KATRIN experiment," in preparation.

[127] D. Furse. PhD thesis, MIT, 2013. in preparation.

[128] M. Haag. PhD thesis, KIT, 2014. in preparation.

[129] T. J. Corona, "Tools for Electromagnetic Field Simulation in the KATRIN Experiment ," Master's thesis, MIT, 2009.

[130] T. Corona, "Fully Three-Dimensional Electrostatic Simulations of the Main Spectrometer." KATRIN Collaboration meeting, March 2013, `http://fuzzy.fzk.de/bscw/bscw.cgi/774166/95-TRP-5453-S5-TJCorona.pdf`.

[131] D. Poljak and C. A. Brebbia, *Boundary element methods for electrical engineers*, vol. 4. WIT Press, 2005.

[132] F. Glück, "Axisymmetric electric field calculation with zonal harmonic expansion," *Progress In Electromagnetics Research B*, vol. 32, pp. 319–350, 2011.

[133] J. A. Formaggio, P. Lazic, T. Corona, H. Stefancic, H. Abraham, and F. Gluck, "Solving for micro-and macro-scale electrostatic configurations using the robin hood algorithm," *arXiv preprint arXiv:1111.5035*, 2011.

[134] P. Renschler, *KESS - A new Monte Carlo simulation code for low-energy electron interactions in silicon detectors.* PhD thesis, KIT, 2011.

[135] F. R. Elder, A. M. Gurewitsch, R. V. Langmuir, and H. C. Pollock, "Radiation from electrons in a synchrotron," *Phys. Rev.*, vol. 71, pp. 829–830, Jun 1947.

[136] P. A. Dirac, "Classical theory of radiating electrons," *Proceedings of the Royal Society of London. Series A. Mathematical and Physical Sciences*, vol. 167, no. 929, pp. 148–169, 1938.

[137] P. R. Johnson and B.-L. Hu, "Stochastic theory of relativistic particles moving in a quantum field: Scalar abraham-lorentz-dirac-langevin equation, radiation reaction, and vacuum fluctuations," *Physical Review D*, vol. 65, no. 6, p. 065015, 2002.

[138] A. D. Yaghjian, *Relativistic dynamics of a charged sphere: updating the Lorentz-Abraham model*, vol. 11. Springer, 1992.

[139] F. Rohrlich, "The dynamics of a charged sphere and the electron," *American Journal of Physics*, vol. 65, p. 1051, 1997.

[140] R. Medina, "Radiation reaction of a classical quasi-rigid extended particle," *Journal of Physics A: Mathematical and General*, vol. 39, no. 14, p. 3801, 2006.

[141] S. Mertens, *Study of Background Processes in the Electrostatic Spectrometers of the KATRIN Experiment.* PhD thesis, KIT, 2012.

[142] H. Tawara, Y. Itikawa, H. Nishimura, and M. Yoshino, "Cross sections and related data for electron collisions with hydrogen molecules and molecular ions," *Journal of Physical and Chemical Reference Data*, vol. 19, p. 617, 1990.

[143] N. Wandkowsky, "Design and background simulations for the katrin main spectrometer and air coil system," Master's thesis, KIT, 2009.

[144] F. M. Fränkle, *Background Investigations of the KATRIN Pre-Spectrometer.* PhD thesis, KIT, 2010.

[145] N. Wandkowsky *et al.*, "Modeling of electron emission processes accompanying Radon-α-decays within electrostatic spectrometers," *subm. to New J. Phys.*, 2013. arXiv:1304.1375.

[146] Electronic Logbook for SDS commissioning measurements, "Elog entry nr. 9," 2013. https://neutrino.ikp.kit.edu:8080/SDS-Measurements/9.

[147] Electronic Logbook for SDS commissioning measurements, "Elog entry nr. 19," 2013. https://neutrino.ikp.kit.edu:8080/SDS-Measurements/19.

[148] Electronic Logbook for SDS commissioning measurements, "Elog entry nr. 29," 2013. https://neutrino.ikp.kit.edu:8080/SDS-Measurements/29.

[149] Electronic Logbook for SDS commissioning measurements, "Elog entry nr. 41," 2013. https://neutrino.ikp.kit.edu:8080/SDS-Measurements/41.

[150] Electronic Logbook for SDS commissioning measurements, "Elog entry nr. 46," 2013. https://neutrino.ikp.kit.edu:8080/SDS-Measurements/46.

[151] N. Stallkamp Master's thesis, KIT, 2013. in preparation.

[152] Electronic Logbook for SDS commissioning measurements, "Elog entry nr. 228," 2013. https://neutrino.ikp.kit.edu:8080/SDS-Measurements/228.

[153] Electronic Logbook for SDS commissioning measurements, "Elog entry nr. 28," 2013. https://neutrino.ikp.kit.edu:8080/SDS-Measurements/28.

[154] Electronic Logbook for SDS commissioning measurements, "Elog entry nr. 213," 2013. https://neutrino.ikp.kit.edu:8080/SDS-Measurements/213.

[155] Electronic Logbook for SDS commissioning measurements, "Elog entry nr. 238," 2013. https://neutrino.ikp.kit.edu:8080/SDS-Measurements/238.

[156] S. Görhardt. PhD thesis, KIT, 2013. in preparation.

[157] Electronic Logbook for SDS commissioning measurements, "Elog entry nr. 219," 2013. https://neutrino.ikp.kit.edu:8080/SDS-Measurements/219.

[158] Electronic Logbook for SDS commissioning measurements, "Elog entry nr. 235," 2013. https://neutrino.ikp.kit.edu:8080/SDS-Measurements/235.

[159] Electronic Logbook for SDS commissioning measurements, "Elog entry nr. 234," 2013. https://neutrino.ikp.kit.edu:8080/SDS-Measurements/234.

[160] R. Fowler and L. Nordheim, "Fn theory on field emission-tunneling," in *Proc. Roy. Soc.(London) A*, vol. 119, p. 173, 1928.

Appendix

A. Code work

Much of the work done in the course of this thesis has gone into the improvement of KASSIOPEIA. A list of contributions can be seen in the Münster Git-Repository at *https://nuserv.uni-muenster.de/cgit/cgit.cgi/Kasper.git/log/?qt=author&q=trost* or the private branches of the author found there.

Acknowledgement

Ich möchte hier allen danken die mich während meiner Diplomarbeit unterstütz haben und generell die Welt noch etwas lebenswerter machen. Besonderer Dank gebührt hier:

- ◇ Prof. Dr. G. Drexlin für die interessante Diplomarbeit und die Ermöglichung meiner Teilnahme an der EPSHEP 2013 in Stockholm,
- ◇ Prof. Dr. U. Husemann, für die Betreuung der Arbeit als Korreferent ,
- ◇ Dr. F. Glück für die vielen physikalischen Diskussion und seinen steten Frohsinn,
- ◇ Dr. N. Wandkowsky für die riesige Hilfsbereitschaft und geduldiges korrekturlesen,
- ◇ Dipl.-Phys. S. Groh für die Unterstützung bei allen Fragen zu Kassiopeia und der stetigen Bugjagd,
- ◇ Dipl.-Phys M. Haag für die tolle Zeit in Stockholm, den großen Einsatz für ordentlichen Kaffee, die guten Gespräche und das Verständnis für die Leiden der C++ Programmierung

Weiterhin danke ich allen Mitstreitern am KATRIN Experiment und im Institut für die gute Athmosphäre, die allseitige Hilfsbereitschaft und die fröhliche Zeit.